Program on Technology Innovation: Effects of Spatial Incoherence on Seismic Ground Motions

Program on Technology Innovation: Effects of Spatial Incoherence on Seismic Ground Motions

1015110

Final Report, December 2007

EPRI Project Manager
R. Kassawara

DISCLAIMER OF WARRANTIES AND LIMITATION OF LIABILITIES

THIS DOCUMENT WAS PREPARED BY THE ORGANIZATION(S) NAMED BELOW AS AN ACCOUNT OF WORK SPONSORED OR COSPONSORED BY THE ELECTRIC POWER RESEARCH INSTITUTE, INC. (EPRI). NEITHER EPRI, ANY MEMBER OF EPRI, ANY COSPONSOR, THE ORGANIZATION(S) BELOW, NOR ANY PERSON ACTING ON BEHALF OF ANY OF THEM:

(A) MAKES ANY WARRANTY OR REPRESENTATION WHATSOEVER, EXPRESS OR IMPLIED, (I) WITH RESPECT TO THE USE OF ANY INFORMATION, APPARATUS, METHOD, PROCESS, OR SIMILAR ITEM DISCLOSED IN THIS DOCUMENT, INCLUDING MERCHANTABILITY AND FITNESS FOR A PARTICULAR PURPOSE, OR (II) THAT SUCH USE DOES NOT INFRINGE ON OR INTERFERE WITH PRIVATELY OWNED RIGHTS, INCLUDING ANY PARTY'S INTELLECTUAL PROPERTY, OR (III) THAT THIS DOCUMENT IS SUITABLE TO ANY PARTICULAR USER'S CIRCUMSTANCE; OR

(B) ASSUMES RESPONSIBILITY FOR ANY DAMAGES OR OTHER LIABILITY WHATSOEVER (INCLUDING ANY CONSEQUENTIAL DAMAGES, EVEN IF EPRI OR ANY EPRI REPRESENTATIVE HAS BEEN ADVISED OF THE POSSIBILITY OF SUCH DAMAGES) RESULTING FROM YOUR SELECTION OR USE OF THIS DOCUMENT OR ANY INFORMATION, APPARATUS, METHOD, PROCESS, OR SIMILAR ITEM DISCLOSED IN THIS DOCUMENT.

ORGANIZATION(S) THAT PREPARED THIS DOCUMENT

Norman A. Abrahamson, Inc.

NOTE

For further information about EPRI, call the EPRI Customer Assistance Center at 800.313.3774 or e-mail askepri@epri.com.

Electric Power Research Institute, EPRI, and TOGETHER…SHAPING THE FUTURE OF ELECTRICITY are registered service marks of the Electric Power Research Institute, Inc.

CITATIONS

This report was prepared by

Norman A. Abrahamson, Inc.
152 Dracena Avenue
Piedmont, CA 94611

Principal Investigator
N. Abrahamson

This report describes research sponsored by the Electric Power Research Institute (EPRI).

The report is a corporate document that should be cited in the literature in the following manner:

Program on Technology Innovation: Effects of Spatial Incoherence on Seismic Ground Motions.
EPRI, Palo Alto, CA: 2007. 1015110.

PRODUCT DESCRIPTION

Spatial incoherency of strong ground motions has the effect of lowering earthquake input at building foundations. Previous coherency models for short separation distances (0 to 150 m) have been based on surface recordings from a suite of dense arrays located in Taiwan, Japan, and California. Most of these arrays were located on soil or soft-rock sites. The applicability of these data to hard-rock conditions in the Eastern United States (EUS) has been discussed at review meetings with the Nuclear Regulatory Commission (NRC). Of the data considered in the previous research, the Pinyon Flat array is the only hard-rock site. This study describes the development of empirical spatial coherency models for use in soil-structure interaction (SSI) analyses based on the Pinyon Flat array data. In addition, a soil site coherency model is developed based on an extensive set of soil array data. This soil site coherency model can be applied for SSI analyses for structures on soil sites.

Results & Findings
The coherency model based on the Pinyon Flat data set is applicable to hard-rock conditions, earthquakes of all magnitudes, all rupture distances, and station separation distances less than 150 m. The hard-rock coherency model can be used as a conservative model for coherency for soft-rock and soil sites as well as for embedded foundations; however lower coherency can be justified for soil and soft-rock site conditions.

Challenges & Objective(s)
Most of the studies of spatial coherency are based on evaluation of the ground motions from the dense array located in Lotung, Taiwan, due to the extensive database available from the SMART-1 strong motion array. To address the spatial variation over dimensions of foundations for nuclear power plants, EPRI supported the installation of the EPRI large-scale seismic test (LSST) array, also located in Lotung. Together, SMART-1 and LSST array data provide the largest sets of dense array data in terms of the number of earthquakes above magnitude 4.0 and the number of stations. While this large data set allows for robust empirical models of the coherency to be developed, it is not clear that the coherency models from Lotung, Taiwan, are applicable to other regions. The objective of the current study is to review the current coherency models and make any modifications needed for application to SSI analyses for U.S. nuclear power plants.

Applications, Values & Use
The hard rock coherency model can be used at nuclear plant sites to appreciably reduce the levels of motion, primarily at high frequencies, used for evaluation of structures and equipment.

EPRI Perspective

Spatial coherency has not been well understood by the majority of practicing earthquake engineers. The end cases are clear—if the coherency is 0 at all frequencies, then the time series are statistically independent, whereas if the coherency is 1 at all frequencies, then the times series are identical within a scale factor. The difficultly arises in understanding the meaning of the coherency between 0 and 1. The report provides an explanation of coherency in terms of the variability of the Fourier phase angles.

The coherency models presented in this report represent the state of knowledge of coherency based on the currently available dense array data. There is only one array on hard rock site conditions that are applicable to many sites in the CEUS. To develop more robust coherency models, data from additional dense arrays on hard rock sites need to be collected.

Approach

Investigators evaluated ground motions from 10 dense arrays with minimum station spacing of less than 70 m. The arrays are located on a range of site conditions, including both soil and rock sites. The Pinyon Flat data represents the best available dense array data set for hard-rock conditions. While there is a shallow layer of rock above the hard rock at this site, the Pinyon Flat site is the best data set available for developing hard-rock coherency models. The data sets include a wide range of earthquake sources with magnitudes from less than 2.0 to 7.8 and rupture distances from 1 to 100 km.

Keywords

Soil-Structure Interaction (SSI)
Hard-Rock Coherency Model
Spatial Coherency Model
Pinyon Flat Data Array
Lotung Data Array
SMART-1 Array

ABSTRACT

This study describes the development of empirical spatial coherency models for use in soil-structure interaction (SSI) analyses. Ground motions from 10 dense arrays with minimum station spacing of less than 70 m are evaluated. The arrays are located on a range of site conditions, including both soil and rock.

The data sets include a wide range of earthquake sources with magnitudes from less than 2.0 to 7.8 and rupture distances from 1 to 100 km. The observed coherency from all was fit to an initial coherency model and the residuals were then evaluated to test for dependences on the earthquake magnitude, station separation distance, and site condition. No systematic trend with magnitude or distance was found. Coherency models for soil and rock are developed separately; however, the rock coherency model is conservative for application to soil sites or embedded sites.

CONTENTS

x

LIST OF FIGURES

LIST OF TABLES

1
INTRODUCTION

An overview of spatial coherency studies is given by Zerva, and Zervas (2002). Most of the studies of spatial coherency are based on evaluation of the ground motions from the dense array located in Lotung Taiwan due to the extensive database that is available from the SMART 1 array. The SMART-1 array has station spacing of 100-4000m (Abrahamson et al. 1987). Using data from the SMART-1 array, coherency models have been developed by several authors: Abrahamson, (1993), Harichandran and Vanmarcke (1986), Harichandran (1988), Harichandran (1991), Loh (1985), Loh and Yeh (1988), Loh and Lin (1990), Novak (1987), Oliveira et. al. (1991), Ramadan and Novak (1993), Vernon et al. (1991), and Zerva and Zhang (1997). Given the dimensions of the SMART-1 array, these studies have been focused on coherency for station separations that are greater than foundation sizes for nuclear power plants.

To address the spatial variation over dimensions of foundations for nuclear power plants, EPRI supported the installation of the EPRI LSST array, also located in Lotung, Taiwan. The EPRI LSST array is described in Abrahamson et al. (1991) and has station spacings of 3 - 85 m. The spatial coherency from the denser EPRI LSST array data was studied by Abrahamson and Schneider (1988) and Abrahamson et al. (1991).

The SMART-1 and LSST array data provide the largest data sets of dense array data in terms of the number of earthquakes above magnitude 4 and the number of stations. This large data set allows for robust empirical models of the coherency to be developed, but it is not clear that the coherency models from Lotung, Taiwan are applicable to other regions. This issue was addressed by Abrahamson et. al. (1992). They compared the coherency models developed using the LSST array data with coherency measured from dense arrays in other regions. They found that, other than for sites with strong topography, there was not a significant dependence of the coherency on the site condition or earthquake magnitude; however, there were few rock data available.

A coherency model using both the SMART-1 and LSST data, as well as data from ten other dense arrays, was developed by Abrahamson (1998). This model covers station separations distances of 6-4000m. It was developed as part of the seismic studies for the major toll bridges in California with a focus on the large separations (100-2000m). This report simply lists the equation for the coherency model but does not include a description of how the model was derived.

The objective of the current study is to review the current coherency models and make any modifications needed for application to SSI analyses for nuclear power plants.

In a previous study, Abrahamson (2006) presented coherency models for short separation distances (0-150m) based on surface recordings from a suite of dense arrays located in Taiwan, Japan, and California. Most of these arrays were located on soil or soft-rock sites. The applicability of these data to hard-rock conditions in the EUS has been discussed at review meetings with the NRC. Of the data considered in the previous study, the Pinyon Flat array, described below, is the only hard-rock site. In this report, a new coherency model is derived using only the recordings from the Pinyon Flat array. This data set leads to larger coherency at high frequencies than the model presented in Abrahamson (2006).

2
MATHEMATICAL FORMULATION

Introduction

The spatial variability of the ground motion waveforms can be quantified by the spatial coherency. This section gives the mathematical formulation for estimating the coherency. In Section 3, the estimation of the coherency is described without using equations.

Cross-Spectrum

Let $u_j(t)$ be a recorded ground motion at location j. A window, $v(t)$, is applied to $u_j(t)$ that picks out the strong shaking. The windowed time series is given by $u_j(t)v(t)$. Next, let $u_j(\omega)$ be the Fourier transform of the windowed time series:

$$u_j(\omega) = \sum_{k=1}^{T} v(t_k)u_j(t_k)\exp(-i\omega t_k) \qquad \textbf{Equation 2-1}$$

where T is the number of time samples, t_k is the time of the kth sample, and ω is the frequency (in radians/sec). The cross-spectrum from recordings at sites i and j is a complex number given by $u_i(\omega)\overline{u}_j(\omega)$ where the over-bar indicates the complex conjugate. For coherency estimates, the cross-spectrum is smoothed over a frequency band. The smooth cross-spectrum, Sij, is given by

$$S_{ij}(\omega) = \sum_{m=-M}^{M} a_m u_i(\omega_m)\overline{u}_j(\omega_m) \qquad \textbf{Equation 2-2}$$

where 2M+1 is the number of discrete frequencies used in the smoothing $a_{v\delta}$ a_m are the weights used in the frequency smoothing. In this evaluation of coherency, a Hamming window is used for the frequency smoothing (a_m). The Hamming window is shown in Figure 2-1; it is a smoothed version of a triangle window.

In the selection of the frequency smoothing, there is a trade-off between the frequency resolution and the bias and uncertainty. Smoothing over a small number of frequencies leads to high resolution in frequency but also leads to large bias and large variability. Smoothing over a large number of frequencies gives poor resolution in frequency, but leads to small bias and small variability. That is, smoothing over a larger number of frequencies leads to robust coherency estimates, but poor resolution. For this analysis, I selected 11-point frequency smoothing. Therefore, the complex cross spectrum in Equation 2-3 is averaged over 11 frequencies.
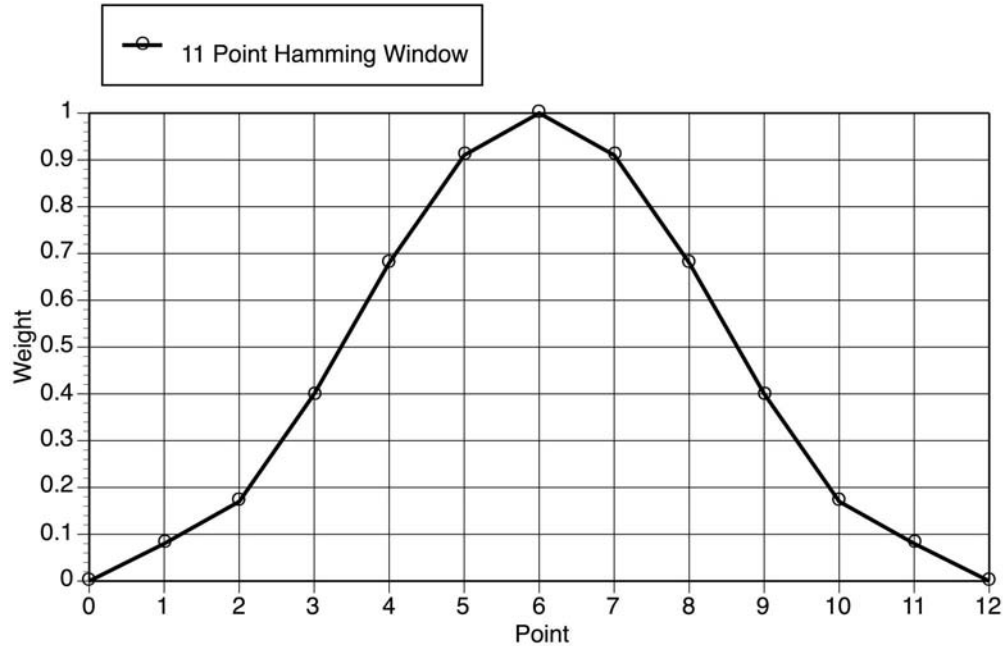
Figure 2-1
Example of a Hamming Window

Complex Coherency

The complex coherency, $\gamma_{ij}(\omega)$, is given by the ratio of the smoothed cross-spectrum to the geometric mean of the auto power spectra.

$$\gamma_{ij}(\omega) = \frac{S_{ij}(\omega)}{\sqrt{S_{ii}(\omega)S_{jj}(\omega)}}$$

Equation 2-3

There are several ways the coherency can be described: lagged coherency, plane-wave coherency, and unlagged coherency. These three measures of coherency are described below.

Lagged Coherency

The lagged coherency is the most commonly cited coherency measure and is given by the modulus of the complex coherency, $|\gamma|$. The lagged coherency can be thought of as the similarity of two time histories after aligning the time series using the time lag that leads to the largest correlation of the two ground motions for a specific frequency band. There is no requirement that the time lags be consistent between frequencies. For example, the optimal time shift for 5-8 Hz may be different than the optimal time shift for 12-15 Hz.

In general, the lagged coherency does not go to zero at large separations and high frequencies due to the bias in the estimate of the lagged coherency. Even if the coherency is zero, the estimate of the lagged coherency will be non-zero due to bias in the estimation.

For a small amount of frequency smoothing, the computed lagged coherency depends strongly on the selected frequency smoothing. If no frequency smoothing is used, then the lagged coherency is always unity.

Plane-Wave Coherency

The plane-wave coherency differs from the lagged coherency in that the time shift for each station are constrained to be the same (consistent with a single wave direction and apparent velocity). A systematic delay due to the inclined waves is often called the wave-passage effect. The plane-wave coherency measures the coherency after removing the time lag due to the wave-passage effect. As a result, the plane-wave coherency is less than or equal to the lagged coherency.

The plane-wave coherency is found by taking the real part of the smoothed cross-spectrum after aligning the ground motions based on the best plane-wave speed. Since the real part will have both positive and negative values, the plane–wave coherency will approach zero at high frequencies and large separations. Unlike the lagged coherency, the plane-wave coherency is unbiased.

Since soil-structure interaction analyses generally assume a single include plane wave, the plane wave coherency is consistent with the intended application.

Unlagged Coherency

The unlagged coherency measures the coherency assuming no time lag between locations. This corresponds to the assumption of vertical wave propagation. The unlagged coherency is given by the real part of the smoothed cross-spectrum. The unlagged coherency will be less than or equal to than the plane-wave coherency. For foundation dimensions of a few hundred meters of less, the travel time across the foundation is very small so wave passage effects are not significant and the unlagged coherency will be similar to the plane-wave coherency.

The coherent part of the wav- passage effect can lead to negative values of the unlagged coherency. Negative values indicate that the ground motion at the two stations are out of phase. An unlagged coherency of –1 indicates that the ground motion is 180 degrees out of phase due to wave passage effects. Time Windows

The time window used in this analysis is given by a 5% cosine bell:

$$v(t) = \begin{cases} 0.5\left[\cos\left(\dfrac{t\pi}{0.05W_L} + \pi\right) + 1\right] & for\, t < 0.05W_L \\ \\ 1 & for\, 0.05W_L \le 0.95W_L \\ \\ 0.5\left[\cos\left(\dfrac{\pi(t - 0.95W_L)}{0.05W_L}\right) + 1\right] & for\, t > 0.95W_L \end{cases}$$

Equation 2-4

where W_L is the length of the time window. The results are not sensitive to the shape of the time window used because the variability in the computed coherency between stations, events, and arrays is much larger than the differences due to the shape of the time window.

The wave field consists of P-waves, S-waves, and surface waves. The models in the EPRI studies are for the S-wave window. This window includes the strongest shaking on the horizontal component. The coherency models are given for the horizontal and vertical components. While the horizontal component is dominated by the S-waves, the vertical component will include both P-waves and S-V waves. At high frequencies, the coherency model for the vertical component is greater than the coherency model for the horizontal component. This increase is due to the larger coherencies at high frequencies from P-waves than from S-waves. If the P-wave window was used (excluding the SV waves), then the vertical component coherency would likely be larger at the high frequencies (e.g. above 10 Hz) than the current model, however, the ground motion amplitude is expected to be smaller during P-wave window than it is during the S-wave window. A separate P-wave coherency has not been developed as part of this study.

In addition to the P and S-waves, the wave field may also include surface waves. The surface waves will be low frequency waves for which the coherency model is already near unity.

ATANH Transformation

The plane-wave coherency ranges between -1 and 1. An example of estimated plane-ave coherency is shown in Figure 2-2. This figure shows that the variability of the coherency is not constant. In this example, the variability is small for low frequencies and becomes large for high frequencies. That is, the coherency is heteroscedastic.
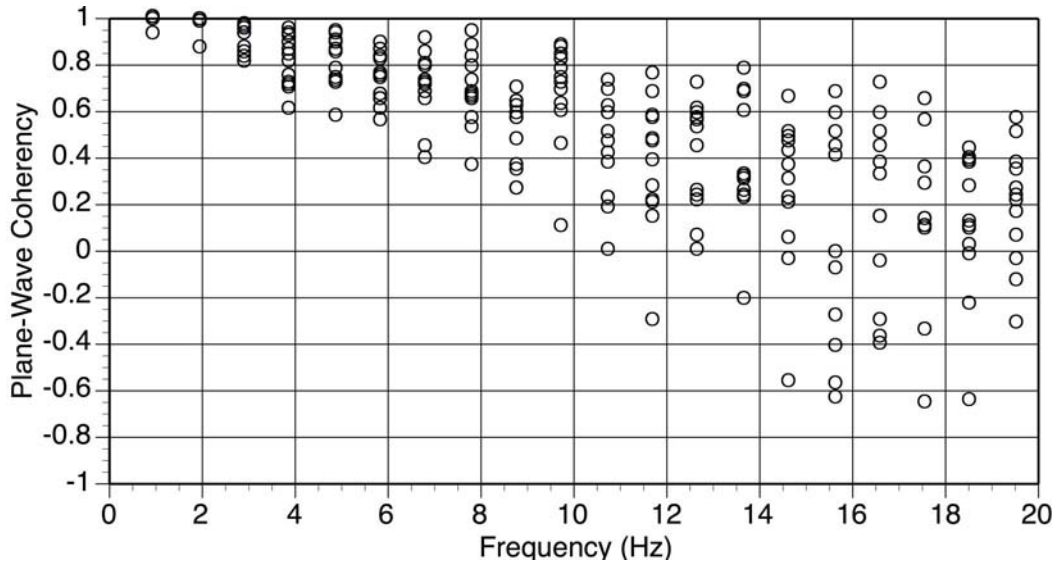
Figure 2-2
Example of Dependence of the Variability of the Plane-Wave Coherency With Frequency

The least squares method of curve fitting is equivalent to the maximum likelihood solution if the data are normally distributed and independent. To take advantage of the computational efficiency of the least-squares method, the coherency should be transformed so that it is approximately normally distributed. A Tanh^{-1} transformation is often applied to the coherency to produce approximately normally distributed data (Enochson and Goodman, 1965). That is, the Tanh^{-1} (γ_{pw}) will be approximately normally distributed about the median Tanh^{-1}(γ_{pw}) curve. An example of the variability of the transformed plane-wave coherency is shown in Figure 2-3. This figures shows that with this transformation the scatter of the coherency is independent of frequency (homoscedastic).
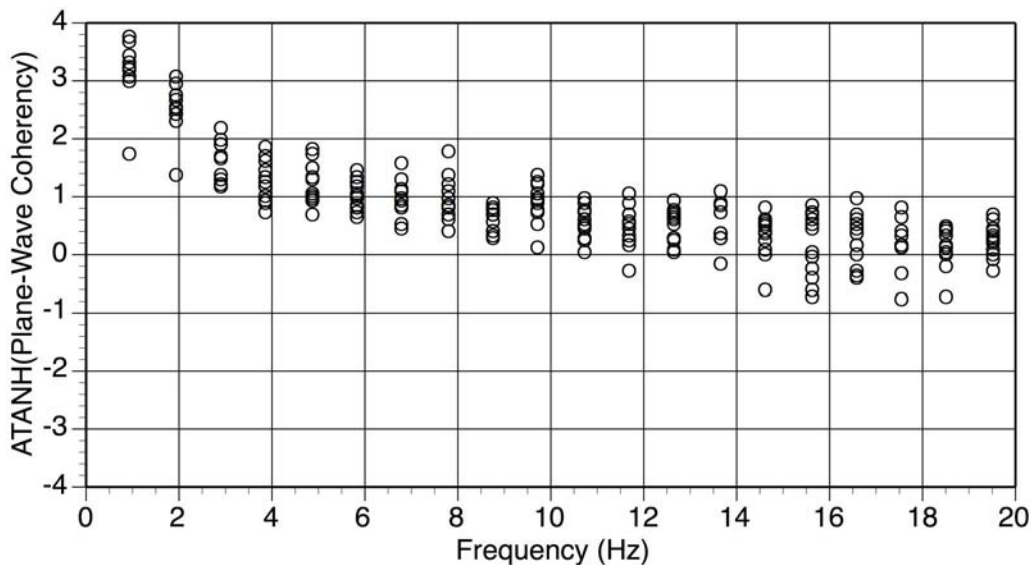
Figure 2-3
Example of Independence of the Variability of the Transformed Plane-Wave Coherency With Frequency

To be consistent in the probabilistic treatment of the ground motion, the mean coherency model should be used. The coherency model described in this report is developed by fitting the Tanh^{-1} (γ_{pw}). The coherency equations give the median coherency. The mean coherency will be different from the median. Examples of the distribution of the coherency assuming a ATANH normal distribution are shown in Figure 2-4. The coherency distributions are skewed to the left (e.g. to lower coherency values). Therefore, the mean coherency will be lower than the median coherency. The mean coherency is shown as a function of the median coherency in Figure 2-5. The difference between the median and the mean is small with the largest difference in the 0.5-0.6 range. Since the difference is small and the median is higher than the mean, it is recommended that the median coherency be used as an estimate for the mean coherency for simplicity.
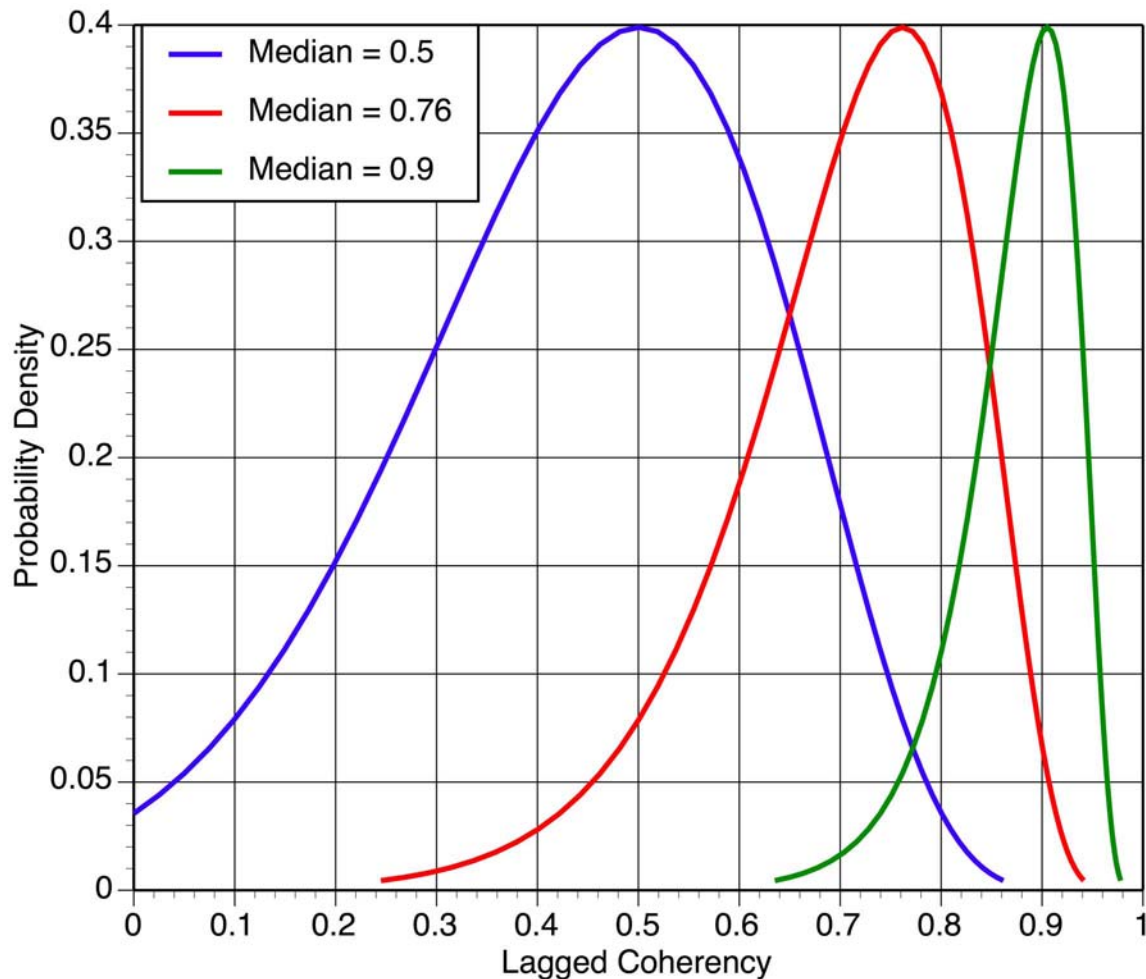
Figure 2-4
Examples of the Distribution of Coherency Assuming a ATANH Normal Distribution With a Standard Deviation of 0.25 ATANH Units
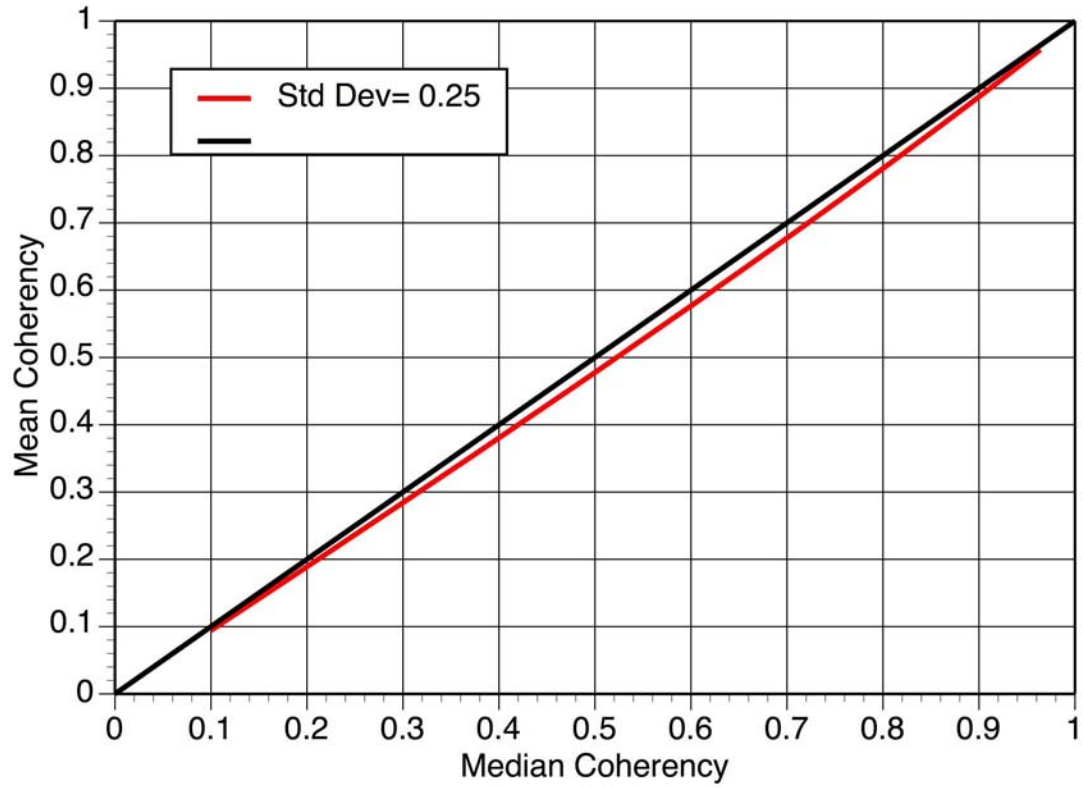
Figure 2-5
Example of the Difference Between the Mean and Median Coherency Assuming a ATANH Normal Distribution With a Standard Deviation of 0.25 ATANH Units

3
DENSE ARRAYS

Introduction

To measure spatial coherency for foundations for NPPS requires a dense arrays with stations separations from 5 to 150 m. There are few dense arrays with such small station separations that have been deployed. Typical seismological dense arrays have station separations of 100s of meters.

Abrahamson (1993) reviewed dense arrays and found 10 arrays with minimum station separations of less than 100m. These dense arrays are listed in Table 3-1. Three of the ten arrays were excluded as described below. First, two of the arrays covered regions with strong topographic variability. The coherency from these arrays was found to be much smaller than for arrays from flat topographic conditions. Therefore, these two arrays were excluded from this study. Second, one array (Stanford temp) did not have accurate relative timing between station which is required to compute the plane-wave coherency. Therefore, this array was excluded. The earthquakes recorded by the remaining seven arrays are summarized in Table 3-2.

Table 3-1
Candidate Dense Arrays (Min Separation < 100 m)

Array	Location	Site Class	Topography	Number of Stations	Station Separation (m)
EPRI LSST	Taiwan	Soil	Flat	15	3 – 85
EPRI Parkfield	CA	Soft-Rock	Flat	13	10 – 191
Chiba	Japan	Soil	Flat	15	5 – 319
USGS Parkfield	CA	Soft Rock	Multiple Ridge Tops	14	25 – 952
Imperial Valley Differential	CA	Soil	Flat	5	18 – 213
Hollister Differential	CA	Soil	Flat	4	61 – 256
Stanford (Temp)	CA	Soil	Flat	4	32 – 185
Coalinga (Temp)	CA	Soft-Rock	Single ridge	7	48 – 313
UCSC ZIYA (Temp)	CA	Soft-Rock	Mountains	6	25 – 300
Pinyon Flat (Temp)	CA	Hard-Rock	Flat	58	7 – 340

Table 3-2
Summary of Earthquakes from the Selected Dense Arrays

Array	No. of Earthquakes	Magnitudes	Epicentral Distances (km)	Maximum PGA (g)
EPRI LSST	13	3.0 – 7.8	5-113	0.26
EPRI Parkfield	2	3.0 – 3.9	13-15	0.04
Chiba	9	4.8 – 6.7	61-105	0.41
Imperial Valley Differential	2	5.1 – 6.5	4-10*	0.89
Hollister Differential	2-3?	5.5-6.2	15-53	0.20
Coalinga (Temp)	4	3.2-5.2	1-5	0.21
Pinyon Flat (Temp)	5	2.0 – 3.6	14-39	0.03

* Rupture distance (km)

EPRI/Taipower LSST Array

The Lotung LSST array is located in northeastern Taiwan near the town of Lotung (Figure 3-1). It is located at the southern end of the Lanyang River plain. The array was installed in 1985 as part of a joint program by EPRI and Taipower. The earthquakes recorded by the array are listed in Table 3-3.

The array consists of free-field surface, free-field down-hole, and structure instruments. The surface array consists 15 three-component force balanced accelerometers. The surface stations are configured in a Y-shaped array with an 85 m radius (Figure 3-2). To avoid soil-structure interaction effects on the coherency, the station closest to the structure on each arm was not used in the analysis. The topography in the array region is flat.

The down-hole array consists of two vertical arrays located under stations FA1-1 and FA1-5. There are stations at four depths: 5 m, 11m, 17m, and 47m. There is a just one station pair at each depth. The downhole array configuration is shown in Figure 3-3.

Extensive in situ and laboratory studies were conducted to define the soil stratigraphy and geotechnical properties beneath the LSST array (Anderson and Tang, 1987). A total of 12 drill holes to depths of from 30 to 150 m were sampled. In the top 50 m, the S-wave velocities from cross-hole and u-hole seismic tests is 100 m/s near the surface and increases to 250 m/s at 18 m depth. It remains 250/s to a depth of 50 m. The average shear-wave velocity in the top 30 m is 210 m/s. The results of laboratory tests also indicate that the shear modulus and damping becomes nonlinear at shear strains of about 10^{-2}%. Recent observations of vertical transfer functions obtained from selected LSST recorded earthquakes suggest that nonlinearity is significant at accelerations of about 0.15g (Chang et al., 1989). This site is classified as a soil site.
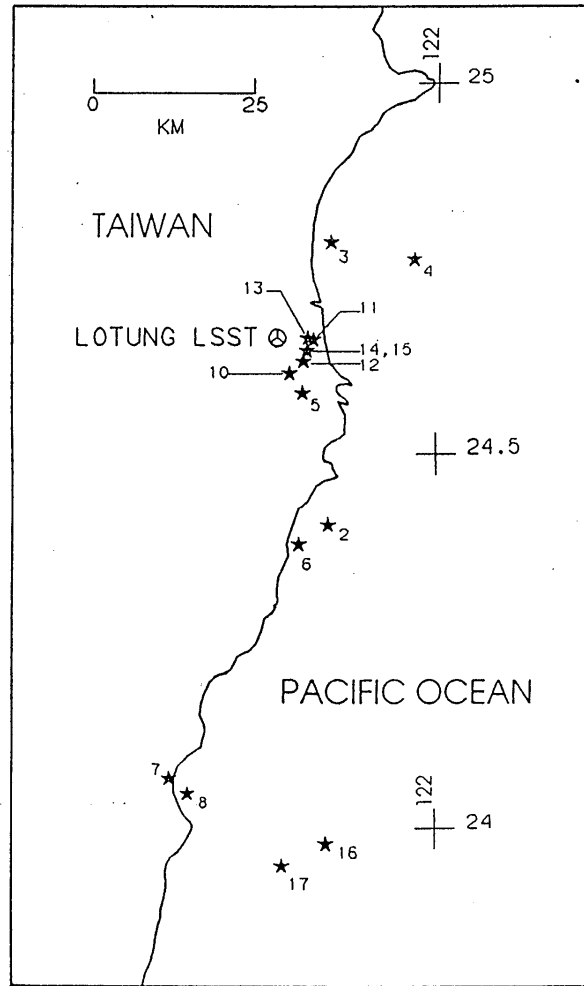
Figure 3-1
Location of the LSST Array and Epicenters of Recorded Events

Table 3-3
Events Recorded by the LSST Array

Event Name	Date	Time	M	Epicentral Dist (km)	Depth (km)	Az (degrees)	No. Stations
event 2	10/26/85		4.6	29	1	165	7
event 3	11/07/85		4.7	81	79	30	11
event 4	1/16/86		6.0	26	10	61	10
event 5	3/29/86		3.9	13	10	159	12
event 6	4/08/86		4.3	33	11	174	11
event 7	5/20/86		6.4	71	16	195	11
event 8	5/20/86		5.5	72	22	192	11
event 10	7/16/86		3.7	6	1	162	10
event 11	7/17/86		4.1	6	2	90	10
event 12	7/30/86		5.6	4	2	131	12
event 13	7/30/86		-	5	-	90	12
event 14	7/30/86		4.1	5	2	119	10
event 15	8/05/86		-	5	-	120	10
event 16	11/14/86		7.8	68	7	174	9
event 17	11/14/86		6.3	80	-	180	9

EPRI/Taipower Lotung Array
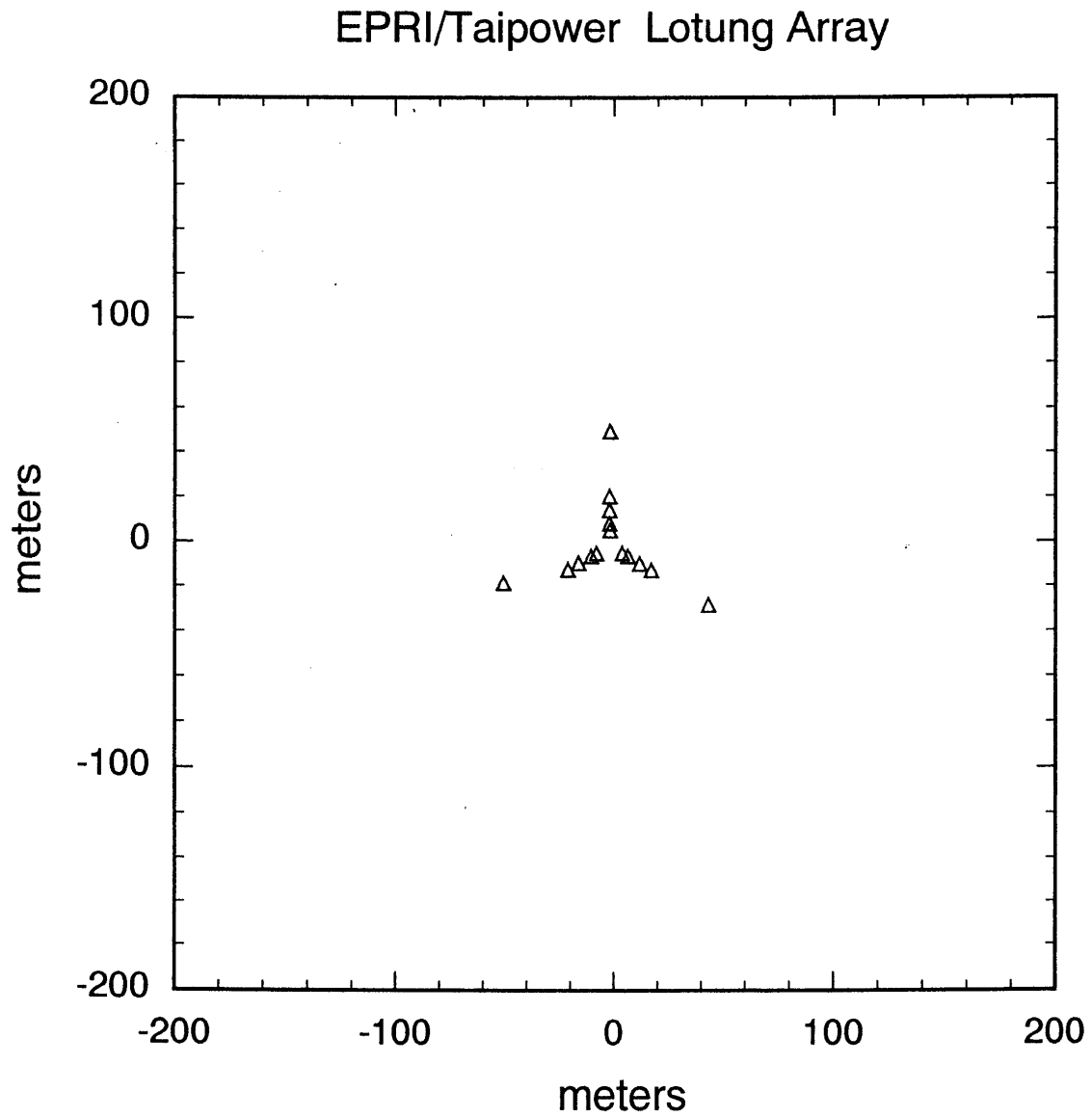
Figure 3-2
Configuration of the LSST Array
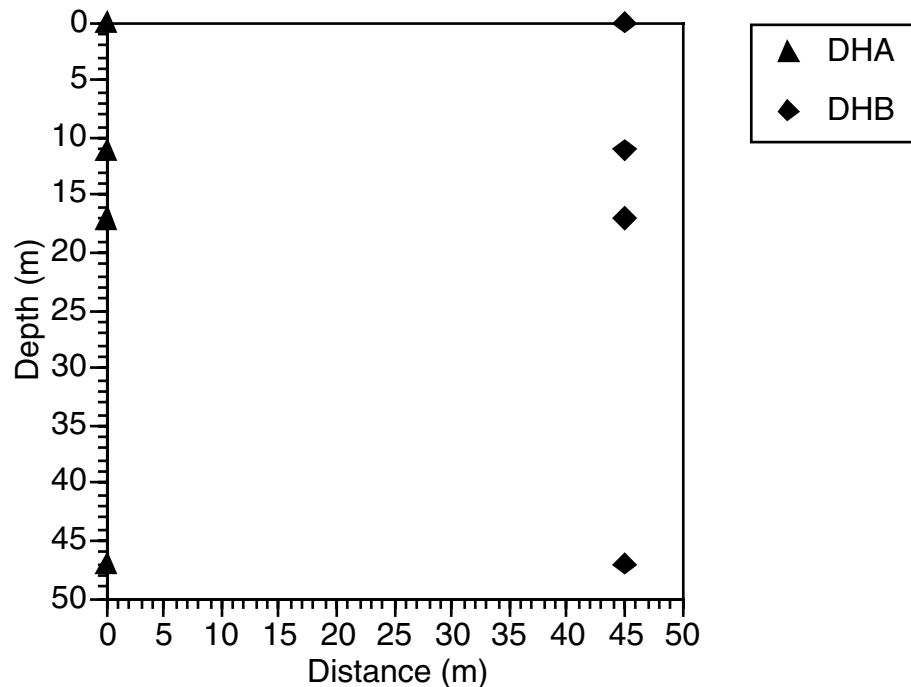
Figure 3-3
Configuration of the EPRI LSST Downhole Array

EPRI Parkfield Array

In anticipation of the rupture of the Parkfield segment of the San Andreas fault, EPRI installed a dense strong motion array at Stone Corral, about 15 km southeast of Parkfield (Figure 3-4). The array is located 7 km east of the San Andreas Fault along the rupture zone of the 1966 Parkfield earthquake. The array was operation from 1987 to 1994. Unfortunately, the funding for the operation of the array was discontinued before the occurrence of the 2004 Parkfield earthquake. The earthquakes recorded by the array are listed in Table 3-4.

The array consists of 21 three-component force-balanced accelerometers connected to a central recording facility on site. There are 13 surface and 8 downhole elements distributed to 90 m depth. The surface stations are configured in a Y-shaped array with a 120 m radius (Figure 3-5). The topography in the array region is fairly flat.

The downhole array consists of four station at a depth of 15 m and four stations at depths of 30, 60, and 90 m under the center station. The 15 m depth is the only depth with more than one station, allowing a coherency at depth to be computed. The configuration of the stations at 15 m depth is shown in Figure 3-6.
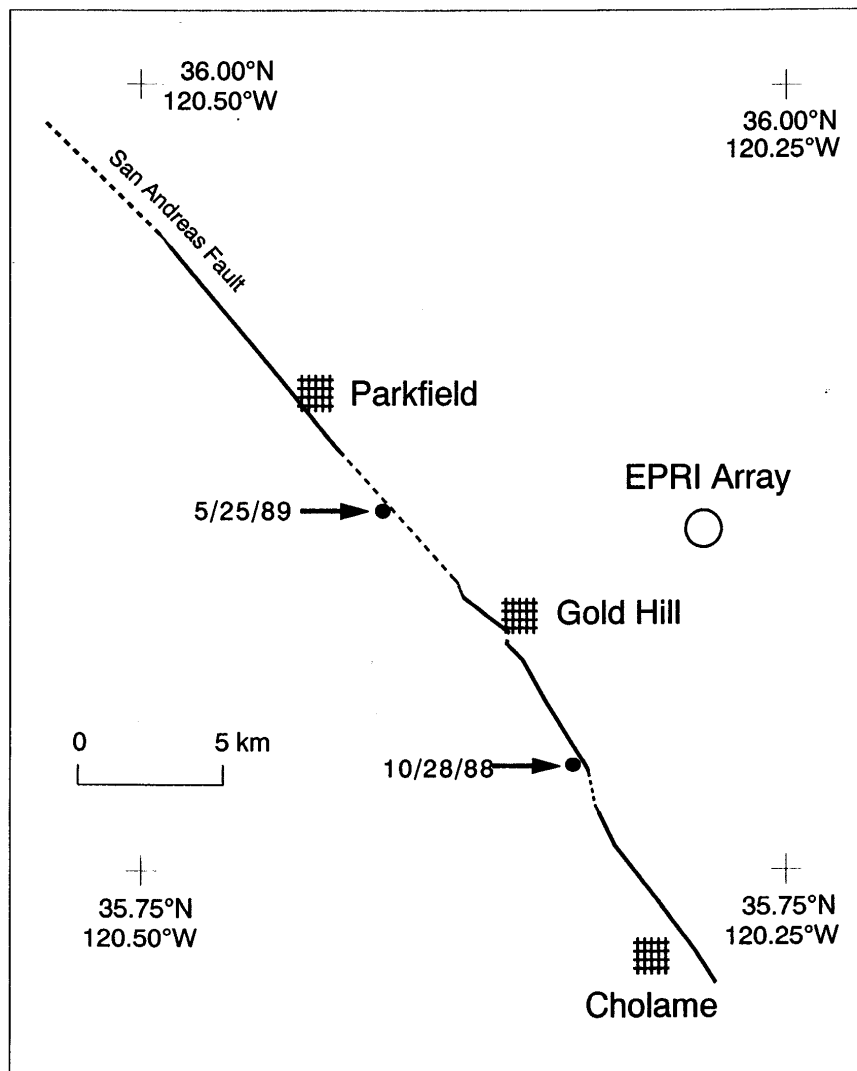
Figure 3-4
Location of the EPRI Parkfield Array and Epicenters of Recorded Events

Table 3-4
Events Recorded by the EPRI Parkfield Array

Event Name	Date	Time	M	Epicentral Dist (km)	Depth (km)	Az (degrees)	No. Stations
event 1	10/23/88	00:00	3.0	9	9	210	13
event 2	5/25/89	00:00	3.9	12	9	275	10

EPRI Parkfield Array
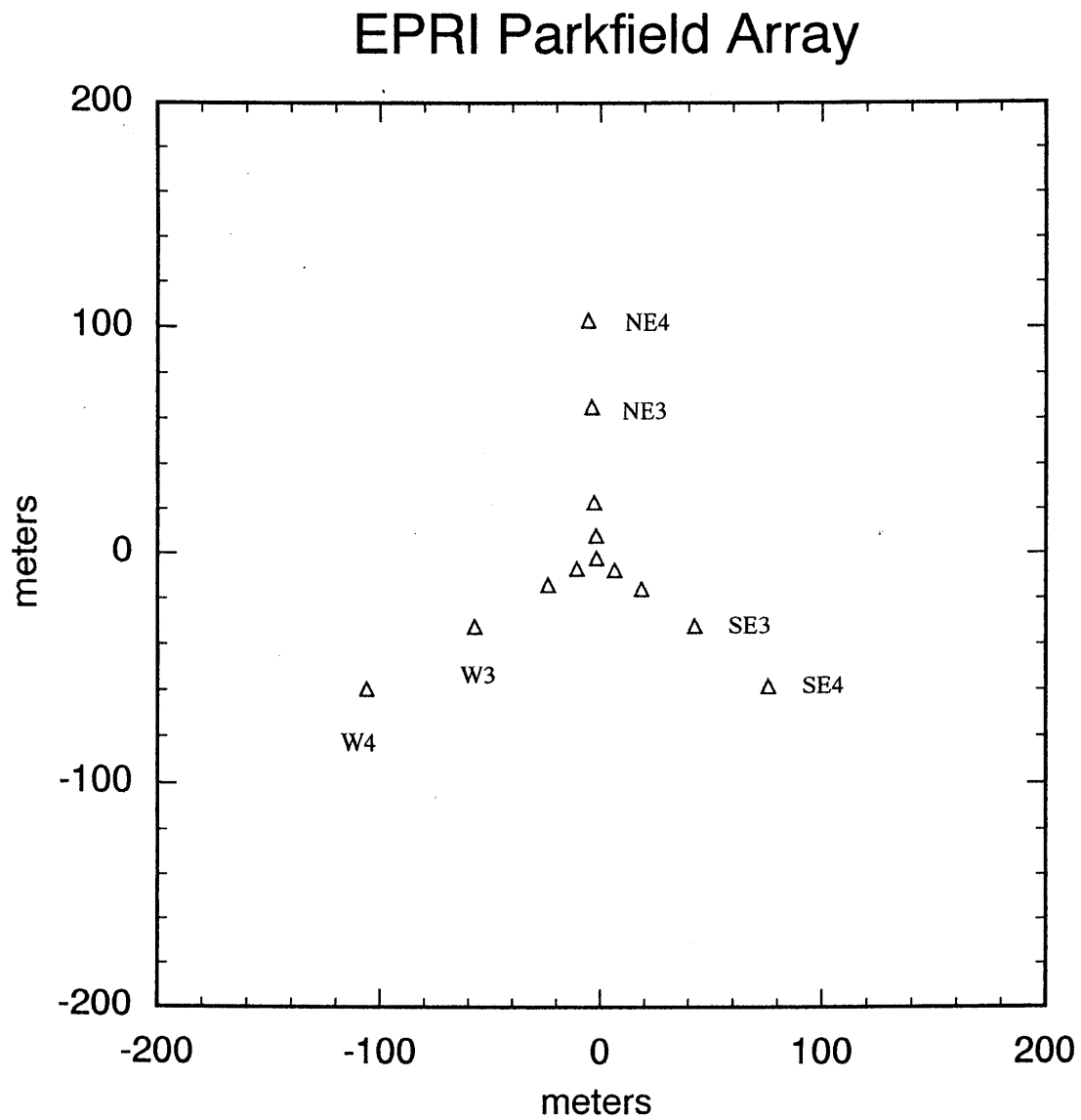
Figure 3-5
Configuration of the EPRI Parkfield Array
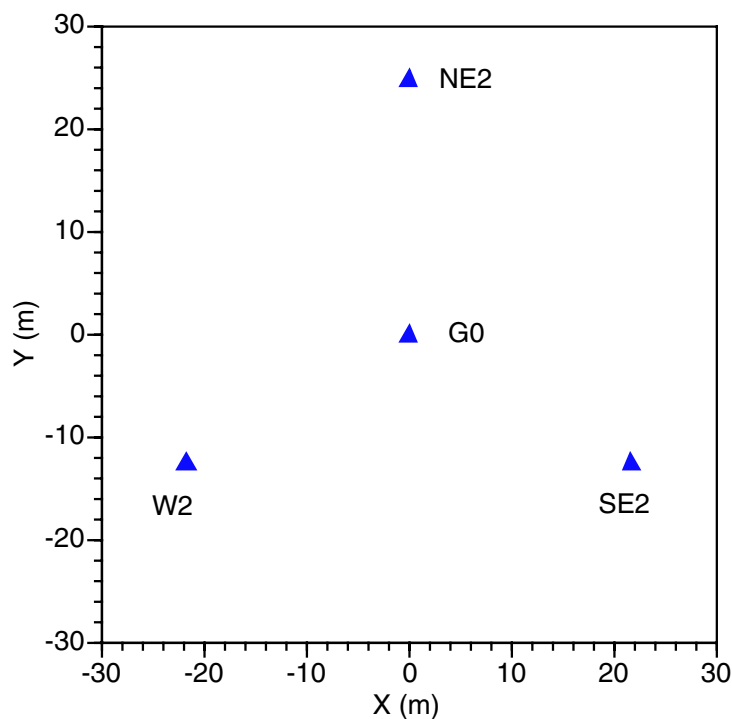
Figure 3-6
Configuration of the EPRI Parkfield Stations at a Depth of 15 m

The site has been characterized using a variety of geotechnical methods (EPRI RP2556-40):
1) Reconnaissance geologic mapping of surface exposures; 2) stratigraphic mapping and mineralogic analysis from drilling and coring of 4 6-cm boreholes to a maximum depth of 120 m; 3) uphole-downhole seismic velocity profiling for P and S waves to 90 m depth; and 4) seismic refraction analysis from four profiles extending parallel and perpendicular to structure and extending from 180 m to 460 m in length. The refraction data yield P-wave velocity information to about 150 m depth throughout the array.

The site array site is located in a complex tectonic block on the northeast side of the San Andreas Fault. The deep basement in the area is composed of pervasively sheared Franciscan and related ultramafic rocks of Mesozoic age. The basement rocks are overlain by about 5000 m of Tertiary and Cretaceous marine sedimentary rocks. The basement and overlying meta-sedimentary rocks have been progressively transposed into a series of NW-SE trending en echelon folds and faulted folds, probably in response to the right-lateral shear associated with the San Andreas Fault system.

The central portion of the seismic array is located on an old (> 10,000 years) alluvial deposit which is up to about 6 m thick. The bedrock underlying and surrounding the array is predominantly sandstone of the Miocene Temblor Formation (Diblee, 1971). A small area of mudstone and siltstone is also mapped at the surface in the northwestern portion of the array. The array is located on the eastern limb of a steep, NW plunging, N40W trending asymmetric syncline. At the array center, the Temblor formation extends from 6m depth to below 90 m, with a bedding plane dip of 70°. This site is classified as a rock site.

Chiba Array

The Chiba array is located at the Chiba experiment station approximately 30 km east of Tokyo (Figure 3-7). The array became operational in April 1982. The Chiba array consists of 15 three-component near-surface accelerometers in an area about 300m x 400m (Figure 3-8). There is a very dense subarray which contains 9 of the 15 stations in an area about 30m x 30m. The near-surface stations are buried at a depth of 1 m. The earthquakes recorded by the array are listed in Table 3-5.
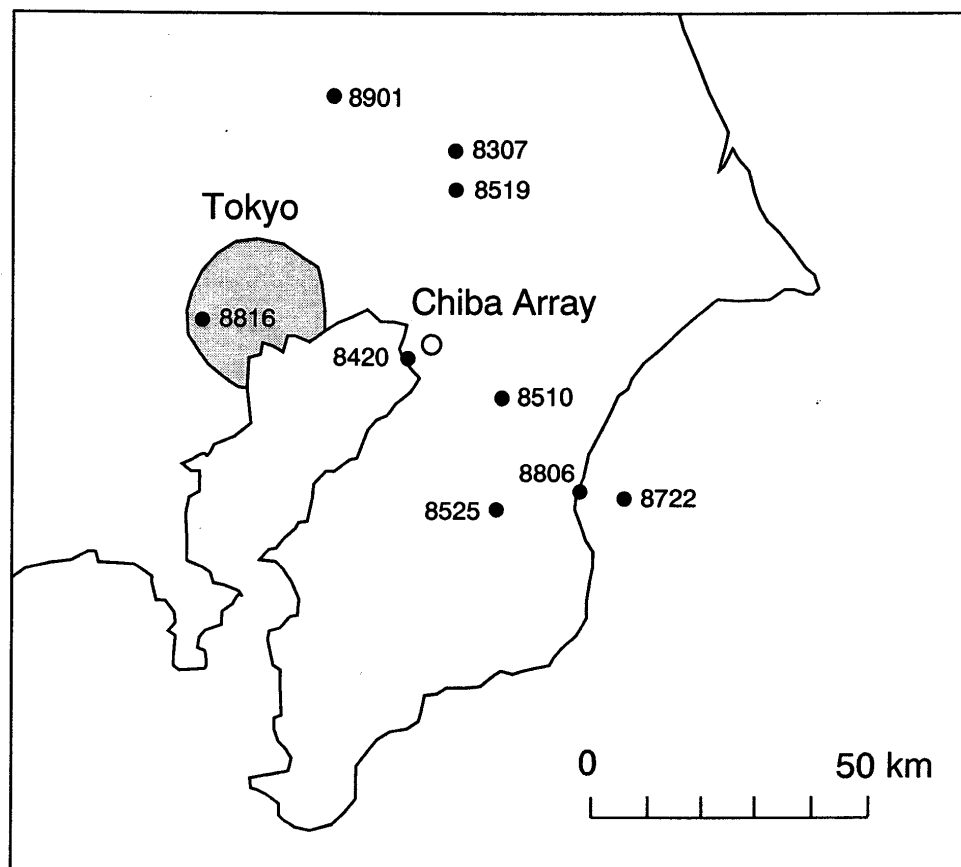
Figure 3-7
Location of the Chiba Array and Epicenters of Recorded Events

Chiba Array
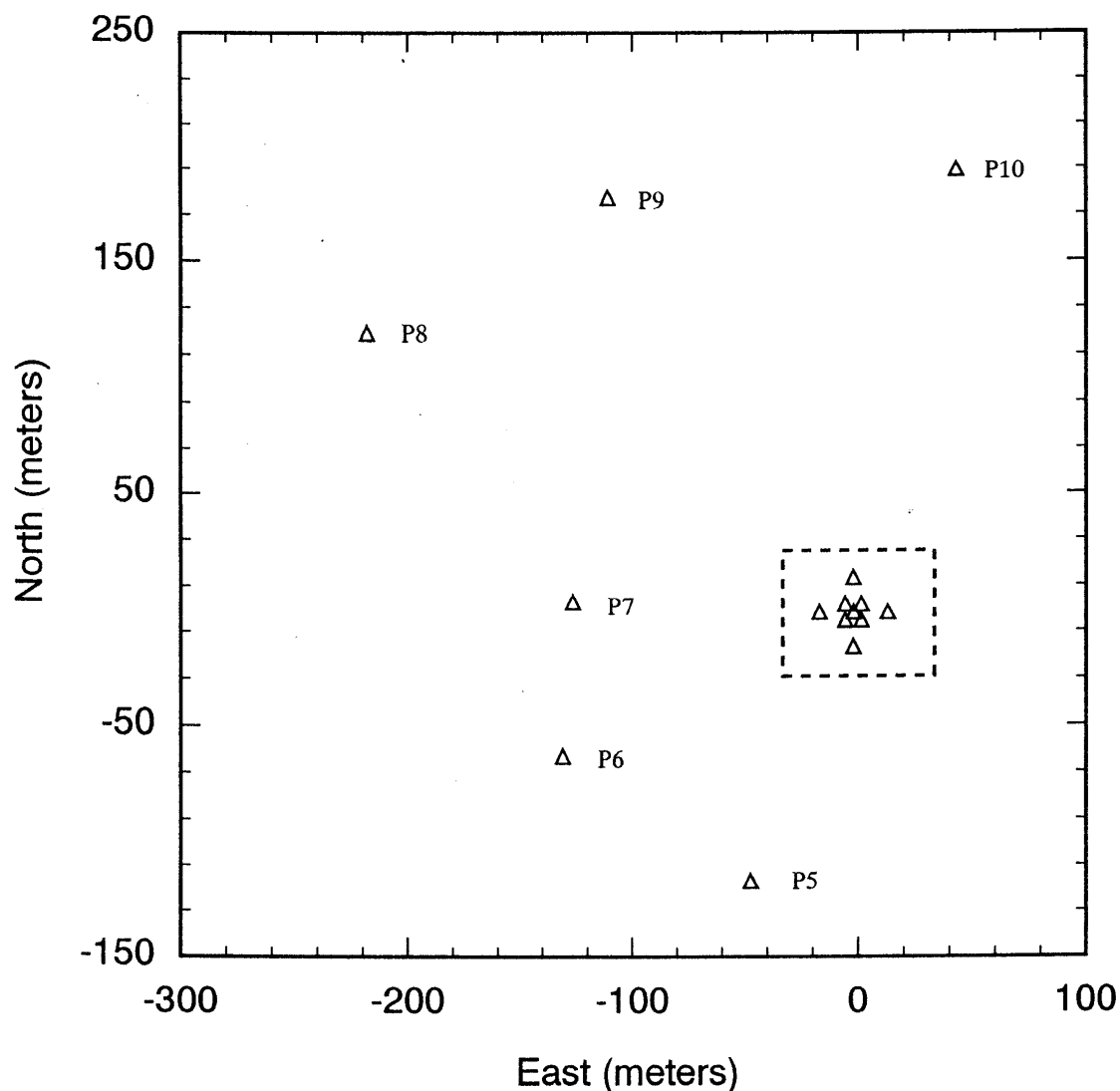
Figure 3-8
Configuration of the Chiba Array

There are also 29 three-component downhole accelerometers at depths of 5, 10, 20, and 40 m.
The are multiple stations at each depth allowing the coherency at depth to be computed. The
configuration of the stations at depth is shown in Figure 3-9.

The topography at the Chiba array is very flat at the array and the soils are uniform. The soil
profile consists of about 3-5 m of loam (140m/s) over about 5 m of sandy clay and clayey sand
(320 m/s). There is more than 30 m of fine sands below the clayey sands (320-420 m/s). The
average shear-wave velocity in the top 30 m is 290 m/s. A complete description of the array
is given by Katayama et al. (1990). This site is classified as a soil site.

Table 3-5
Events Recorded by the Chiba Array

Event Name	Date	Time	M	Epicentral Dist (km)	Depth (km)	Az (degrees)	No Stations
8307	2/27/83		6.0	35	72	353	11
8420	12/17/84		4.9	5	78	120	11
8510	6/8/85		4.8	16	64	234	15
8519	10/4/85		6.1	28	78	351	15
8525	11/16/85		5.0	32	63	202	15
8722	12/17/87		6.7	45	58	232	11
8806	1/16/88		5.2	38	48	226	11
8816	3/18/88		6.0	42	96	84	15
8901	2/19/89		5.6	48	55	22	12
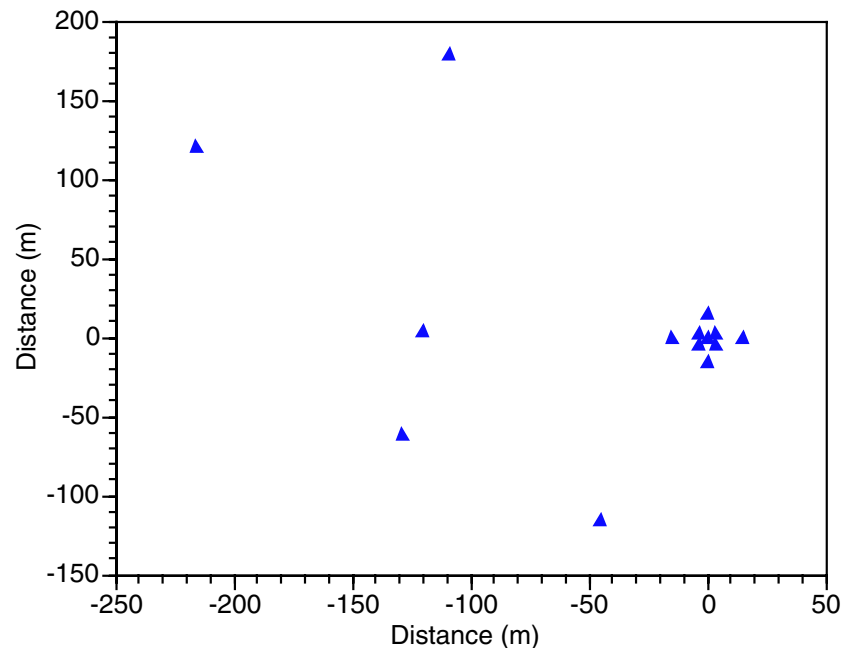
Figure 3-9
Configuration of the Chiba Downhole Stations

Imperial Valley Differential Array

The Imperial Valley Differential array is located in the Imperial Valley, CA about 4 km west of the Imperial Fault (Figure 3-10). This fault was the source of the 1979 Imperial Valley Earthquake. The array consists of 5 three-component force-balanced accelerometers stations. The instruments are configured in a north-south line (Figure 3-11). The earthquakes recorded by the array are listed in Table 3-6.

The array is located at a deep soil site. The surface velocities were measured at the site from drill holes and refraction surveys (Smith et al., 1982). The top 12 m has a shear wave velocity of about 150 m/s. Below this top layer, the shear-wave velocity is about 200 m/s to a depth of about 330 m. The average shear-wave velocity in the top 30 m is 180 m/s. The total depth of the sediments in the Imperial Valley is about 5 km. This site is classified as a soil site.
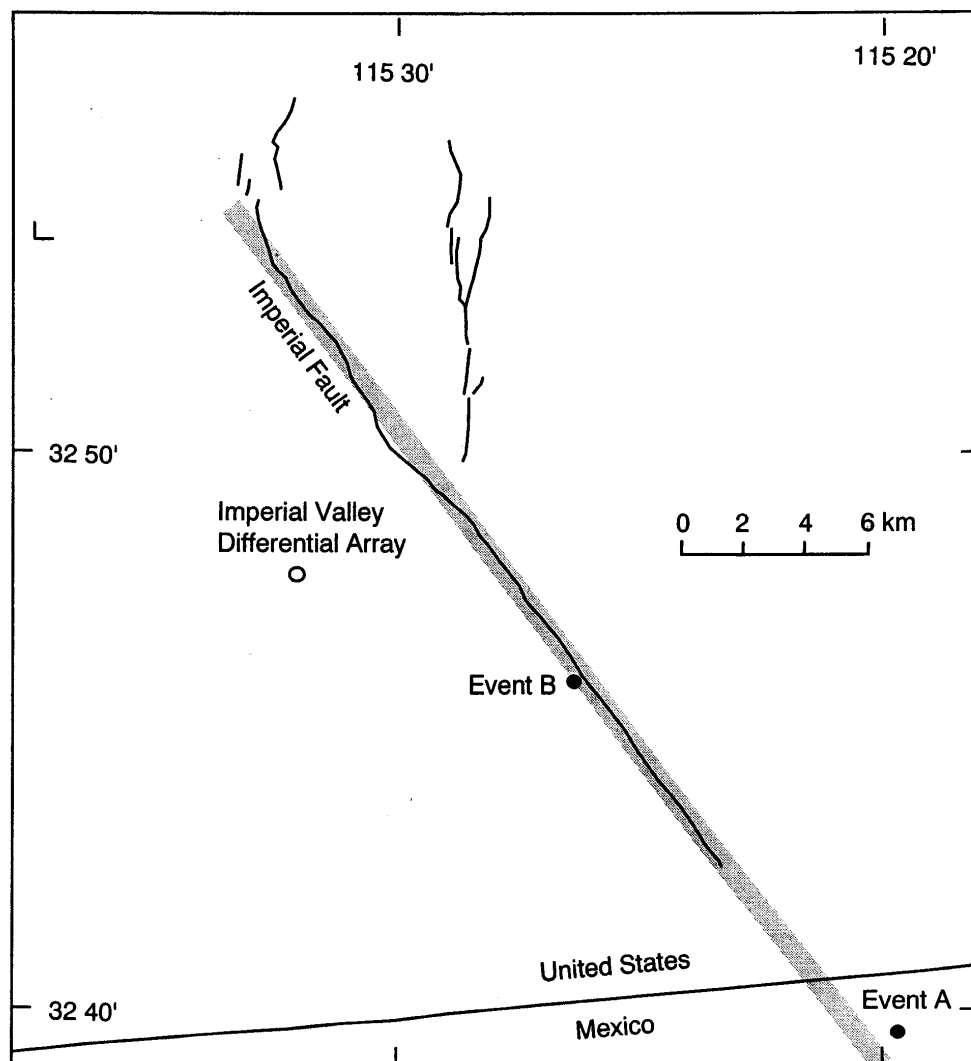
Figure 3-10
Location of the Imperial Valley Differential Array and Epicenters of Recorded Events

Imperial Valley Differential Array
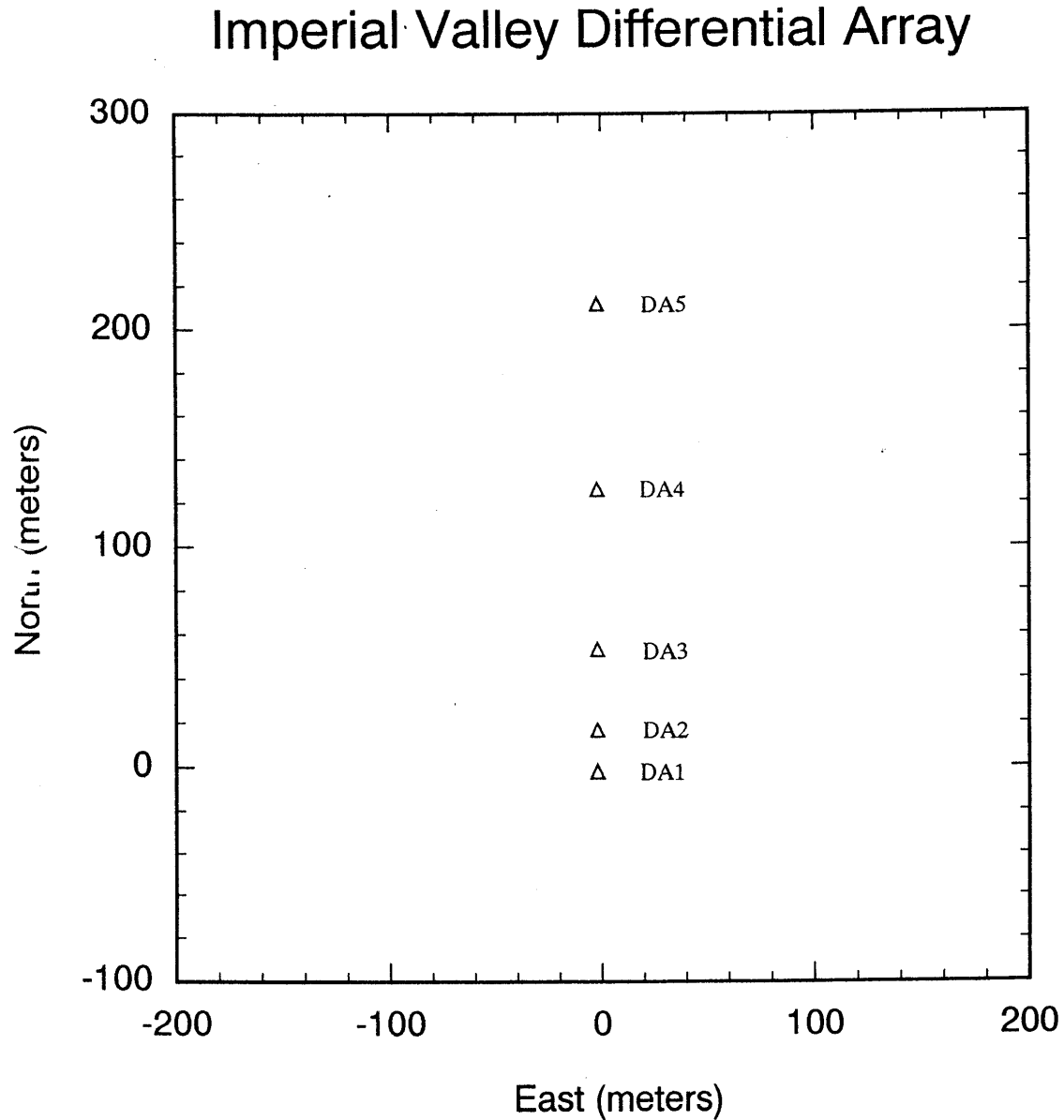
Figure 3-11
Configuration of the Imperial Valley Differential Array

Table 3-6
Events Recorded by the Imperial Valley Differential Array

Event Name	Date	Time	M	Rupture Dist (km)	Depth (km)	Az (degrees)	No. Stations
event A	10/15/79		6.5	4	0	60	4
event B	10/15/79		5.1	10	10	111	5

Event A location given by the closest distance from the site to the fault rupture.

Hollister Differential Array

The Hollister differential array is located at the Hollister airport, CA (Figure 3-12). It is located about 10 km northeast of the San Andreas fault. The array was installed and operated by the USGS. The array consists of 7 three-component accelerometers in a V-shape (Figure 3-13). The lengths of the two arms of the array are 2015m and 1000 m. The earthquakes recorded by the array are listed in Table 3-7.

The topography in the region is flat. The average shear-wave velocity in the top 30 m is 215 m/s (PEER, 2006). This site is classified as a soil site.
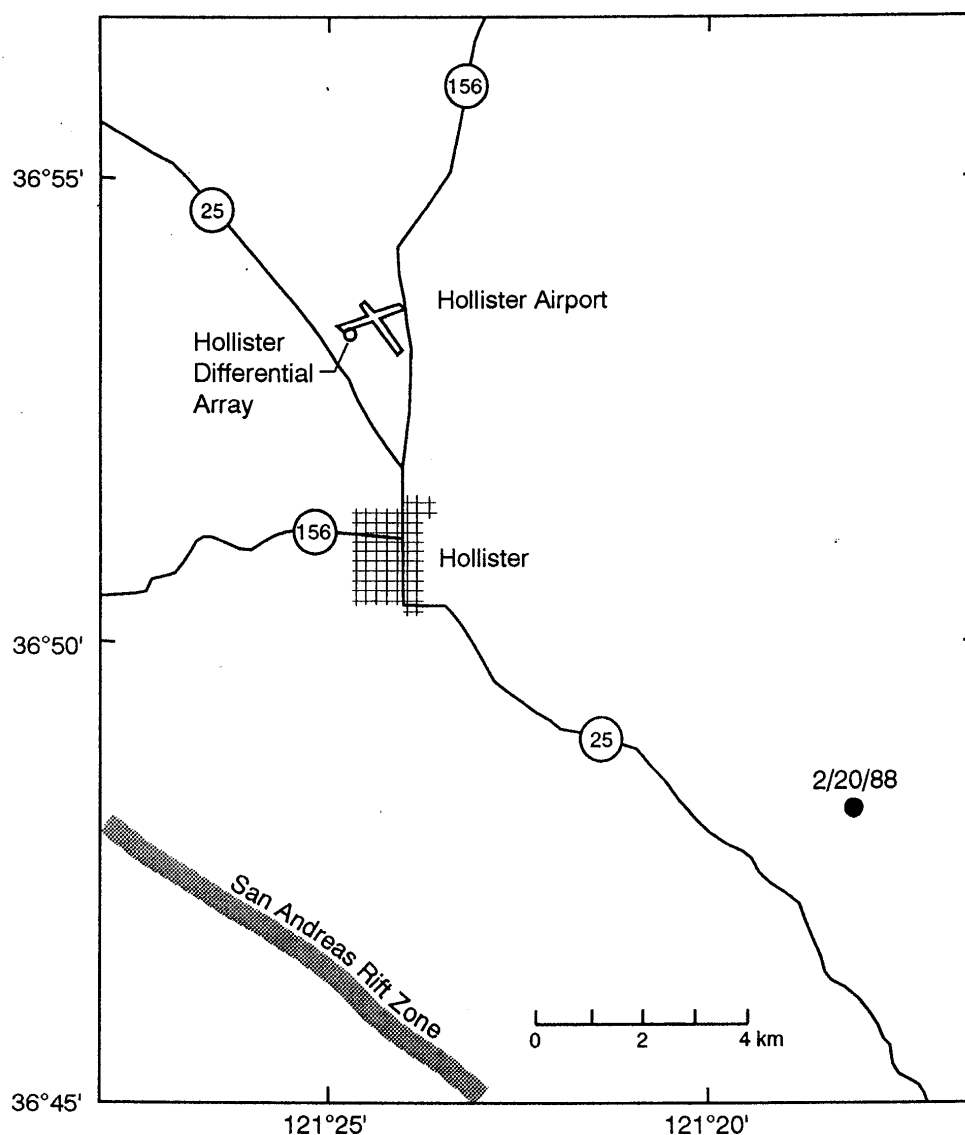
Figure 3-12
Location of the Hollister Differential Array and Epicenters of Recorded Events

Hollister Differential Array
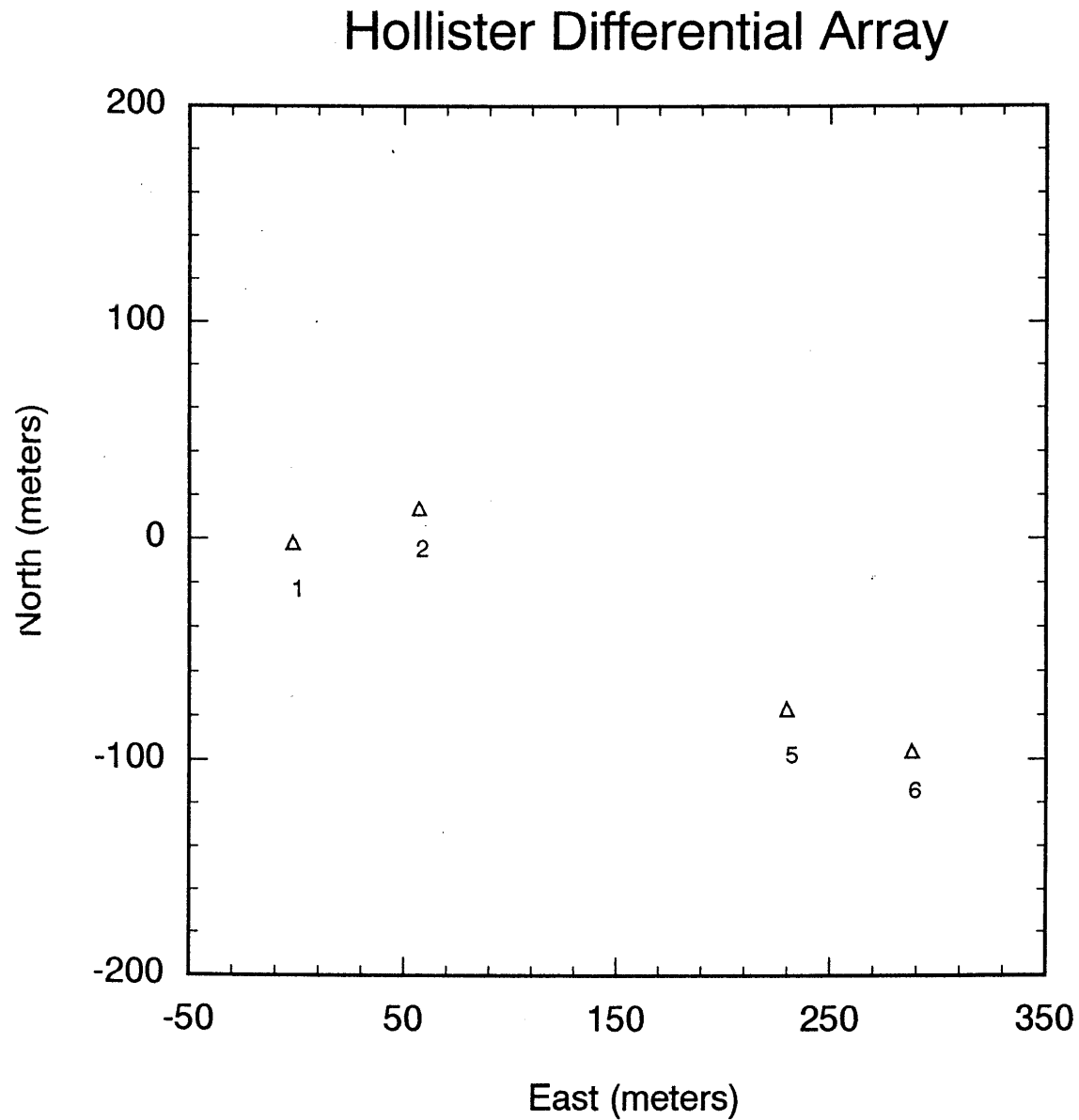
Figure 3-13
Configuration of the Hollister Differential Array

Table 3-7
Events Recorded by the Hollister Differential Array

Event Name	Date	Time	M	Epicentral Dist (km)	Depth (km)	Az (degrees)	No. Stations
event 1	2/20/88		5.3	14	9	136	4
event 2	1/26/86		5.5	15	9		
event 3	4/24/84		6.2	53	9		

Coalinga Temporary Array

The USGS Coalinga Temporary Array was deployed during the aftershock sequence of the 1985 Coalinga earthquake (Mueller et al.,1984). The array is located 10 km north of Coalinga on Anticline ridge (Figure 3-14). The array consists of 7 stations that are a mix of accelerometers and velocity transducers. The instruments are configured in a V-shape array (Figure 3-15). In this study, only the accelerometer data are used. The earthquakes recorded by the array are listed in Table 3-8.

The array is located on the sandstone outcrop along anticline ridge. No other site-specific information on the site velocities is available. For this study, this site is classified as a rock site.
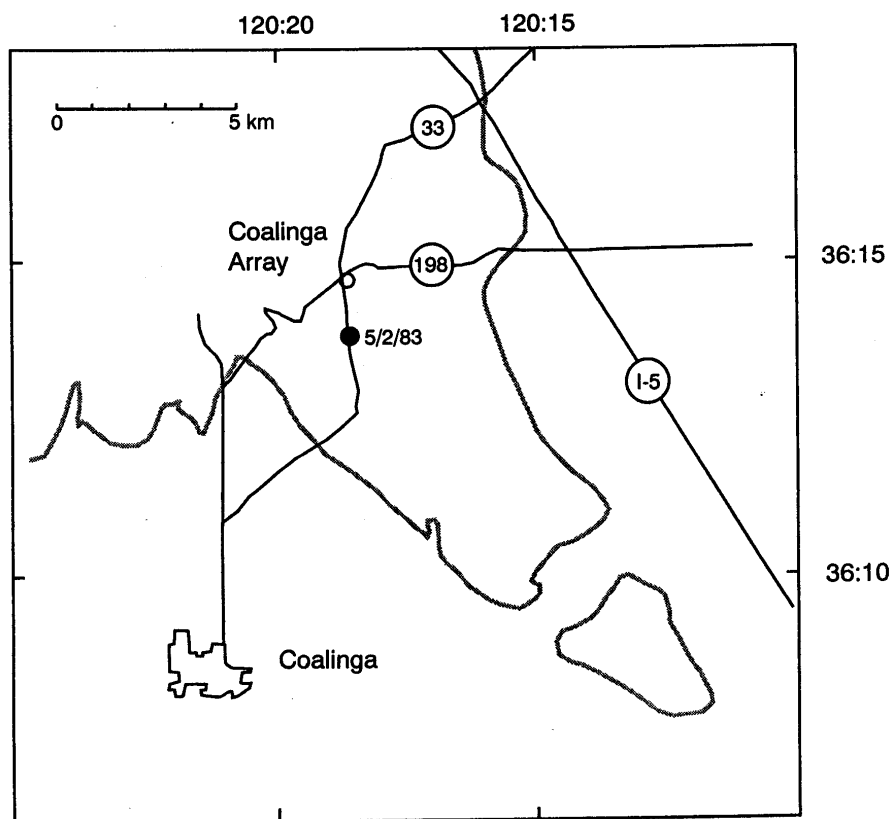
Figure 3-14
Location of the Coalinga Temporary Array and Epicenters of Recorded Events

USGS Coalinga (temp)
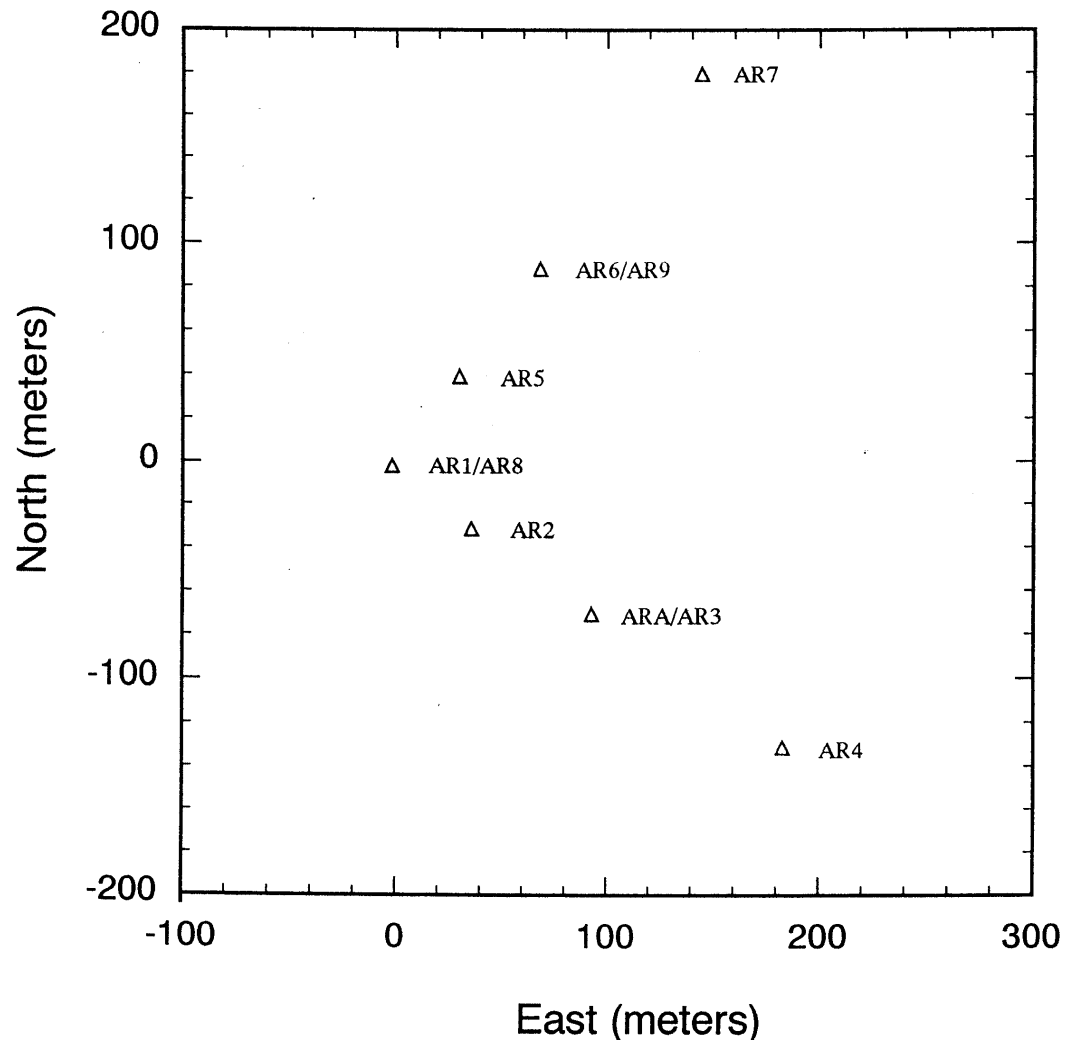
Figure 3-15
Configuration of the Coalinga Temporary Array

Table 3-8
Events Recorded by the Coalinga Temporary Array

Event Name	Date	Time	M	Epicentral Dist (km)	Depth (km)	Az (Degrees)	No. Stations
126E57	5/6/83	04:57	3.3				4
126H43	5/6/83	07:43	2.3				4
126S31	5/6/83	18:31	3.2				4
127A17	5/7/83	00:17	3.2				4
129C49	5/9/83	02:49	5.2	1	12	179	4
129D26	5/9/83	03:26	4.1				4

Pinyon Flat Array

The Pinyon Flat array is located in southern California between the San Jacinto and southern San Andreas Faults (Figure 3-16). The array was deployed as part of a PASSCAL experiment to study wave propagation, scattering, and spatial variations (Owens et al. 1991). The earthquakes recorded by the array are listed in Table 3-9.
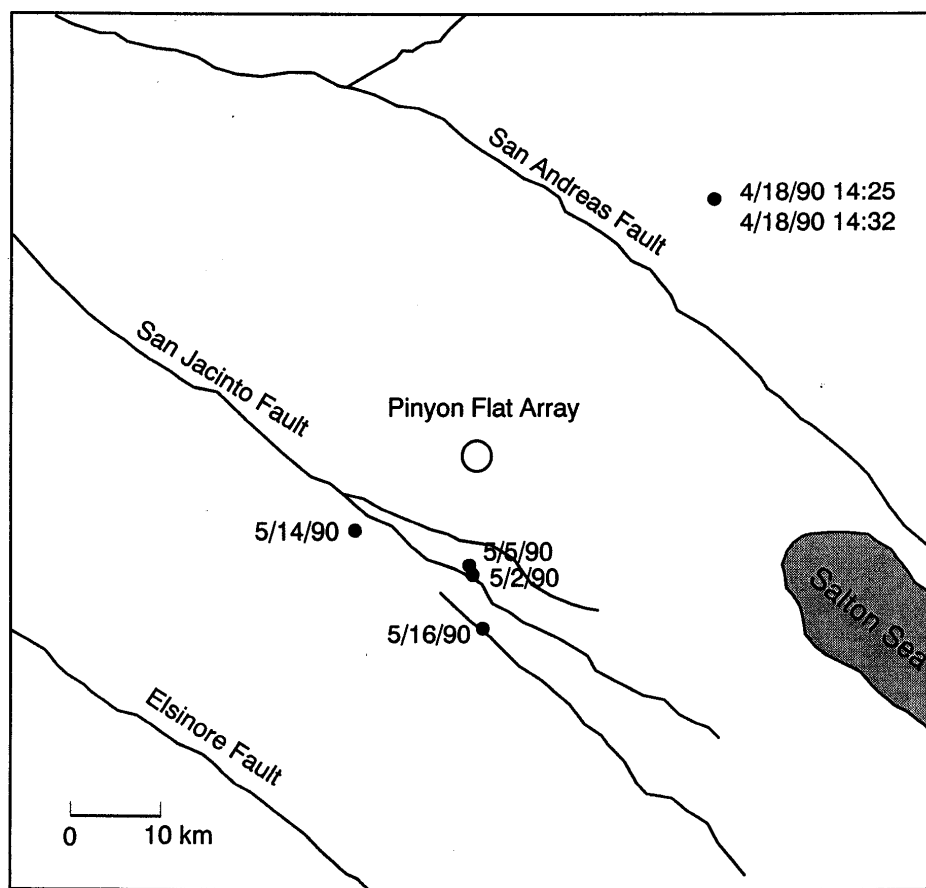
Figure 3-16
Location of the Pinyon Flat Array

The Pinyon Flat array consists of 58 force-balanced accelerometers. The array has two parts. In one part, the instruments are configured in an L-Shaped array and in the second part 36 instruments are configured in a dense grid with 6-7 m spacing (Figure 3-17).

The Pinyon Flat area consists of granite. A shear-wave velocity profile from down-hole measurements (Louie et al., 2002) is shown in Figure 3-18. The top layer is highly weathered. This layer was removed with a backhoe and the instruments were plastered to the rock at depth of 1-3 m below the ground surface. The rock is called "semi-competent rock" by Vernon et al. (1995) since it is still partially weathered at the top. Competent rock, with a shear-wave velocity of 880 m/s, is reached at a depth of 5 m (3 m below the instruments). The shear-wave velocity increases to 1600 m/s at a depth of 13 m. The average shear-wave velocity in the 30 m below the instrument depth is 1030 m/s. The shear-wave velocity profile is shown in Figure 3-18. This site is classified as a hard-rock site.

Table 3-9
Events Recorded by the Pinyon Flat Temporary Array

Event Number	Event Name	Number of Stations
1	90.108/90.108.01.16.51	8
2	90.108/90.108.10.23.27	40
3	90.108/90.108.14.25.58	40
4	90.108/90.108.14.32.41	40
5	90.108/90.108.19.07.21	51
6	90.109/90.109.05.43.34	51
7	90.109/90.109.08.42.55	51
8	90.109/90.109.20.24.52	51
9	90.110/90.110.02.24.45	51
10	90.110/90.110.03.24.54	51
11	90.110/90.110.07.21.01	49
12	90.110/90.110.17.48.02	49
13	90.111/90.111.17.29.03	49
26	90.115/90.115.03.29.27	53
29	90.115/90.115.07.08.28	51
30	90.115/90.115.07.10.58	51
32	90.115/90.115.09.46.24	53
33	90.115/90.115.09.53.30	53
39	90.115/90.115.16.26.39	51
44	90.115/90.115.22.36.37	51
61	90.117/90.117.13.51.16	47
63	90.117/90.117.15.40.10	43
65	90.117/90.117.20.03.12	43
67	90.118/90.118.08.32.30	51
68	90.118/90.118.10.12.04	51
69	90.118/90.118.14.23.11	51
71	90.118/90.118.15.21.32	49
74	90.119/90.119.02.56.08	47
76	90.119/90.119.11.25.57	43
80	90.119/90.119.19.35.48	41
84	90.120/90.120.06.01.41	39
85	90.120/90.120.06.56.22	39
86	90.120/90.120.07.30.46	39
88	90.120/90.120.20.16.54	39
100	90.122/90.122.14.13.10	51
125	90.127/90.127.07.58.05	36
126	90.127/90.127.12.41.00	36
128	90.127/90.127.21.01.53	36
131	90.128/90.128.10.18.33	36
136	90.129/90.129.22.05.28	57
141	90.130/90.130.07.23.31	57
143	90.130/90.130.10.42.12	57
144	90.130/90.130.12.10.41	57

Table 3-9
Events Recorded by the Pinyon Flat Temporary Array (Continued)

Event Number	Event Name	Number of Stations
146	90.130/90.130.14.16.02	57
148	90.130/90.130.14.25.08	57
152	90.130/90.130.15.19.06	57
154	90.130/90.130.15.57.44	57
156	90.130/90.130.17.29.42	55
161	90.131/90.131.00.54.55	55
162	90.131/90.131.00.57.36	55
175	90.132/90.132.15.16.58	50
180	90.132/90.132.19.42.46	50
184	90.132/90.132.23.54.47	55
190	90.134/90.134.05.05.20	57
192	90.134/90.134.07.29.45	55
195	90.134/90.134.11.32.06	57
196	90.134/90.134.11.34.45	57
199	90.135/90.135.00.10.14	57
200	90.135/90.135.02.28.56	57
204	90.135/90.135.13.46.43	57
209	90.136/90.136.01.14.15	57
211	90.136/90.136.04.53.05	55
213	90.136/90.136.18.14.38	53
215	90.137/90.137.02.36.37	53
226	90.138/90.138.12.05.42	51
234	90.139/90.139.06.30.57	53
236	90.139/90.139.09.48.19	53
237	90.139/90.139.11.36.56	53
243	90.140/90.140.01.15.48	53
245	90.140/90.140.04.54.23	53
250	90.141/90.141.14.14.09	53
251	90.142/90.142.00.02.28	53
252	90.142/90.142.03.22.47	53
260	90.144/90.144.00.05.41	49
270	90.145/90.145.03.59.16	56
271	90.145/90.145.04.15.25	56
274	90.145/90.145.12.35.53	54
283	90.147/90.147.11.30.05	48
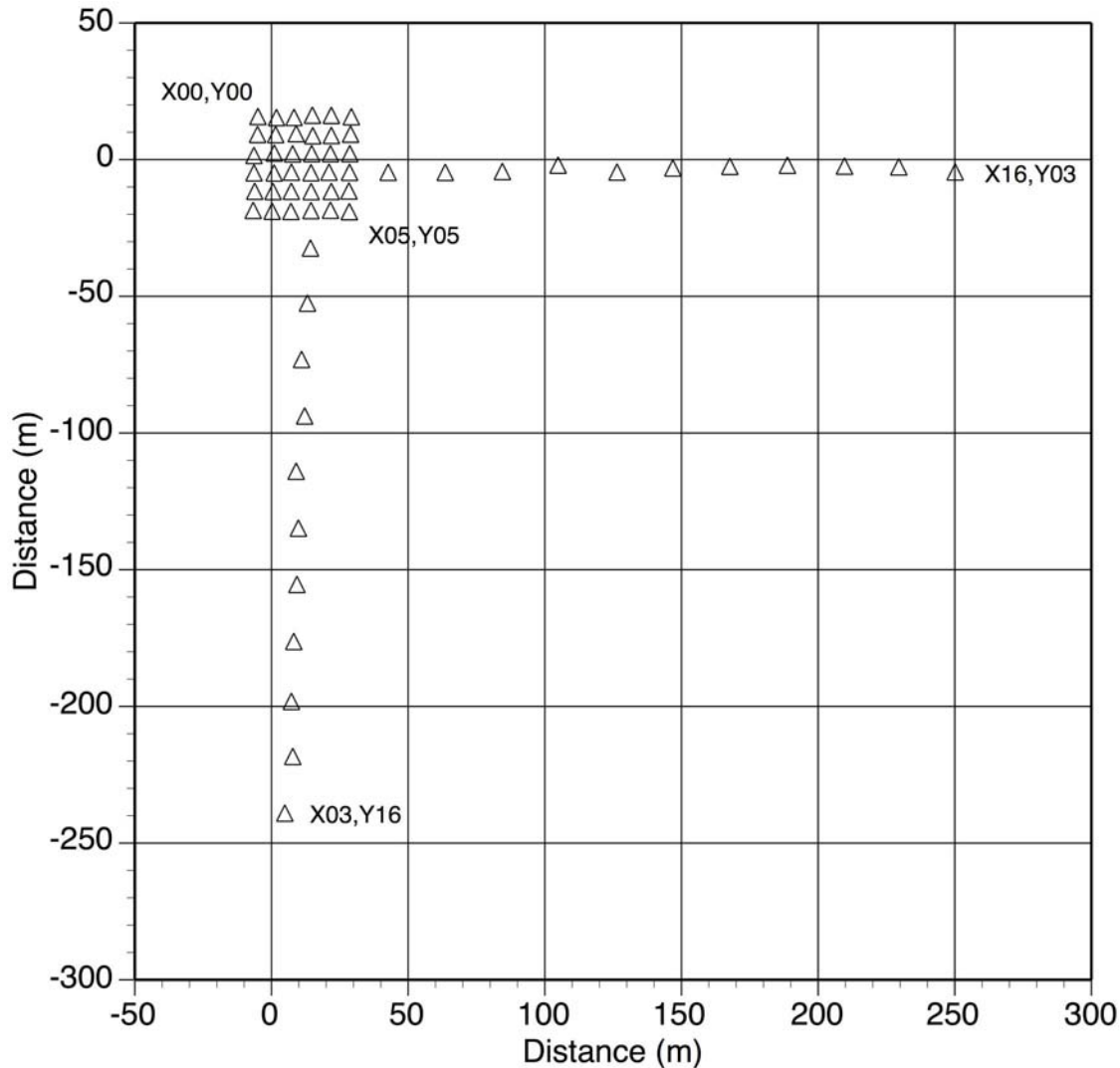
Figure 3-17
Configuration of the Pinyon Flat array

From the 1990 deployment of the dense array at Pinyon Flat (Vernon et al., 1995), there are recordings from 287 earthquakes available through the IRIS data center. The earthquakes magnitudes are all less than 4 with most of these earthquakes from magnitudes less than 2.

From the set of 287 earthquakes, a subset was selected based on the signal in the frequency range of 10 to 40 Hz which is a key frequency range of the application of the coherency model for nuclear power plants. The mean Fourier amplitude spectrum (FAS) of the windowed acceleration for each component was computed for each earthquake. Those earthquakes for which the mean FAS shows good signal to noise in the frequency band 10-40 Hz were selected. The 78 selected earthquakes are listed in Table 3-9. Several of the recordings have a significant noise spike at 60 Hz. To avoid this noise, the data are only used for a maximum frequency of 50 Hz.
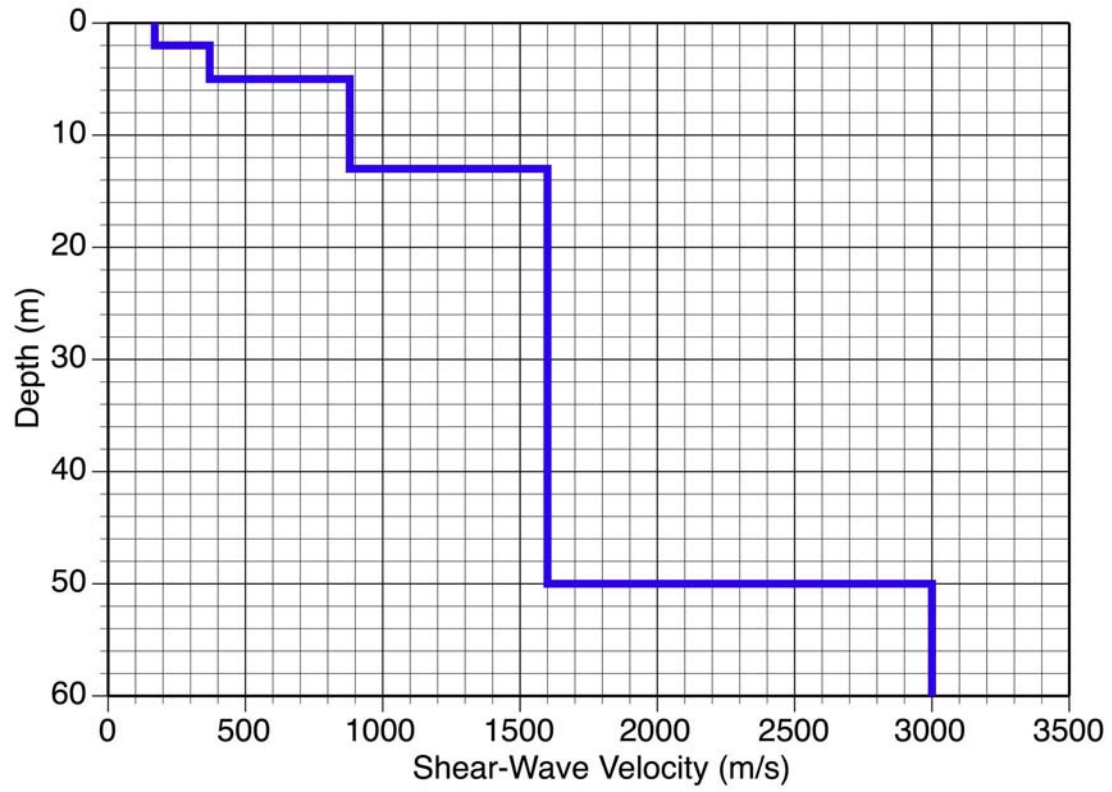
Figure 3-18
Shear-Wave Velocity Profile at the Pinyon Flat Array Based on Down-Hole Measurements

4
UNDERSTANDING COHERENCY

The spatial coherency has not been well understood by the majority of practicing earthquake engineers. The end cases are clear: if the coherency is 0 at all frequencies, then the time series are statistically independent; if the coherency is 1 at all frequencies, then the times series are identical within a scale factor. The difficultly is understanding the meaning of the coherency between 0 and 1.

In this section, I provide a set of examples to explain coherency without using equations. These examples are intended to provide some insights into coherency to give some understanding of what the different values of coherency mean. For the reader that already understands coherency, this section can be skipped.

Cross-Correlation and Coherency

The cross-correlation is a measure of the similarity of two time series. It is a time domain measure that is commonly used and is generally better understood than coherency. The cross-correlation is a good starting point for understanding coherency.

The data from the EPRI Parkfield arrays is used as an example. The cross-correlations are for two earthquakes are shown in Figure 4-1. As the separation distance increases, the cross-correlation decreases. The coherency is compared to the cross-correlation. The coherency model between 10 and 15 Hz is similar to the cross-correlation. This occurs because the Fourier spectrum is peaked in the 10-15 Hz range. If we had used larger magnitude events, then the cross-correlation would be more similar to the coherency at lower frequencies. This is why we use the coherency rather than the cross-correlation.

A key difference between the cross-correlation and the coherency is that the cross-correlation is computed using all frequencies. To estimate the frequency dependence of the cross-correlation, we could band-pass filter the time series before computing the cross-correlation. This is exactly what the coherency is doing when we smooth the cross-spectrum over a frequency band. So, the coherency is the same as the cross-correlation if the same frequency band is used.
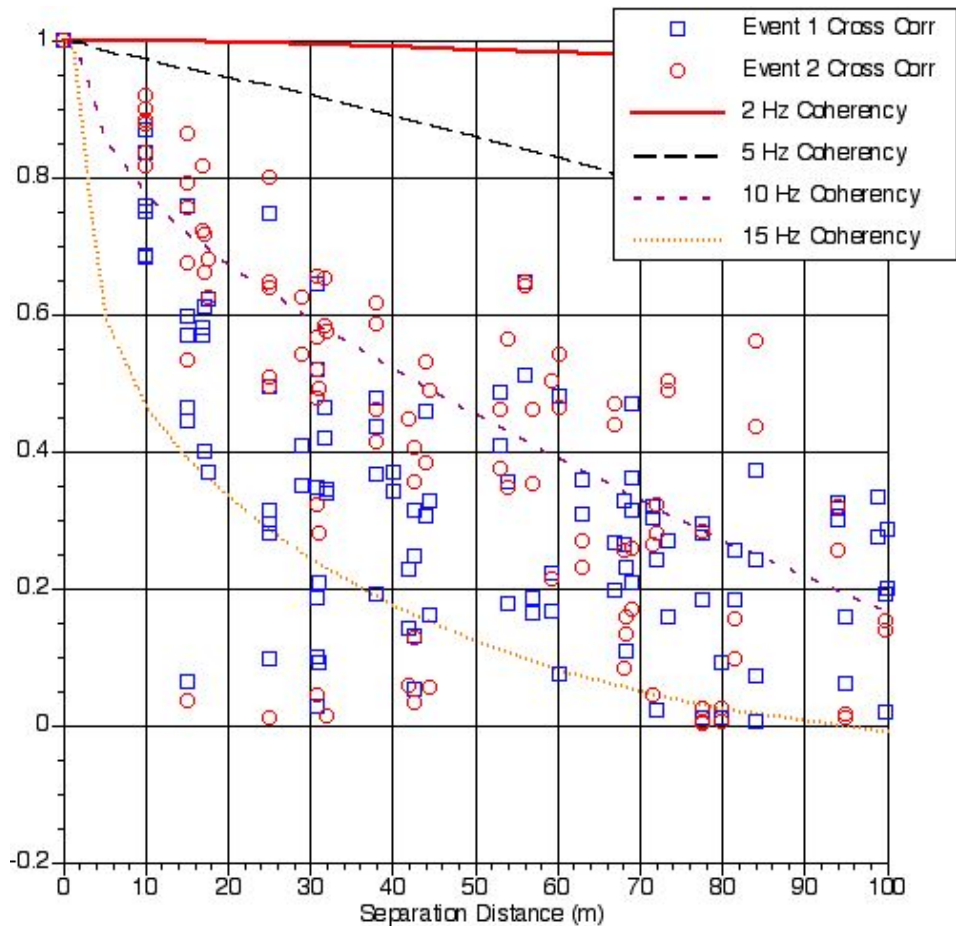
Figure 4-1
Example Comparison of Coherency and Cross-Correlation

Coherency and Phase Angles

Another way to get insight in to the coherency is to look at the coherency in the frequency domain. As an example, consider a case in which the amplitudes are all identical (here unity) and the phase differences are normally distributed. Figure 4-2 shows 30 random samples of the complex cross-spectral values for a mean phase difference of 30 degrees and a standard deviation of the phase difference of 20 degrees. The mean cross-spectrum is shown by the black X. The lagged coherency is given by the modulus of the mean cross-spectrum (distance from the origin). In this case, the lagged coherency is 0.94. The unlagged coherency is given by the real part of the mean cross-spectrum. In this case, the unlagged coherency is 0.81. As the mean phase difference approaches zero (e.g. not systematic time delays across the array), then the unlagged coherency becomes equal to the lagged coherency.

Figure 4-3 shows another example of the coherency in the complex plane. In this case, the standard deviation of the phase difference is 90 degrees. For this larger standard deviation of the phase differences, the lagged coherency is reduced to 0.31. The unlagged coherency is 0.23.
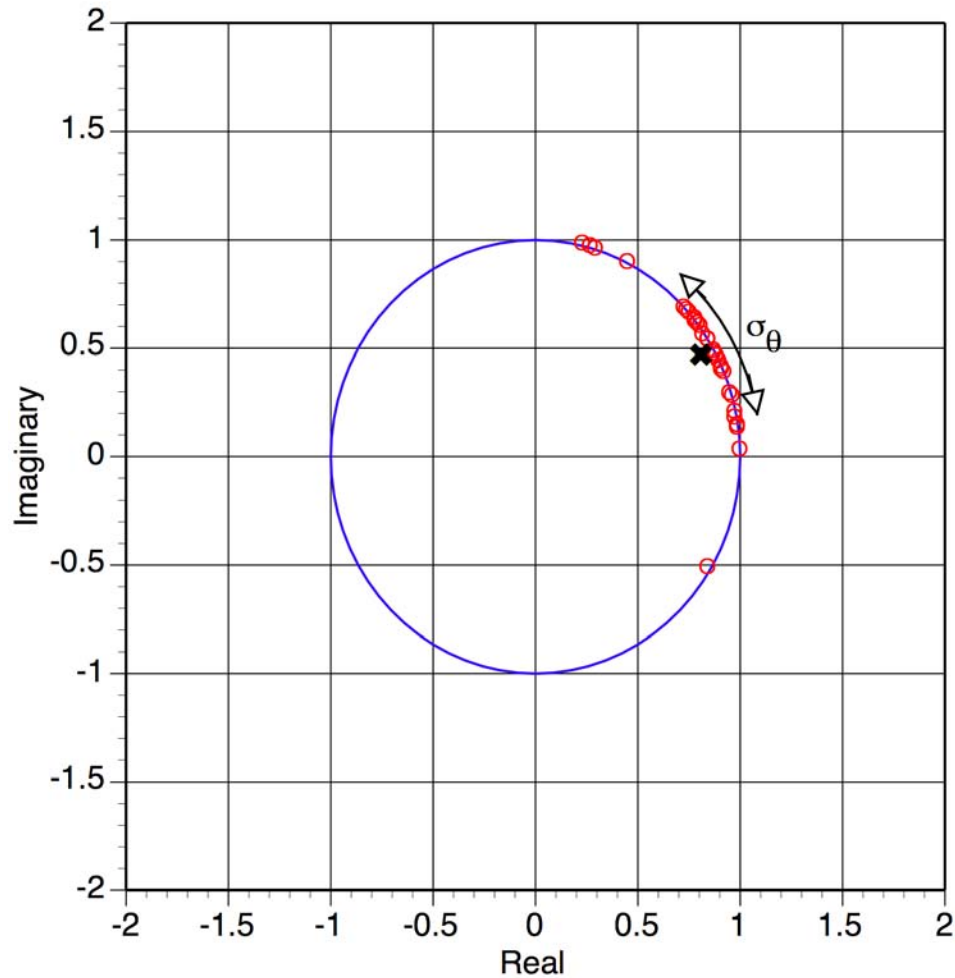
Figure 4-2
Example of the Variability of the Phase Angles and Coherency. For this Example, there is No Difference in the Amplitudes, the Mean Phase Difference is 30 Degrees, and the Standard Deviation of the Phase Difference is 20 Degrees. The Red Circles Show 30 Samples of the Cross-Spectrum. The x Shows the Mean Cross-Spectrum. The Lagged Coherency is 0.94

Repeating this exercise for a range of phase difference standard deviations, we can find the relation relation between the mean lagged coherency and the standard deviation of the phase differences. This relation is shown in Figure 4-4. For example, a coherency of 0.5 corresponds to a standard deviation of 68 degrees. For vertical plane wave propagation, this applies to the unlagged coherency as well.
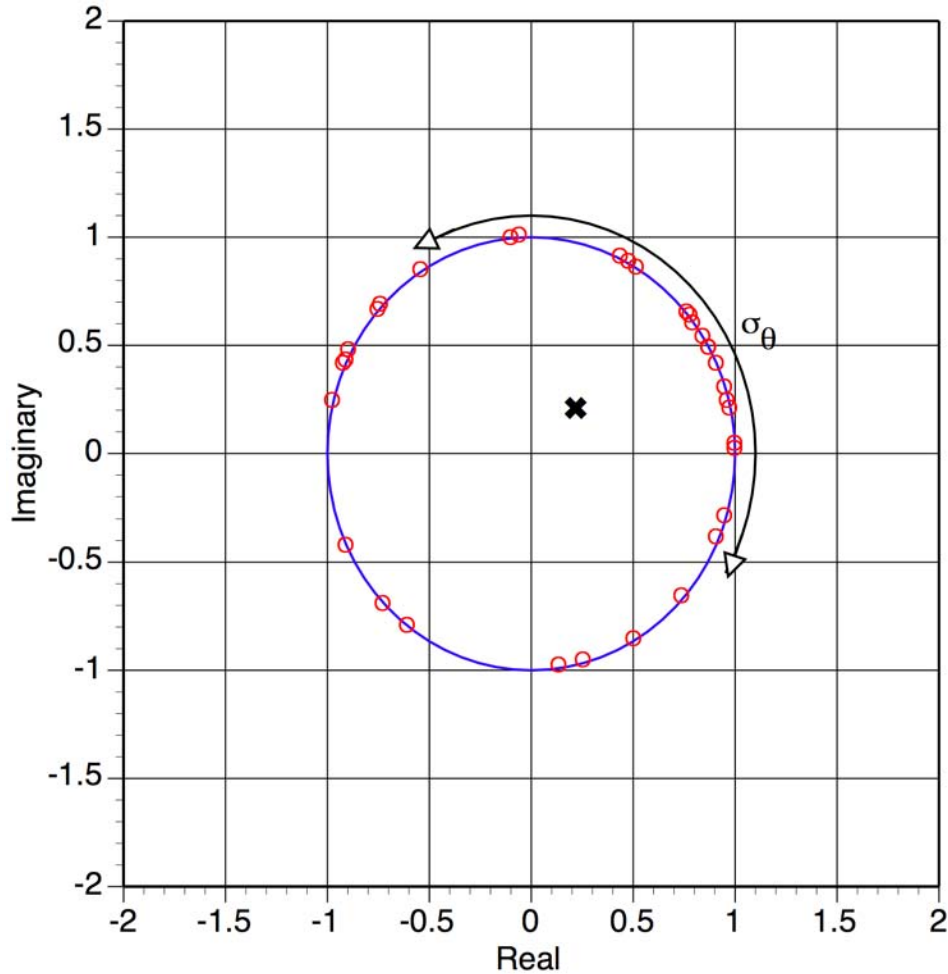
Figure 4-3
Example of the Variability of the Phase Angles and Coherency. For this Example, there is No Difference in the Amplitudes, the Mean Phase Difference is 30 Degrees, and the Standard Deviation of the Phase Difference is 90 Degrees. The Red Circles Show 30 Samples of the Cross-Spectrum. The x Shows the Mean Cross-Spectrum. The Lagged Coherency is 0.31

The actual cross-spectra will include variations in the amplitudes as well as phase differences. As described in Section 2, the cross-spectrum is smoothed over 11 frequencies. Examples of the complex cross-spectra for the Imperial Valley differential array is shown in First, consider a short station separation of 18 m. Figures 4-5 and 4-6 show the cross-spectra centered on 2 Hz and 15 Hz, respectively. For the 2 Hz case, the phase differences are all nearly the same and are centered near 0 since the wave passage effect is negligible for such a short station separation and low frequency. The lagged coherency is 1 and the unlagged coherency (real part) is also 1.0. For the 15 Hz case, the phase difference remain consistent, but there is larger variability as compared to 2 Hz. The lagged coherency is 0;85 and the unlagged coherency is 0.84.
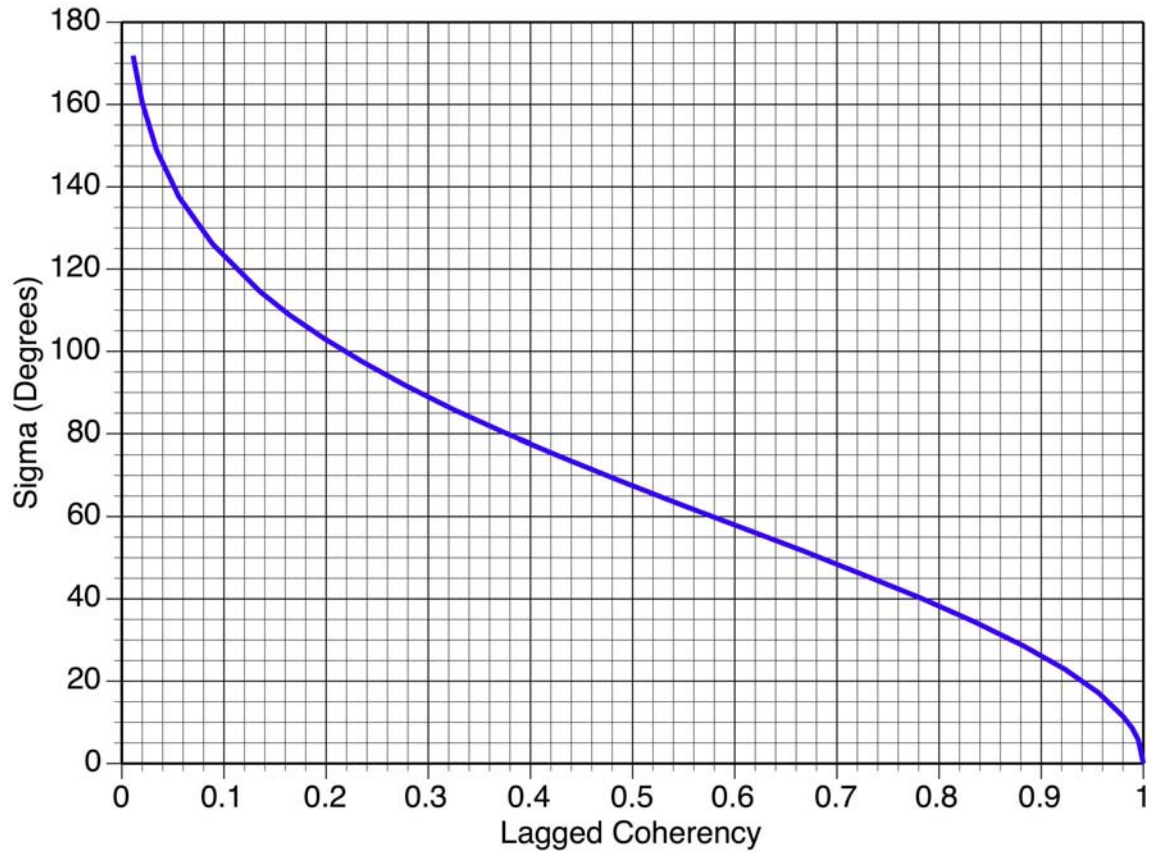
Figure 4-4
Relation Between the Coherency and the Standard Deviation of the Phase Angles for the Cases With a Constant Fourier Amplitude Over the Selected Frequency Band
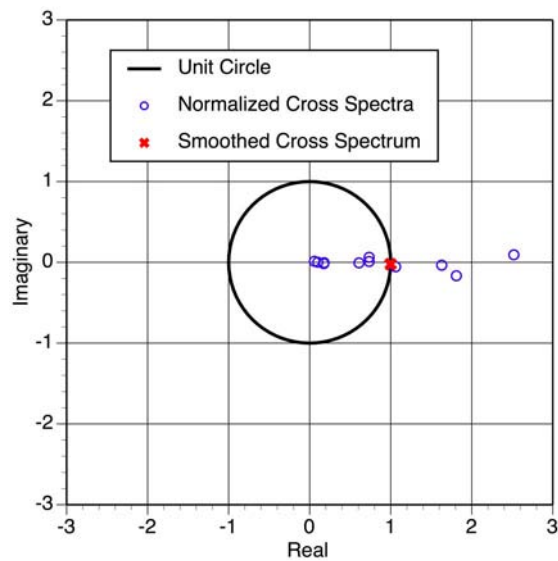
Figure 4-5
Example of the Estimation of Coherency for a Separation Distance of 18 m and a Center Frequency of 2 hz. Here, the Coherency is 1.00
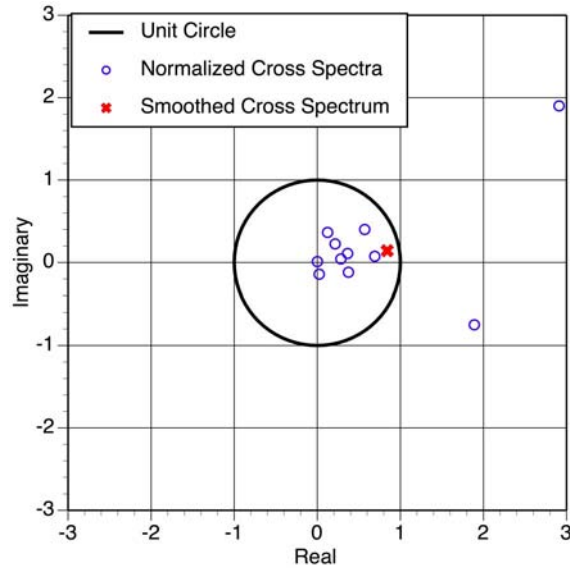
Figure 4-6
Example of the Estimation of Coherency for a Separation Distance of 18 m and a Center Frequency of 15 hz. Here, the Lagged Coherency is 0.85 and the Unlagged Coherency is 0.84

Note that the computation of the mean cross-spectrum gives greater weight to the phase differences associated with the larger amplitudes. This can be seen in Figure 4-6 in which the large amplitude (about 3 times the average) has the strongest effect on the mean cross-spectrum. An alternative would be to pre-whiten the data so that the amplitudes are constant, but the larger amplitudes are more important for the strong motion so I prefer to compute the mean including the amplitude variations.

Next, I used a large station separation of 128 m. The cross-spectra are shown in Figures 4-7 and 4-8 for 2 Hz and 15 Hz respectively. For the larger station separation, the wave passage effect can be seen as a non-zero average phase difference for 2 Hz (Figure 4-7). The phase differences are consistent and the lagged coherency is 0.99 and the unlagged coherency is 0.92. For the 15 Hz case (Figure 4-8), the cross-spectral values have much more variability, but are far from being completely random. For 15 Hz, the lagged coherency is 0.63 and the unlagged coherency is –0.47. A negative unlagged coherency means that the ground motions are out of phase at the two stations for this frequency band.
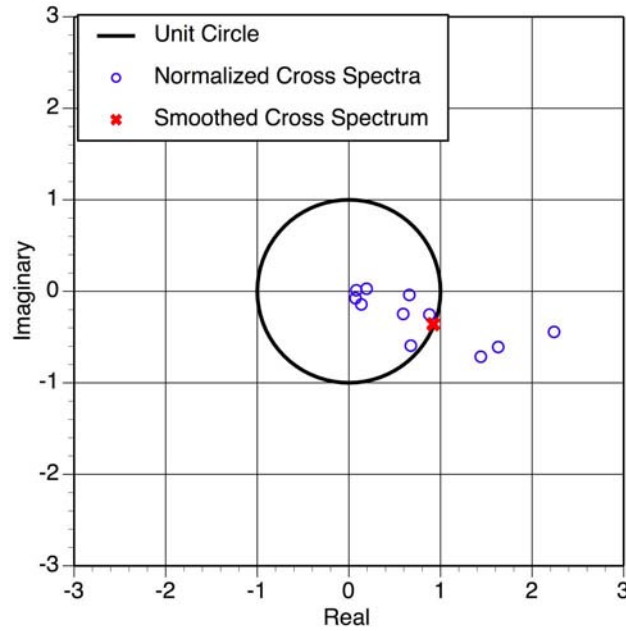
Figure 4-7
Example of the Estimation of Coherency for a Separation Distance of 128 m and a Center Frequency of 2 hz. Here, the Lagged Coherency is 0.99 and the Unlagged Coherency is 0.92
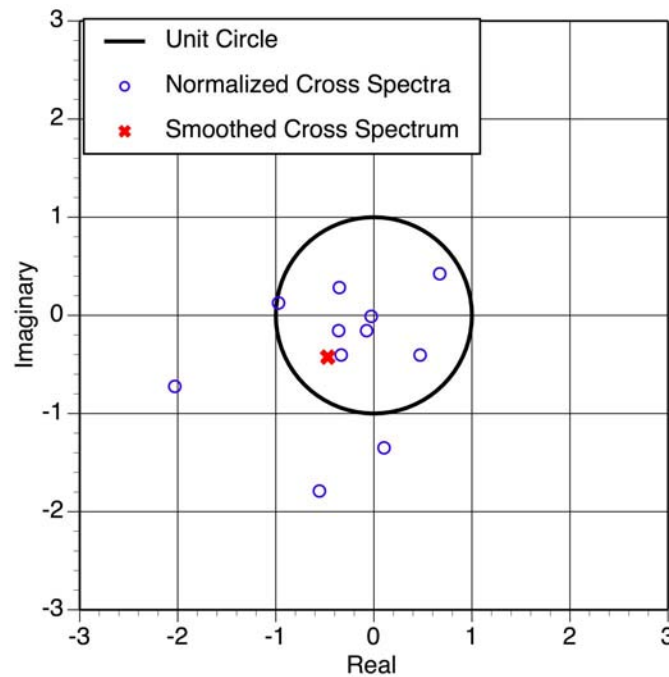
Figure 4-8
Example of the Estimation of Coherency for a Separation Distance of 128 m and a Center Frequency of 15 hz. Here, the Lagged Coherency is 0.63 and the Unlagged Coherency is -0.47

Causes of Incoherency

Spatial incoherency is caused by complex wave propagation. This could be a result of deviations from 1-D plane layered velocity models or from scattering. Most studies of spatial coherency have analyzed array data with stations spacing greater than 100 m. For nuclear power plants, our focus is on station separations less than 100 m with an emphasis on separations of 5-20 m. What is depth range of velocity structure variability that is the cause of the high frequency (f> 10 Hz) spatial incoherency over such short distances? Ideally, we could have numerical models of the velocity structure variability that could explain the observed coherency and identify the depth range responsible, however, to date, I am not aware of any studies that have successfully developed physical models of the velocity structure variability that can explain the observed coherency over very short separation distances (< 20 m).

One dense array that has been well studied is the Pinyon Flat array (see Section 3). The large spatial variability of the ground motions over short distances has been a surprise for some seismologists. For example, Bear et al (1999) found that the Pinyon Flat data showed larger than expected deviations from simple plane-wave propagation over short distances. They suggested that this could be due to weathering of the shallow material, large scale anisotrphy, and near surface scattering. Vernon et al (1998) attributed the spatial incoherency to scattering. In my opinion, the near surface scattering is the likely cause, not extremely large anisotropy. The question is, what is the depth range of "near-surface" scattering? Bear et al found that the deviations from simple plane wave propagation seen at depths of 153 ad 274 m in the borehole is similar to the deviations seen at the surface. This indicates that the shallow weathering is not the main cause of the incoherency: it must be coming from depths greater than a few hundred meters.

While there is still insufficient data available, in my opinion, the incoherency observed over distances of 10s of meters is caused by scattering in the top 500 m. Additional data and analysis of numerical simulations will be needed to confirm this.

Impact of Non-Linear Site Response

The coherency changes the phasing of the ground motion at a point, but not the Fourier amplitude. With the same amplitudes, the strain dependent properties should be similar. Therefore, no change is needed in the approach to non-linear site response.

Correlation of FAS and Coherency

The main issue here is a possible correlation of coherency with the FAS. The EUS rock sites will have larger high frequency content, so if there is a positive correlation between coherency and FAS, then we would expect to have higher coherency in the EUS.

To address this, we have plotted the lagged coherency and the FAS for the EPRI Parkfield and the Pinyon Flat arrays in Figures 4-9 and 4-10. The spectra for these two arrays peak in the 8 - 14 Hz range, but the coherency does not peak at the peak amplitude in the spectrum. The Pinyon Flat array does have higher coherency at high frequencies than predicted by the model, but the EPRI Parkfield array does not show the same trend.
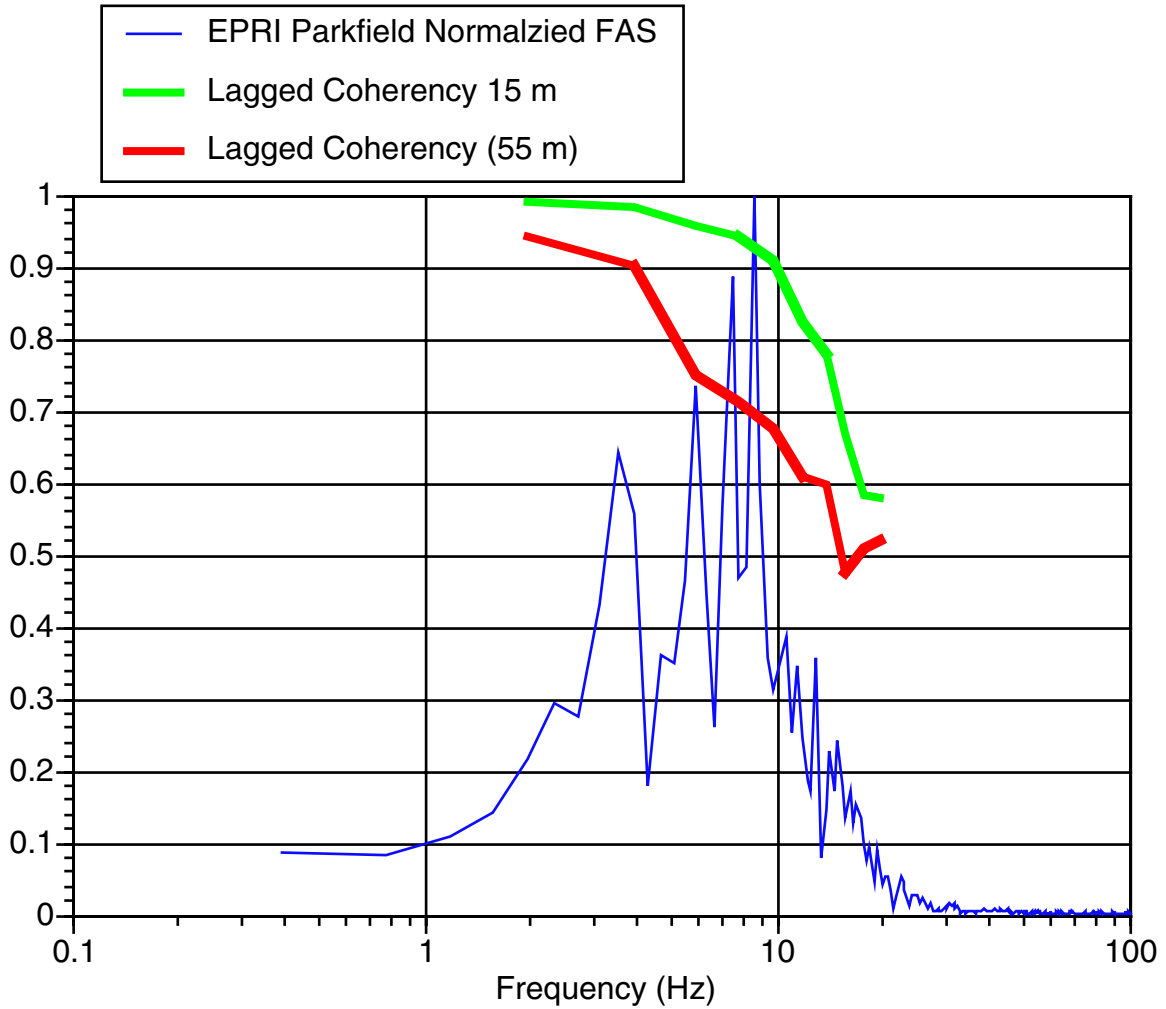
Figure 4-9
Comparison of the FAS and the Lagged Coherency for the EPRI Parkfield Array
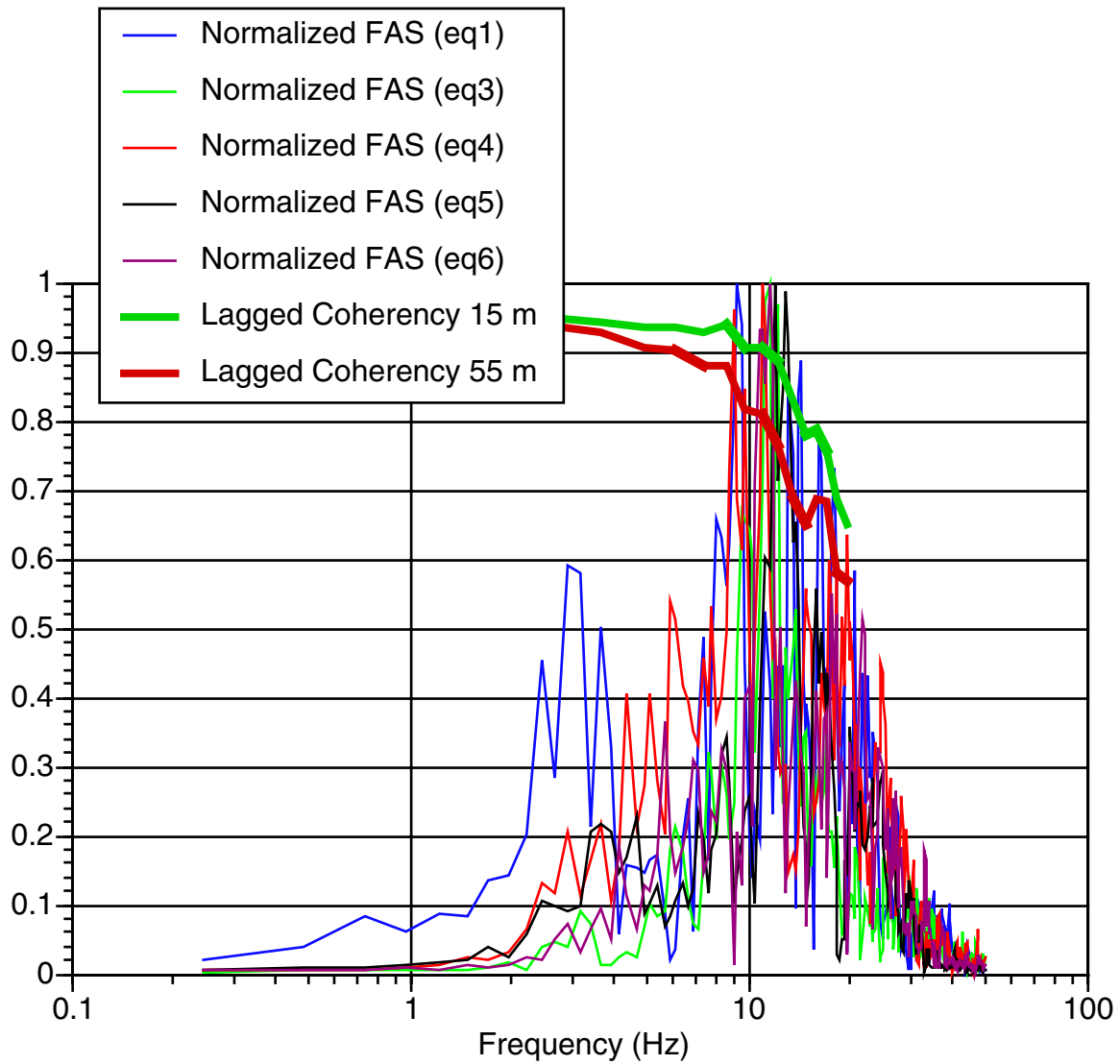
Figure 4-10
Comparison of the FAS and the Lagged Coherency for the Pinyon Flat Array

5
COMPUTED COHERENCIES

This section describes the selection of the time windows and the identification of useable frequency bands for computing the coherency from the dense array data. The dependence of the coherency on source parameters (magnitude and distance) and on the site condition (soil, soft-rock, hard-rock) is evaluated.

Selection of Time Windows

For all of the data expect the Pinyon Flat data, the time windows were selected by visual inspection of the acceleration time histories. The time windows were selected to capture the strongest high frequency shaking on the horizontal components. The selected time windows for each earthquake are listed in Table 5-1. Examples of the time windows for each array are shown in Appendix A.

Time Windows for Pinyon Flat

Due to the large number of earthquakes for the Pinyon Flat array, an automated method was developed to select the time window based on the duration of the normalized Arias intensity of the two horizontal components of velocity. The approach for selecting the Pinyon Flat time windows is described below.

The Pinyon Flat recordings can have long pre-event and post-event memory. Even though the ground motion is much lower in these sections of the records, if they are very long, they can have a significant effect on the normalized Arias intensity. Therefore, an initial data window was applied that starts 10 seconds before the peak velocity and ends 10 seconds after the peak velocity. (The peak velocity is defined as the largest velocity on either of the two horizontal components).

The normalized Arias intensity is then given by:

$$I(\tau) = \frac{\int\limits_{T_P-10}^{\tau} V_1^2(t) + V_2^2(t)\, dt}{\int\limits_{T_P-10}^{T_P+10} V_1^2(t) + V_2^2(t)\, dt} \qquad \textbf{Equation 5-1}$$

where T_P is the time of the peak velocity. A window based on the time at which the normalized Arias intensity reaches a value of 0.10 and 0.75. These times are denoted $T_{0.1}$ and $T_{0.75}$. To avoid a very short duration, the start time of the window is set 0.5 seconds before $T_{0.1}$ and 1.0 seconds after $T_{0.75}$. An example of the initial windowing is shown in Figure 5-1. The final window is based on the normalized Arias intensity. Examples of the final windows are shown in Figures 5-2 and 5-3 for short and long duration records, respectively.

Table 5-1
Time Window Used in the Coherency Estimates from Dense Arrays

Array	Event Number	Event Name	Start Time (sec)	Window Duration (sec)
EPRI LSST	2	eq02	4.5	2.0
EPRI LSST	3	eq03	1.0	5.0
EPRI LSST	4	eq04	3.5	5.0
EPRI LSST	5	eq05	3.0	2.5
EPRI LSST	6	eq06	5.0	5.0
EPRI LSST	7	eq07	9.0	5.0
EPRI LSST	8	eq08	1.0	5.0
EPRI LSST	10	eq10	2.0	2.5
EPRI LSST	11	eq11	2.8	2.5
EPRI LSST	12	eq12	5.0	5.0
EPRI LSST	14	eq14	5.0	2.5
EPRI LSST	16	eq16	18.0	10.0
EPRI LSST	17	eq17	13.0	10.0
EPRI PARKFIELD	1	EV1	2.5	2.0
EPRI PARKFIELD	2	EV2	4.0	2.5
CHIBA	1	Eq8307	5.1	2.5
CHIBA	2	Eq8420	10.0	5.0
CHIBA	3	Eq8510	9.0	5.0
CHIBA	4	Eq8519	11.0	5.0
CHIBA	5	Eq8525	7.8	4.5
CHIBA	6	Eq8722	8.4	5.0
CHIBA	7	Eq8806	6.8	4.5
CHIBA	8	Eq8816	12.0	5.0
CHIBA	9	Eq8901	10.0	5.0
IV Diff	1	Event A	3.9	2.5
IV Diff	2	Event B	5.0	2.5
Hollister Diff	1	88Feb20	5.0	5.0
Coalinga	2	eq02	3.1	2.0
Coalinga	3	eq03	2.4	2.0
Coalinga	5	eq05	2.9	2.0
Coalinga	7	eq07	2.9	2.0

Table 5-1
Time Window Used in the Coherency Estimates from Dense Arrays (Continued)

Array	Event Number	Event Name	Start Time	Window Duration (sec)
Pinyon Flat	1	90.108/90.108.01.16.51	13:36:00.846	1.764
Pinyon Flat	2	90.108/90.108.10.23.27	07:58:58.746	7.540
Pinyon Flat	3	90.108/90.108.14.25.58	05:06:14.818	7.628
Pinyon Flat	4	90.108/90.108.14.32.41	11:56:27.469	6.716
Pinyon Flat	5	90.108/90.108.19.07.21	11:30:15.057	8.024
Pinyon Flat	6	90.109/90.109.05.43.34	08:54:21.877	8.120
Pinyon Flat	7	90.109/90.109.08.42.55	08:25:18.353	2.120
Pinyon Flat	8	90.109/90.109.20.24.52	14:32:24.349	7.320
Pinyon Flat	9	90.110/90.110.02.24.45	14:26:17.505	1.816
Pinyon Flat	10	90.110/90.110.03.24.54	12:33:59.529	5.324
Pinyon Flat	11	90.110/90.110.07.21.01	07:15:52.521	5.552
Pinyon Flat	12	90.110/90.110.17.48.02	13:36:37.817	7.548
Pinyon Flat	13	90.111/90.111.17.29.03	13:29:46.001	7.472
Pinyon Flat	26	90.115/90.115.03.29.27	19:02:40.329	1.728
Pinyon Flat	29	90.115/90.115.07.08.28	21:48:44.069	2.980
Pinyon Flat	30	90.115/90.115.07.10.58	14:23:46.857	7.264
Pinyon Flat	32	90.115/90.115.09.46.24	10:15:21.149	1.808
Pinyon Flat	33	90.115/90.115.09.53.30	03:54:20.505	7.324
Pinyon Flat	39	90.115/90.115.16.26.39	13:32:12.040	1.744
Pinyon Flat	44	90.115/90.115.22.36.37	03:08:12.520	3.904
Pinyon Flat	61	90.117/90.117.13.51.16	12:15:03.040	12.208
Pinyon Flat	63	90.117/90.117.15.40.10	11:30:30.764	4.592
Pinyon Flat	65	90.117/90.117.20.03.12	00:22:54.168	6.844
Pinyon Flat	67	90.118/90.118.08.32.30	18:50:42.016	7.916
Pinyon Flat	68	90.118/90.118.10.12.04	18:44:36.160	2.104
Pinyon Flat	69	90.118/90.118.14.23.11	17:02:59.220	6.896
Pinyon Flat	71	90.118/90.118.15.21.32	06:28:56.476	6.524
Pinyon Flat	74	90.119/90.119.02.56.08	23:16:27.188	2.128
Pinyon Flat	76	90.119/90.119.11.25.57	17:04:19.980	1.892
Pinyon Flat	80	90.119/90.119.19.35.48	21:42:06.416	8.176
Pinyon Flat	84	90.120/90.120.06.01.41	13:46:54.624	1.800
Pinyon Flat	85	90.120/90.120.06.56.22	07:42:46.368	1.760
Pinyon Flat	86	90.120/90.120.07.30.46	07:16:10.076	4.960
Pinyon Flat	88	90.120/90.120.20.16.54	02:29:07.328	4.568
Pinyon Flat	100	90.122/90.122.14.13.10	16:19:58.200	3.864
Pinyon Flat	125	90.127/90.127.07.58.05	01:36:52.728	1.944
Pinyon Flat	126	90.127/90.127.12.41.00	00:57:47.536	7.344
Pinyon Flat	128	90.127/90.127.21.01.53	22:13:29.828	5.328

Table 5-1
Time Window Used in the Coherency Estimates from Dense Arrays (Continued)

| Array	Event Number	Event Name	Start Time	Window Duration (sec)
Pinyon Flat	131	90.128/90.128.10.18.33	18:04:24.428	2.448
Pinyon Flat	136	90.129/90.129.22.05.28	15:19:17.216	1.760
Pinyon Flat	141	90.130/90.130.07.23.31	14:20:51.464	5.580
Pinyon Flat	143	90.130/90.130.10.42.12	13:25:21.260	2.292
Pinyon Flat	144	90.130/90.130.12.10.41	12:10:53.220	1.764
Pinyon Flat	146	90.130/90.130.14.16.02	08:39:47.348	1.964
Pinyon Flat	148	90.130/90.130.14.25.08	01:41:19.900	7.884
Pinyon Flat	152	90.130/90.130.15.19.06	22:05:38.800	1.912
Pinyon Flat	154	90.130/90.130.15.57.44	00:22:31.556	1.920
Pinyon Flat	156	90.130/90.130.17.29.42	15:00:28.800	1.764
Pinyon Flat	161	90.131/90.131.00.54.55	19:01:38.964	1.760
Pinyon Flat	162	90.131/90.131.00.57.36	12:41:09.088	1.780
Pinyon Flat	175	90.132/90.132.15.16.58	17:27:56.960	1.736
Pinyon Flat	180	90.132/90.132.19.42.46	15:03:09.076	1.876
Pinyon Flat	184	90.132/90.132.23.54.47	06:59:49.488	9.356
Pinyon Flat	190	90.134/90.134.05.05.20	13:05:48.591	2.372
Pinyon Flat	192	90.134/90.134.07.29.45	16:24:46.929	1.748
Pinyon Flat	195	90.134/90.134.11.32.06	09:09:43.625	1.764
Pinyon Flat	196	90.134/90.134.11.34.45	08:59:31.797	1.752
Pinyon Flat	199	90.135/90.135.00.10.14	22:39:26.253	4.176
Pinyon Flat	200	90.135/90.135.02.28.56	20:17:13.761	4.560
Pinyon Flat	204	90.135/90.135.13.46.43	06:01:55.517	1.808
Pinyon Flat	209	90.136/90.136.01.14.15	17:55:40.724	1.960
Pinyon Flat	211	90.136/90.136.04.53.05	16:22:39.344	1.728
Pinyon Flat	213	90.136/90.136.18.14.38	05:26:17.256	1.816
Pinyon Flat	215	90.137/90.137.02.36.37	02:50:47.334	4.140
Pinyon Flat	226	90.138/90.138.12.05.42	14:38:34.008	2.908
Pinyon Flat	234	90.139/90.139.06.30.57	05:06:10.174	5.608
Pinyon Flat	236	90.139/90.139.09.48.19	20:28:51.926	2.868
Pinyon Flat	237	90.139/90.139.11.36.56	18:57:41.302	3.856
Pinyon Flat	243	90.140/90.140.01.15.48	01:29:58.762	1.760
Pinyon Flat	245	90.140/90.140.04.54.23	22:23:35.878	3.644
Pinyon Flat	250	90.141/90.141.14.14.09	15:22:12.014	1.776
Pinyon Flat	251	90.142/90.142.00.02.28	14:37:44.450	1.900
Pinyon Flat	252	90.142/90.142.03.22.47	14:29:19.454	1.832
Pinyon Flat	260	90.144/90.144.00.05.41	04:43:19.550	1.816
Pinyon Flat	270	90.145/90.145.03.59.16	23:53:18.494	2.332
Pinyon Flat	271	90.145/90.145.04.15.25	17:38:12.841	1.740
Pinyon Flat	274	90.145/90.145.12.35.53	17:32:01.181	6.428
Pinyon Flat	283	90.147/90.147.11.30.05	19:07:33.617	1.784
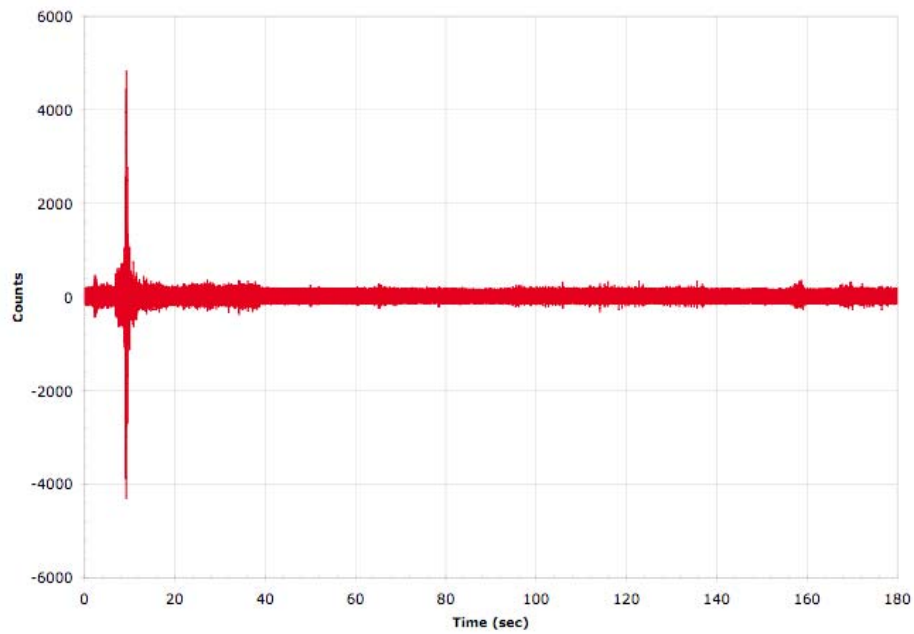
Figure 5-1
Example of the Long Post-Event Memory from a Recording from the Pinyon Flat Array (Event 90.108.01.16.51). The Peak Velocity is at 9.2 sec. an Initial Window from 0 to 19.2 Sec is Selected

Figure 5-2
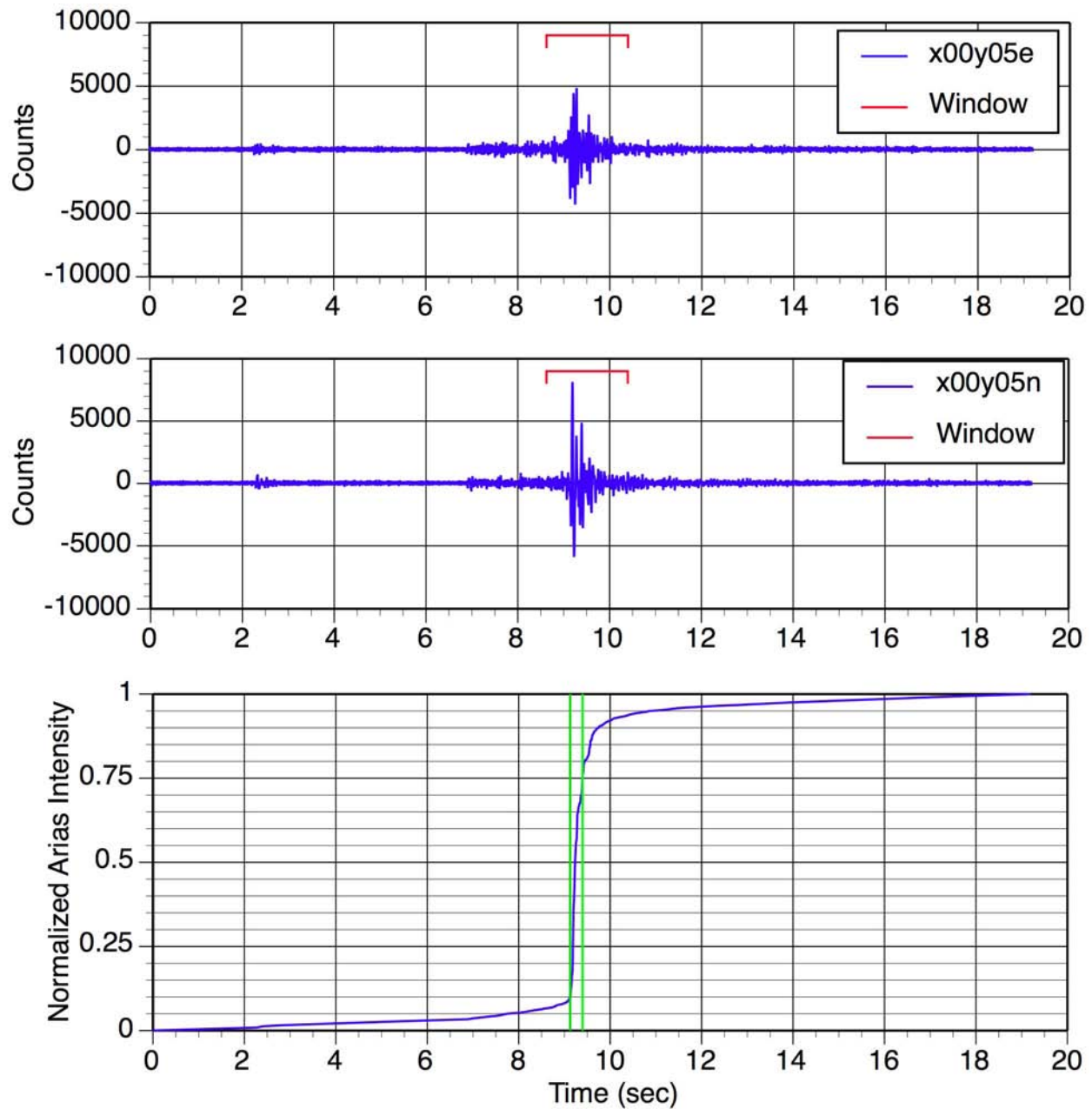**Example of the Final Window Selected from the 20 Seconds About the Peak Velocity for a Short Duration Recording**
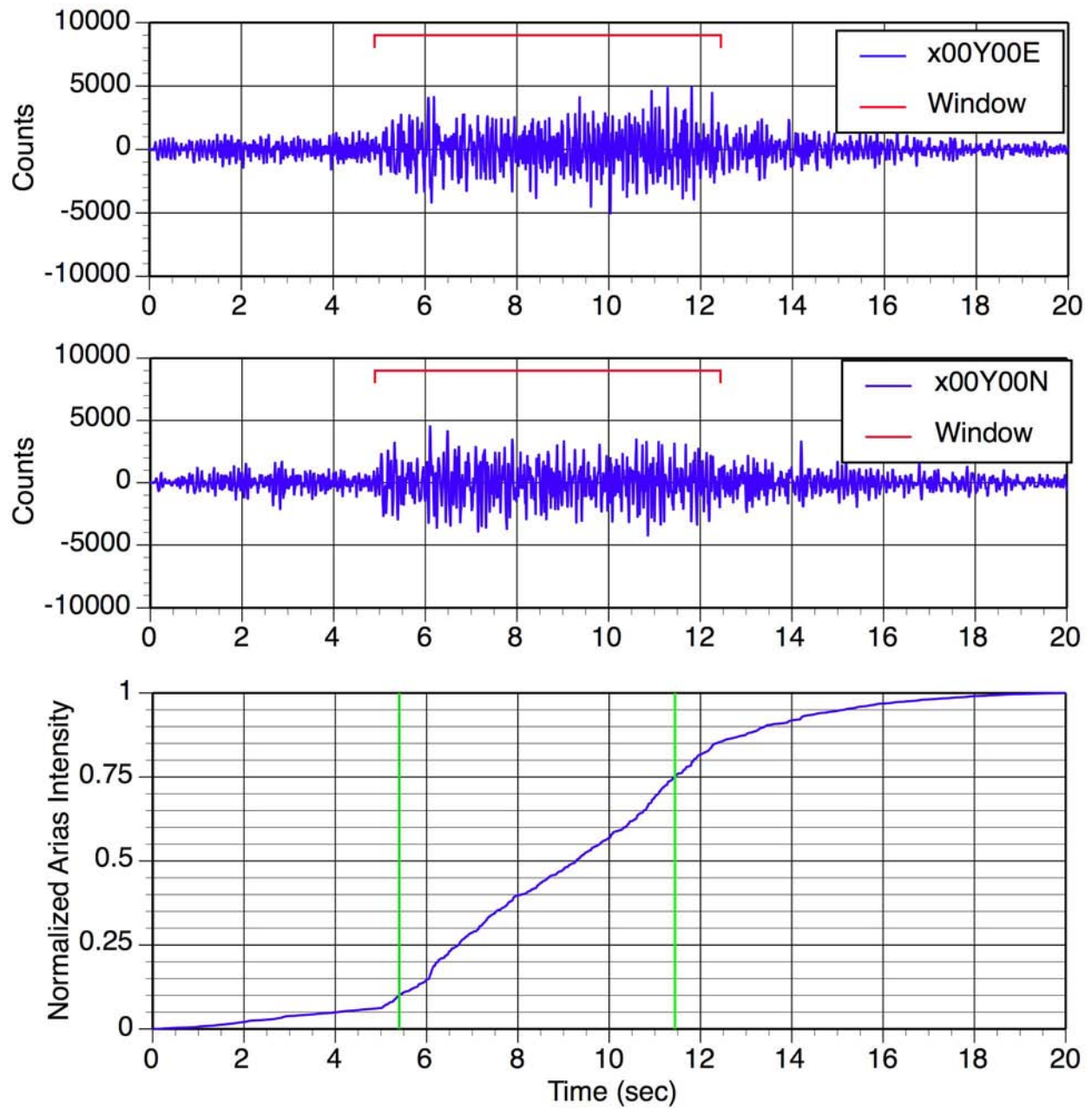
Figure 5-3
Example of the Final Window Selected from the 20 Seconds About the Peak Velocity for a Long Duration Recording

Scaling With Frequency and Separation Distance

Early studies of coherency based on very simple physical models assumed that the key parameter was the number of wave lengths separating the two stations. That is, doubling the frequency would have the same effect on the coherency as doubling the separation distance. If this is the case, then we don't need very dense arrays because we can use stations at larger separations and lower frequencies in place of short separations at high frequencies. Unfortunately, Abrahamson (1992) showed that the coherency scaled differently with frequency and separation distance so these simple physical models don't work. Therefore, I have developed purely empirical models of the coherency. The downside of an empirical approach is that you need to have enough data to constrain the model for all cases (all separation distances and frequencies).

Vernon et al (1991) also found that they could not predict the observed coherency using physical models. The models significantly over-predict the coherency for separations distances less than 500 m.

The main parameters that control the coherency are the separation distance and frequency. In addition, the topography has been found to have a significant effect on the coherency. The main assumption made in using the model is that the ground motion is stationary over the window of strong staking.

Initial Coherency Model

The functional form for the coherency model is based on the empirical data. It does not have a physical basis other than the coherency must go to unity at zero separation distance and zero frequency and the coherency must go to zero at very large frequencies and very large separation distances.

The frequency dependence of the coherency is stronger than the separation distance dependence. From exploratory analysis of the plane-wave coherency, the frequency dependence at a given separation distance was first modeled by the product of two low-pass filters. The separation distance dependence of the corner frequency of the filters, f_c, and the number of poles, n_1 and n_2, was then modeled. The resulting functional form is given by Equation 5-2. The $Tanh(a_3\xi)$ term is included in the numerator to force the coherency to unity at all frequencies for zero separation distance.

$$\gamma_{pw}(f,\xi) = \left[1 + \left(\frac{f\ Tanh(a_3\xi)}{a_1 f_c(\xi)}\right)^{n1}\right]^{-\frac{1}{2}} \left[1 + \left(\frac{f\ Tanh(a_3\xi)}{a_2 f_c(\xi)}\right)^{n2(\xi)}\right]^{-\frac{1}{2}}$$

Equation 5-2

The resulting coefficients are listed in Tables 5-2 and 5-3 for the horizontal and vertical components, respectively. The coherency model for the horizontal and vertical components are shown in Figure 5-4.

Table 5-2
Plane-Wave Coherency Model Coefficients for the Horizontal Component

Coeff	Horizontal Component
a_1	1.647
a_2	1.01
a_3	0.4
n_1	7.02
$n_2(\xi)$	5.1 - 0.51 ln(ξ+10)
$f_c(\xi)$	$f_c(\xi) = -1.886 + 2.221 \ln\left(\dfrac{4000}{\xi+1} + 1.5\right)$
s	0.0005 s/m to 0.00025 s/m

Table 5-3
Plane-Wave Coherency Model Coefficients for the Vertical Component

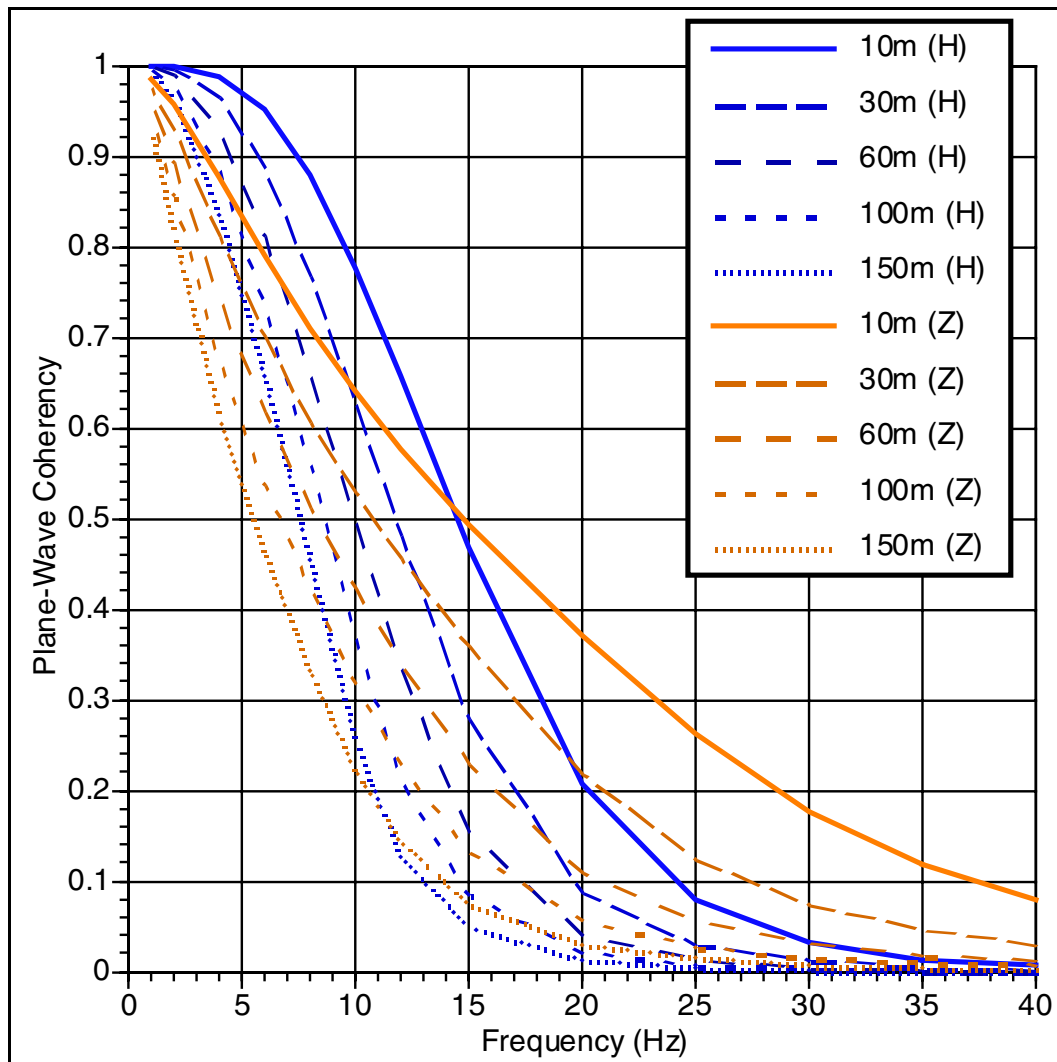| Coeff	Vertical Component
a_1	3.15
a_2	1.0
a_3	0.4
n_1	4.95
$n_2(\xi)$	1.685
$f_c(\xi)$	$f_c(\xi) = \exp\left(2.43 - 0.025\ln(\xi+1) - 0.048[\ln(\xi+1)]^2\right)$
s	0.0005 s/m to 0.00025 s/m

Figure 5-4
Horizontal and Vertical Component Plane-Wave Coherency Models from the Initial Model

Source Parameter Dependence

Previous studies have suggested that coherency depends on earthquake source parameters, but these studies have been based on just a few earthquakes. When larger data sets are used, these trends do not remain. Vernon et al (1991) reached this same conclusion. They found that the correlations with event parameters vanish when averaged over a large number of events.

Magnitude Dependence

For a point source, the earthquake magnitude should not affect the coherency if the scattering is linear. For large magnitudes at short distance, there could be a reduction in coherency due to different wave paths from different parts of the rupture leading to deviations from single plane-wave propagation.

The magnitude dependence is examined using the data from a single array so that there are no site effects differences. The LSST array has the best range of magnitudes. An example of the magnitude dependence of the LSST residuals for separation distance of 20-30 m is shown in Figure 5-5. As expected, there is no trend in the residuals with magnitude.
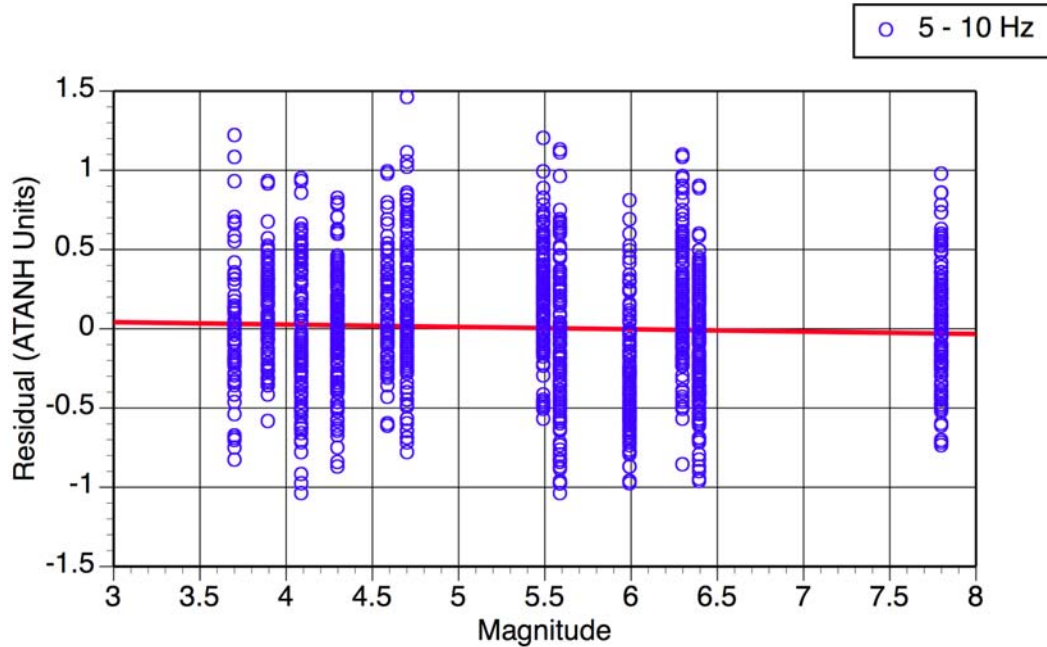

Figure 5-5
Example of the Magnitude Dependence of the Coherency Residuals from the LSST Array for Separation Distances In the Range of 20-30m

Distance Dependence

For a point source, distance should not affect the coherency if the scattering is linear. For large magnitudes at short distance, there could be a reduction in coherency due to different wave paths from different parts of the rupture leading to deviations from single plane-wave propagation.

The distance dependence is examined using the data from a single array so that there are no site effects differences. An examples of the distance dependence of the LSST residuals for separation distance of 20-30 m is shown in Figure 5-6. There is a slight trend of increasing residual with increasing distance for this case, but this trend is not seen systematically at other frequencies and other separation distances.
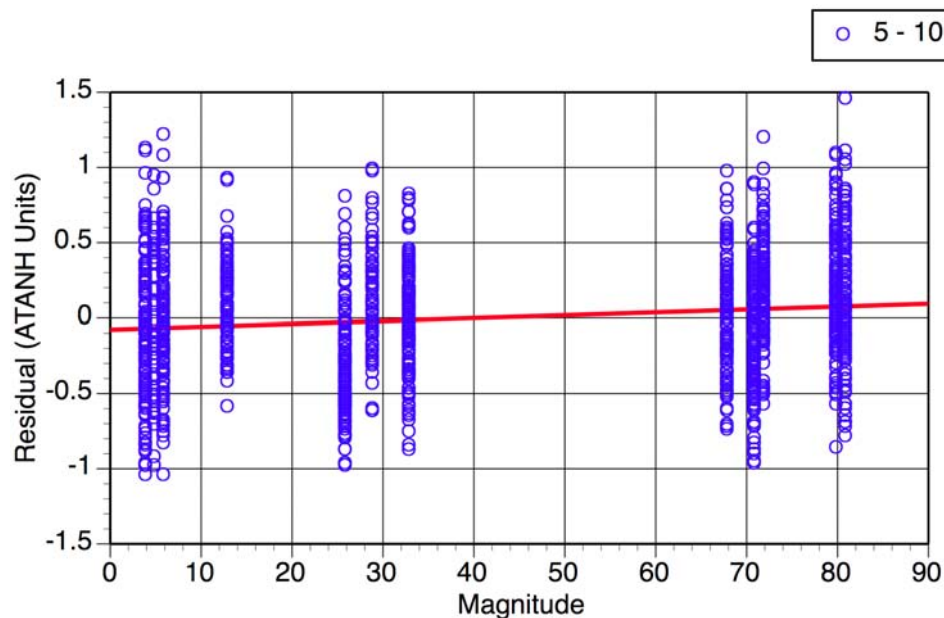
Figure 5-6
Example of the Distance Dependence of the Coherency Residuals from the LSST Array for Separation Distances in the Range of 20-30m

Other Source Parameter Dependence

Other source parameters, such as focal mechanism and focal depth were evaluated and no dependence was observed. The array data used do not have strong directivity effects, so the directivity dependence of coherency cannot be checked with this data set, but there is no reason to expect that directivity would affect the coherency. Directivity effects could significantly affect the amplitude of the low frequency ground motion, but not the variability of the phasing.

Site Condition Dependence

Just changing the 1-D velocity profile would change the amplitude and phasing of the ground motions, but it would not change the phase differences which control the coherency. If there is a change in the 2-D or 3-D velocity structure, then the phase differences could be changed and the coherency affected. The greater the lateral variability, the lower the coherency. If the amount of lateral variability in the velocity structure is correlated to the site condition, then site condition will have an effect on coherency.

The average coherency for soil sites, soft-rock sites, and hard-rock sites are shown in Figures 5-7 and 5-8 for separation distances of 15-30 m and 50-70m. The only hard-rock array is the Pinyon Flat array so the hard-rock curves are based only on the Pinyon Flat data. For the soft-rock curves, there are two arrays (EPRI Parkfield and Coalinga), but only the EPRI Parkfield array has station separations in the 15-30 m range. For the 15-30 m range, there is a clear dependence on the site condition with the coherency increasing for soft-rock and hard-rock sites. For the 50-70 m range, the soil and soft-rock sites are similar, but the hard-rock coherency is still much higher.
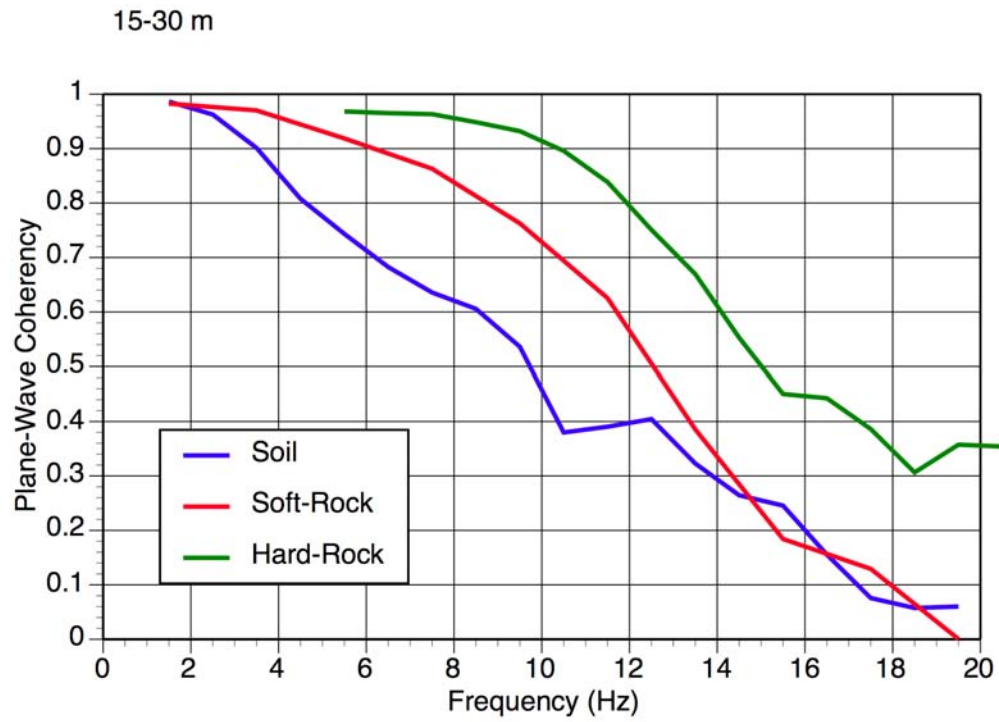
15-30 m

Figure 5-7
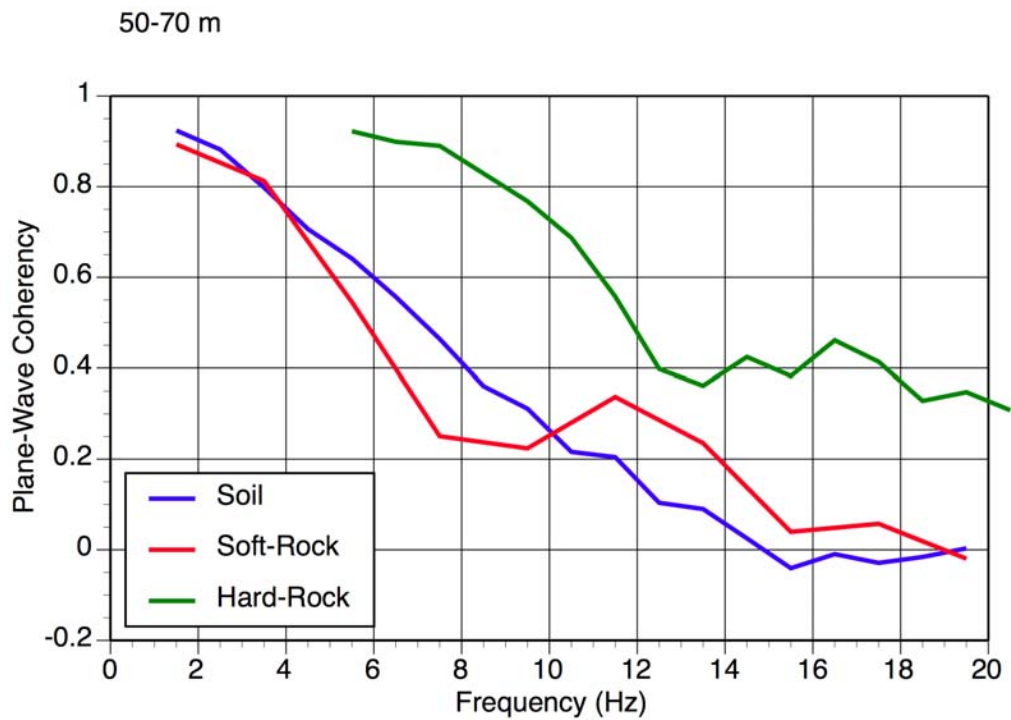**Site Dependence of Coherency for 15-30 M Separations**

50-70 m

Figure 5-8
Site Dependence of Coherency for 50-70 M Separation

The average coherency for embedded sites is compared to the coherency for hard-rock, soft-rock, and soil sites in Figures 5-9 and 5-10 for separation distances of 15-30 m and 50-70m, respectively. The coherency for embedded sites is similar to the hard-rock coherency.
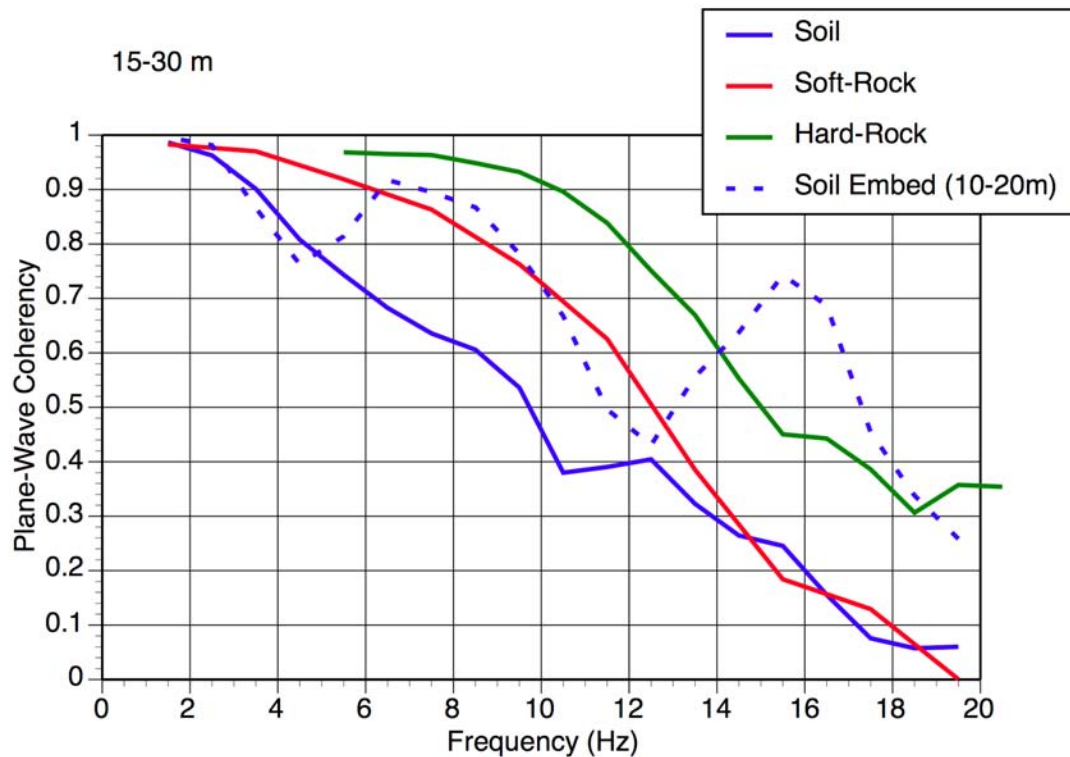

Figure 5-9
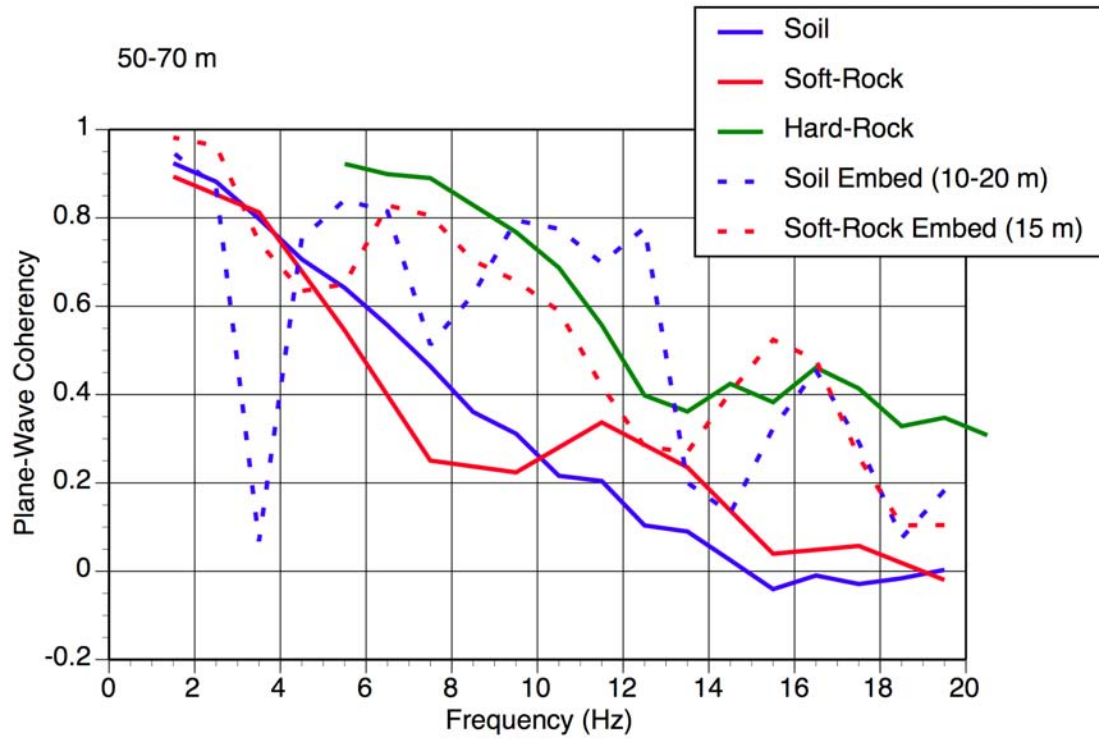**Comparison of the Soil Embedded Coherency With the Hard-Rock Coherency for 15-30 M**

Figure 5-10
Comparison of the Soil Embedded Coherency With the Hard-Rock Coherency for 50-70 M

6
HARD-ROCK COHERENCY MODEL

Based on the site dependence seen in Section 5, hard-rock coherency model is developed using only the Pinyon Flat array data. While there is a shallow layer of rock above the hard-rock at this site, the Pinyon Flat site is the best data set available for developing hard-rock coherency models.

Regression Analysis

The plane-wave coherency is modeled by the functional form described in Section 4:

$$\gamma_{pw}(f,\xi) = \left[1 + \left(\frac{f\ Tanh(a_3\xi)}{a_1 f_c(\xi)}\right)^{n1(\xi)}\right]^{-\frac{1}{2}} \left[1 + \left(\frac{f\ Tanh(a_3\xi)}{a_2}\right)^{n2}\right]^{-\frac{1}{2}}$$

Equation 6-1

The regression analysis was conducted using the $\tanh^{-1}(\gamma_{pw})$ because this transformation leads to residuals that are approximately normally distributed. The results are presented in terms of the untransformed coherency because it is easier to understand.

The coefficients were derived from using data from the 78 earthquakes listed in Table 6-1. Since most of the data were from small magnitude earthquakes with small amplitudes at the low frequencies, the computed coherencies are used only for freq > 5 Hz. The resulting model coefficients are given in Tables 6-1 and 6-2 for the horizontal and vertical components, respectively. The plane-wave coherency models for the horizontal and vertical components are shown in Figures 6-1 and 6-2, respectively.

Table 6-1
Plane-Wave Coherency Model Coefficients for the Horizontal Component

Coeff	Horiz Coeff
a_1	1.0
a_2	40
a_3	0.4
$n_1(\xi)$	$3.80-0.040*\ln(\xi+1)+0.0105[\ln((\xi+1)-3.6]^2$
n_2	16.4
$f_c(\xi)$	$27.9-4.82*\ln(\xi+1)+1.24[\ln((\xi+1)-3.6]^2$

Table 6-2
Plane-Wave Coherency Model Coefficients for the Vertical Component

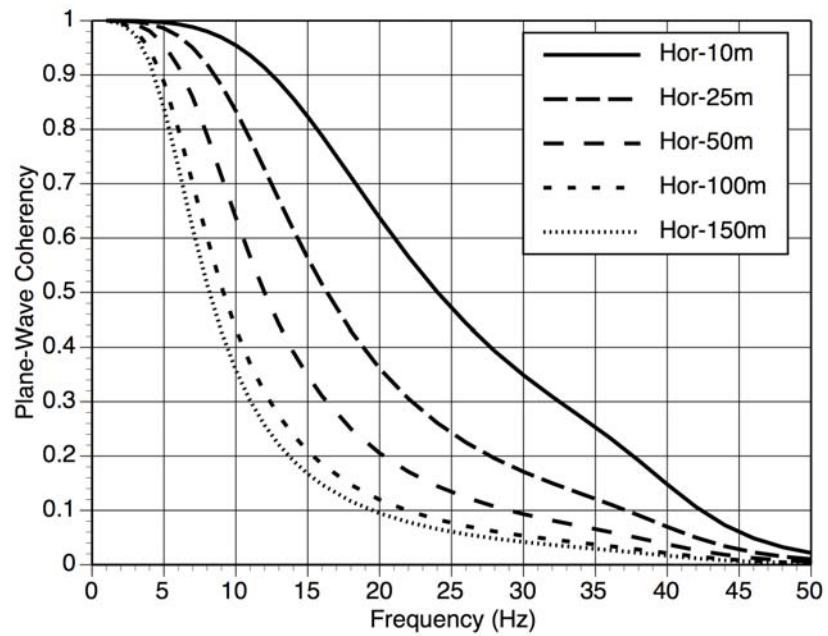| Coeff	Vertical Coeff
a_1	1.0
a_2	200
a_3	0.4
$n_1(\xi)$	$2.03+0.41*\ln(\xi+1)-0.078[\ln((\xi+1)-3.6]^2$
n_2	10
$f_c(\xi)$	$29.2-5.20*\ln(\xi+1)+1.45[\ln((\xi+1)-3.6]^2$

Figure 6-1
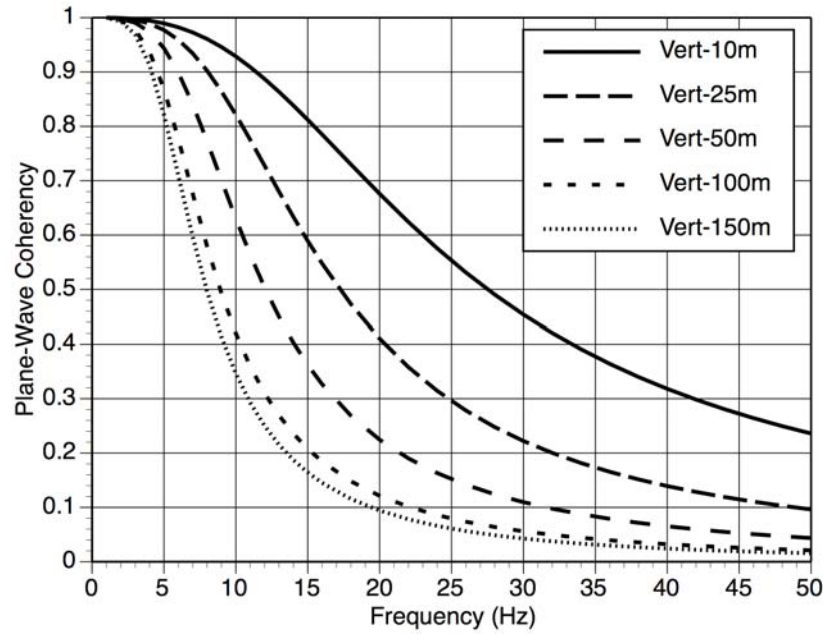**Plane-Wave Coherency for the Horizontal Component**

Figure 6-2
Plane-Wave Coherency for the Vertical Component

Residuals

The residuals for the horizontal and vertical coherencies are shown in Figures 6-3, 6-4, 6-5 and 6-6. In these figures, each point is the residual of the mean coherency for the distance bin for one earthquake and one frequency. The mean residual over the frequency band of 10-35 Hz is shown in Figure 6-7. The model has near zero mean residual over the frequency band of 10-35 Hz.
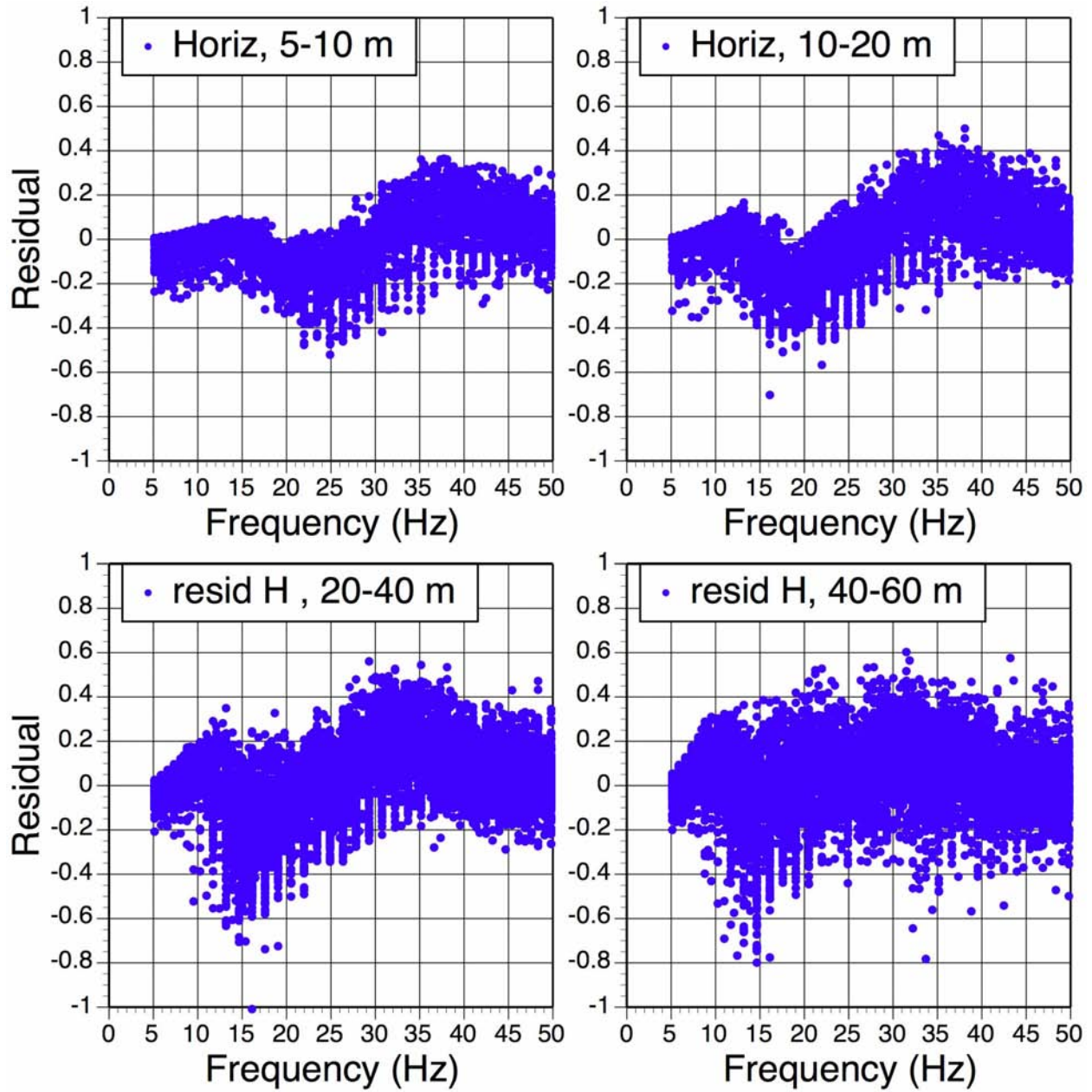
Figure 6-3
Plane-Wave Coherency Residuals for the Horizontal Component (Separation Distances of 5-60m)
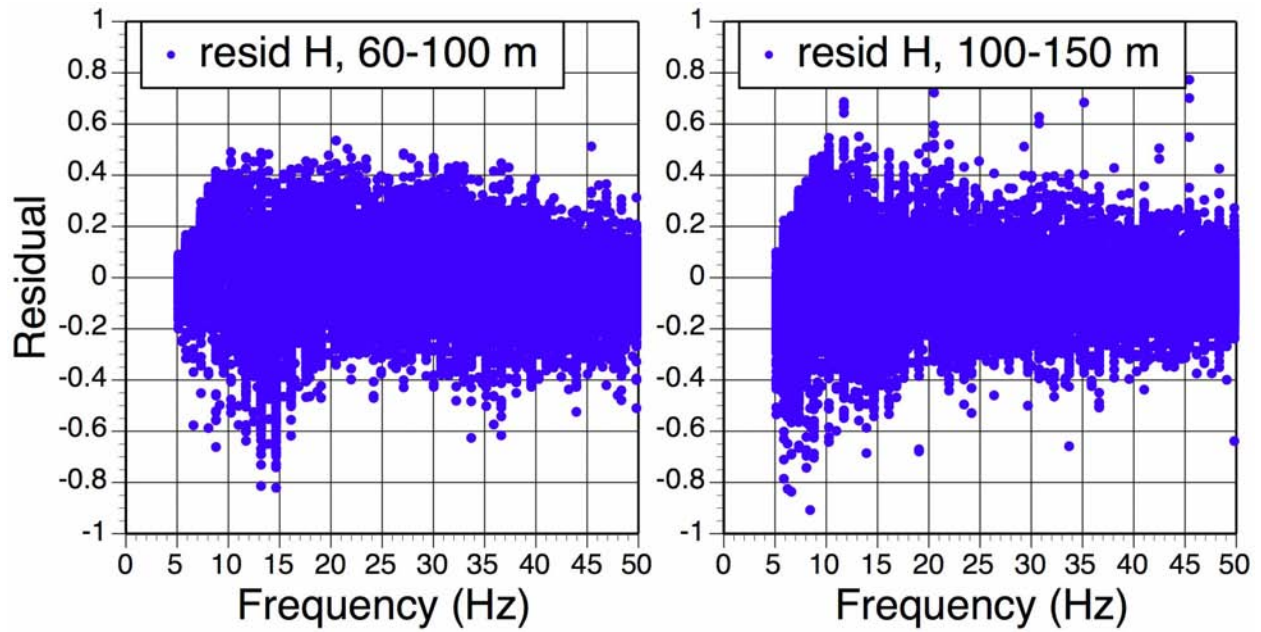
Figure 6-4
Plane-Wave Coherency Residuals for the Horizontal Component (Separation Distances of 60-150m)
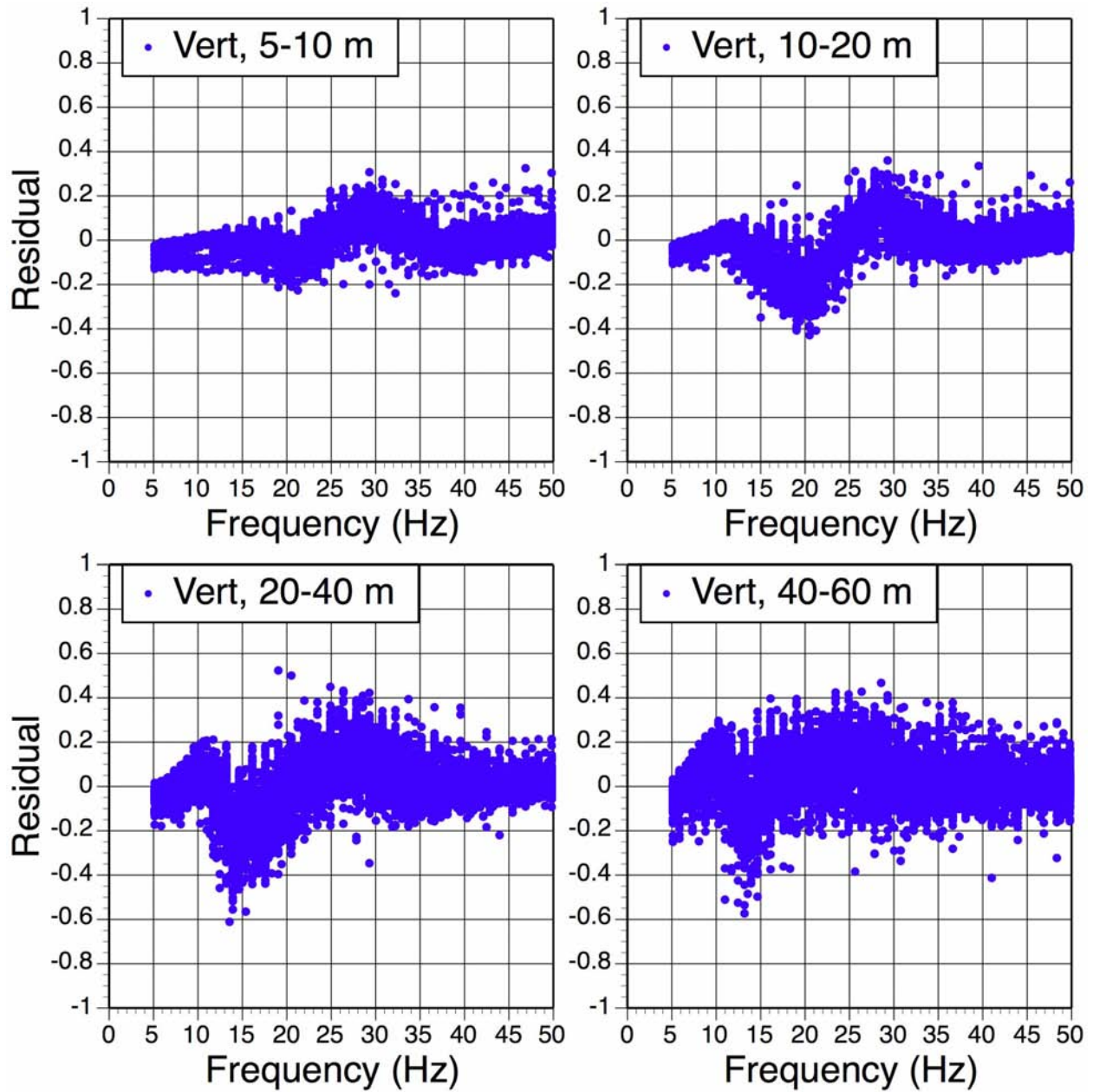
Figure 6-5
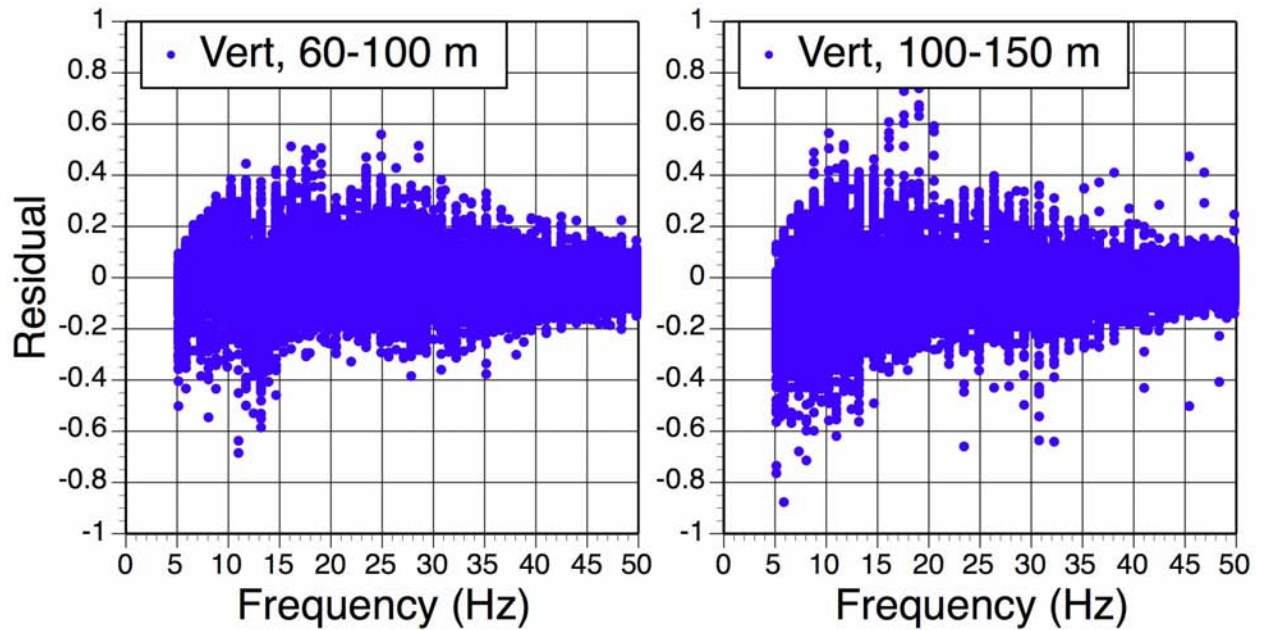**Plane-Wave Coherency Residuals for the Vertical Component (Separation Distances of 5-60m)**

Figure 6-6
Plane-Wave Coherency Residuals for the Vertical Component (Separation Distances of 60-150m)
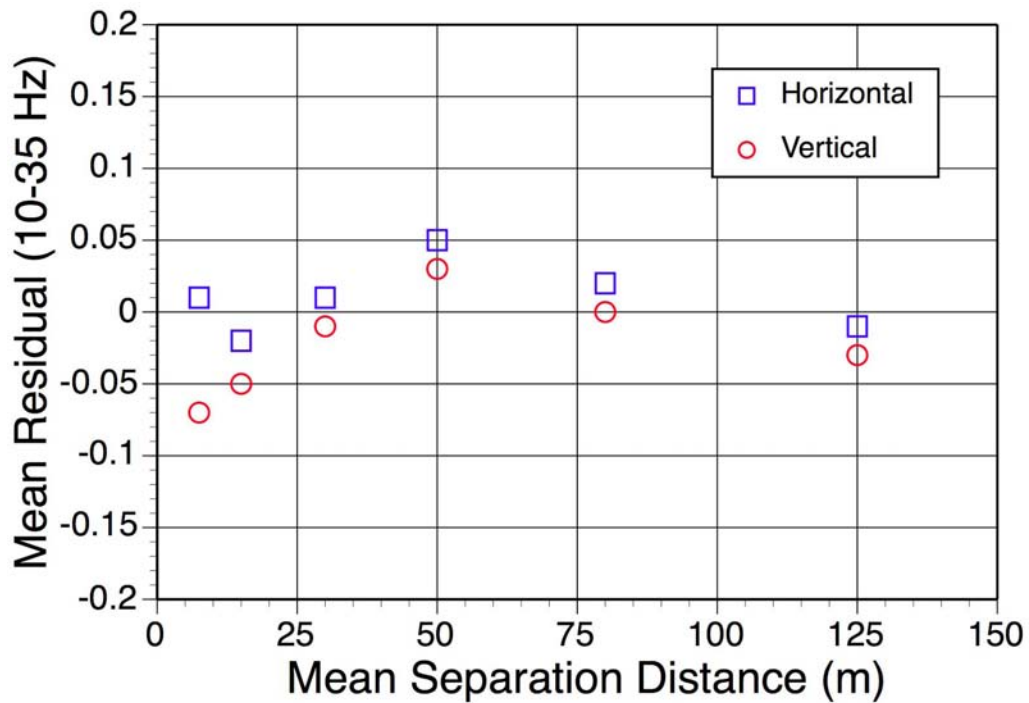

Figure 6-7
Mean Residuals Over 10-35 Hz

7
SOIL COHERENCY MODEL

Based on the site dependence seen in Chapter 5, a soil site coherency model is developed
using data from the four soil arrays: LSST, Chiba, IV, and Hollister.

Regression Analysis

The plane-wave coherency is modeled by the functional form described in Chapter 4:

$$\gamma_{pw}(f,\xi) = \left[1 + \left(\frac{f \ Tanh(a_3\xi)}{a_1 f_c(\xi)}\right)^{n1(\xi)}\right]^{-\frac{1}{2}} \left[1 + \left(\frac{f \ Tanh(a_3\xi)}{a_2}\right)^{n2}\right]^{-\frac{1}{2}}$$

Equation 7-1

The regression analysis was conducted using the $tanh^{-1}(\gamma_{pw})$ because this transformation leads to
residuals that are approximately normally distributed. As a first step, the data are grouped into
five separation distance ranges: 0-15m, 15-30m, 30-60m, 60-100m, and 100-150 m. For each
distance range, the f_c, a_2, n_1 and n_2 values are estimated independently using ordinary least-
squares. The average value for the a_2 and n_2 are found and the f_c and n_1 terms are re-computed.
Finally, the separation distance dependence of the f_c and n_1 terms is modeled using ordinary
least squares.

The coefficients were derived from using data from the earthquakes listed in Tables 3-3, 3-5, 3-6
and 3-7 for the four soil arrays. The soil data are limited in terms of the high frequency content
due to damping in the soil. Therefore, the maximum frequency used in the regression analysis
is 20 Hz. The data were grouped into 6 distance bins (0-10m, 10-20m, 20-30m, 30-50m, 50-70m,
and 70-100m) and 2 hz frequency bands. The mean $tanh^{-1}(\gamma_{pw})$ for each distance-frequency bin
is used in the regression.

The resulting model coefficients are given in Tables 7-1 and 7-2 for the horizontal and vertical
components, respectively. The plane-wave coherency models for the horizontal and vertical
components are shown in Figures 7-1 and 7-2, respectively. The results of the model are
presented in terms of the untransformed coherency because it is easier to understand.

The soil site coherency model leads to lower coherency values than the hard-rock coherency
model shown in Chapter 6, particularly for the vertical component at larger separation distances.

Table 7-1
Plane-Wave Coherency Model Coefficients for the Horizontal Component

Coeff	Horiz Coeff
a_1	1.0
a_2	$15.8 - 0.044\xi$
a_3	0.4
$n_1(\xi)$	3
n_2	15
$f_c(\xi)$	$14.3 - 2.35 * \ln(\xi+1)$

Table 7-2
Plane-Wave Coherency Model Coefficients for the Vertical Component

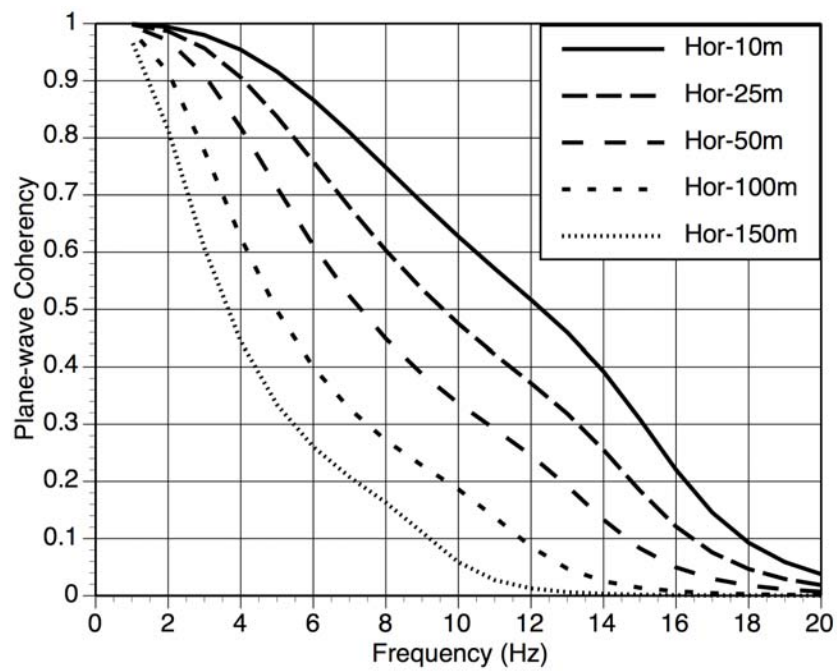| Coeff	Vertical Coeff
a_1	1.0
a_2	100
a_3	0.4
$n_1(\xi)$	1.3
n_2	3
$f_c(\xi)$	$\exp(2.25 - 0.021\xi)$

Figure 7-1
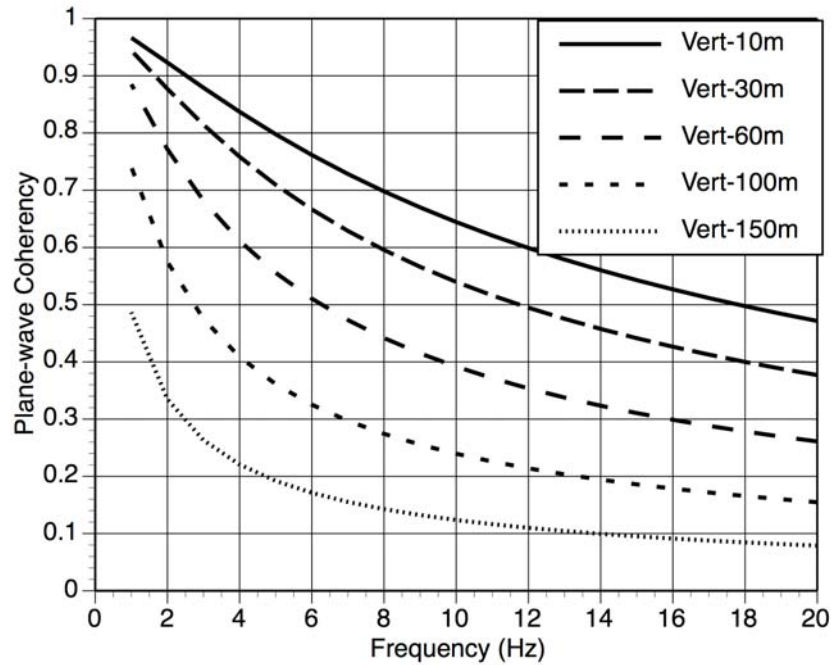**Plane-Wave Coherency for the Horizontal Component for Soil Sites**

Figure 7-2
Plane-Wave Coherency for the Vertical Component for Soil Sites

Residuals

The residuals for the horizontal and vertical coherencies (in coherency units, not $\tanh^{-1}(\gamma_{pw})$ are shown in Figures 7-3 and 7-4. The residuals are also shown in terms of the untransformed coherency since this emphasizes the key aspects of the model; the transformed coherency puts more emphasis on the differences in the very high coherency values (e.g. between 0.95 and 0.99).In these figures, each point is the residual is from the mean coherency for the distance-frequency bin. The residuals show that the soil coherency models do not have a significant relationship with either separation distance or frequency.
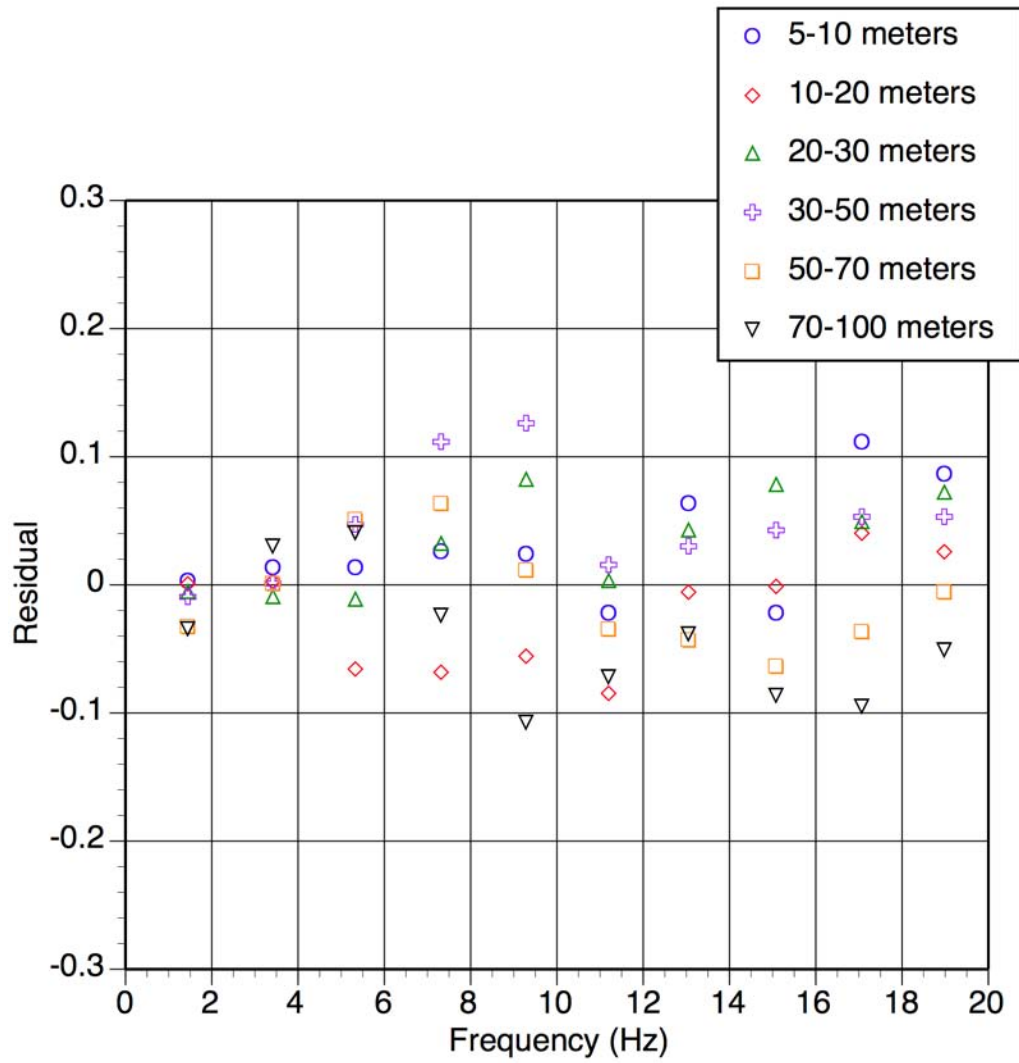
Figure 7-3
Plane-Wave Coherency Residuals (in Arithmetic Units) for the Horizontal Component for Soil Sites
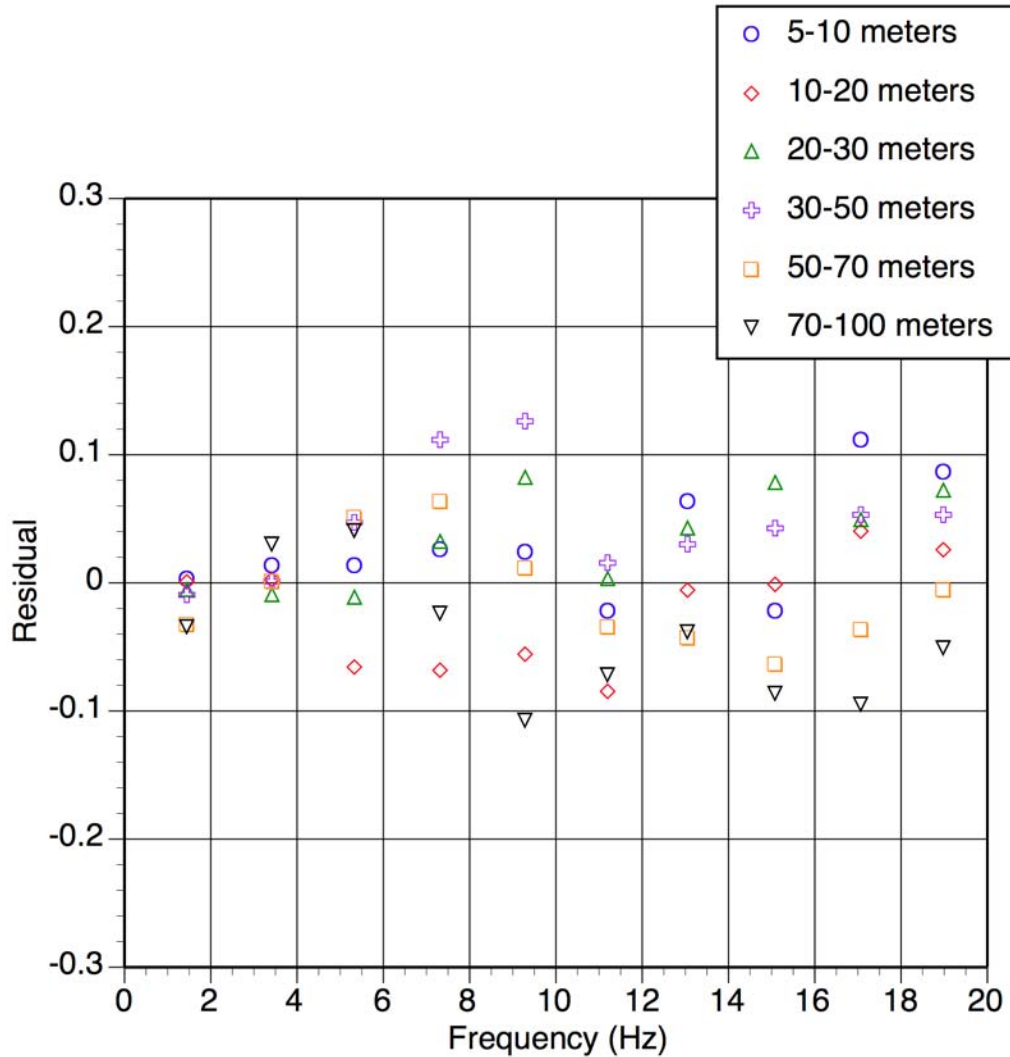
Figure 7-4
Plane-Wave Coherency Residuals for the Vertical Component for Soil Sites

Applicability of the Soil Coherency Model

The average shear-wave velocity in the top 30 m (V_{S30}) for the four soil arrays is listed in Table 7-3. The soil coherency model is applicable to soil sites with V_{S30} values in the range of 180-290 m/s. It is applicable to all magnitudes and source distances and to separation distances in the range of 0 to 150 m.

Table 7-3
Average Shear-Wave Velocity in Top 30 m

Array	V_{S30}
EPRI/LSST	210 m/s
Chiba	290 m/s
IV Differential	180 m/s
Hollister Differential	215 m/s

Coherency for Soft-Rock Sites

There is very little dense array data for soft-rock conditions. The Coalinga and the EPRI Parkfield arrays are on soft-rock sites. Of these two arrays, the EPRI Parkfield array has much better sampling at short separations (less than 100 m) than the Coalinga array. As discussed in Chapter 5 (Figure 5-9), for distance separation of 15-30 m, the coherency for the soft-rock (EPRI Parkfield) falls between the hard-rock and soil coherency. For larger separation distances (50-70m), the coherency for soft-rock is similar to the soil coherency. This lower soft-rock coherency for separation distances of 50-70m is due to the lower coherency from the Coalinga array. The coherency from the EPRI Parkfield array stays between the soil and hard-rock coherency. For SSI applications on soft-rock, it is recommended that the average of the soil and hard-rock coherency be used. This recommendation leads to some conservatism in the coherency (in terms of the reduction of the high frequency response of structures on large foundations) as compared to the average soft-rock coherency using both the Coalinga and EPRI Parkfield arrays.

Coherency for Embedded Sites

There are few data from embedded dense arrays. Based on the comparisons shown in Figure 5-1, the coherency for arrays embedded in soil or in soft-rock is similar to the hard-rock coherency. For SSI applications with embedded foundations of 10 m or more, it is recommended that the hard-rock coherency function be used.

8
CONCLUSIONS

The coherency model developed in this study based on the Pinyon Flat data set is considered to be applicable to hard-rock conditions. The model is applicable to all magnitudes and distances and for separation distances of 0 to 150 m. The hard-rock coherency model can be used as a conservative model for the coherency for soft-rock and soil sites and for embedded foundations; however lower coherency can be justified for soil and soft-rock site conditions.

The soil site coherency model developed in this study is considered to be applicable to soil sites with V_{S30} values of 180 to 290 m/s. The model is applicable to all magnitudes and distance and to separation distances of 0 to 150 m.

For SSI applications on soft-rock, it is recommended that the average of the soil and hard-rock coherency be used. For SSI applications with embedded foundations of 10 m or more, it is recommended that the hard-rock coherency function be used.

9
REFERENCES

Abrahamson, N. A., J. F. Schneider, and J. C. Stepp (1991). Empirical spatial coherency functions for application to soil-structure interaction, *Earthquake Spectra*, **7**, 1-28.

Abrahamson, N. A. (1992). *Spatial variation of earthquake ground motion for application to soil-structure interaction.* EPRI Report 2978-1.

Anderson, D. G. and H. T. Tang (1987). *Summary of soil characterization program for the Lotung Large-scale seismic experiment, Proc: Workshop on Lotung Large-Scale Seismic Experiment.* EPRI, Palo Alto, CA: December 1987.

Bonamassa, O., J. E. Vidale, H. Houston, and S. Y. Schwartz (1991). Directional site resonances and the influence of near-surface geology on ground motions, *Geophysical Research Letters*, **18**, 901-904.

Chang, C.Y., M. S. Power, Y. K. Tang, and C. M. Mok (1988). Evidence of nonlinear soil response during a moderate earthquake, Twelfth Inter. Conf. Soil. Mech. and Foundation Eng., August 13-18, 1989, Rio de Janeiro, Brazil.

Geological and geophysical characterization of the site of the Parkfield dense seismic array, RP2556-40. Electric Power Research Institute (1988).

Enochson, L. D. and N. R. Goodman (1965). Gaussian approximations to the distributions of sample coherence, Tech Report, AFFDL-TR-65-57, Wright- Patterson Air Force Base.

Fletcher, J. B., L. M. Baker, P. Spudich, and P. Goldstein. (1991?). The USGS Parkfield, California, dense seismographic array-UPSAR, *Bull. Seism. Soc. Am.*

Hanson, R. (1992). Personal Communication.

Katayama, T., F. Yamazaki, F., S. Nagata, L. Lu, and T. Turker (1990). Development of strong motion database of the Chiba seismometer array, Earthquake Disaster Mitigation Engineering, Institute of Industrial Science, University of Tokyo, Report No. 90-1 (14).

Mueller, C. S, E. Sembera, and L. Wennerberg (1994). Digital recordings of aftershocks of the May 2, 1983 Coalinga, California Earthquake, U.S. Geol. Surv. OFR 84-697.

Mueller, C. and G. Glasmoyer (1990). Digital recordings of aftershocks of the 17 October 1989 Loma Prieta, California, Earthquake, U.S. Geol. Surv. OFR 90-503.

References

Owens, T. J., P. N. Anderson, and D. E. McNamara (1991). The 1990 Pinyon Flat high frequency array experiment, An IRIS Eurasian seismic studies program passive source experiment, PASSCAL Data Report #91-002.

Pavlis, G. (1992). Personal Communication.

Salsman, M. and R. Forshee (1988). Strong motion data from the Hollister earthquake of February 20, 1988, U.S. Geol. Surv., OFR 88-565.

Schneider, J.F., N.A. Abrahamson, P.G. Somerville, and J.C. Stepp (1990). Spatial variation of ground motion from EPRI's dense accelerograph array at Parkfield, California, Proc. Fourth U.S. Nat. Conf. on Earthquake Eng., EERI, Palm Springs, 375-384.

Smith, S. W., J. E. Ehrenberg, and E. N. Hernandez (1982). Analysis of the El Centro Differential Array for the 1979 Imperial Valley Earthquake, *Bull. Seism. Soc. Am.*, **72**, 237-258.

Somerville, P.G., J.P. McLaren, and C.K. Saikia (1988). Site-specific estimation of incoherence of strong ground motion, Proc. Earth. Engin. Soil Dyn., Recent Advances in Ground Motion Evaluation, ASCE, Park City, Utah, 188-202.

Export Control Restrictions

Access to and use of EPRI Intellectual Property is granted with the specific understanding and requirement that responsibility for ensuring full compliance with all applicable U.S. and foreign export laws and regulations is being undertaken by you and your company. This includes an obligation to ensure that any individual receiving access hereunder who is not a U.S. citizen or permanent U.S. resident is permitted access under applicable U.S. and foreign export laws and regulations. In the event you are uncertain whether you or your company may lawfully obtain access to this EPRI Intellectual Property, you acknowledge that it is your obligation to consult with your company's legal counsel to determine whether this access is lawful. Although EPRI may make available on a case-by-case basis an informal assessment of the applicable U.S. export classification for specific EPRI Intellectual Property, you and your company acknowledge that this assessment is solely for informational purposes and not for reliance purposes. You and your company acknowledge that it is still the obligation of you and your company to make your own assessment of the applicable U.S. export classification and ensure compliance accordingly. You and your company understand and acknowledge your obligations to make a prompt report to EPRI and the appropriate authorities regarding any access to or use of EPRI Intellectual Property hereunder that may be in violation of applicable U.S. or foreign export laws or regulations.

The Electric Power Research Institute (EPRI), with major locations in Palo Alto, California; Charlotte, North Carolina; and Knoxville, Tennessee, was established in 1973 as an independent, nonprofit center for public interest energy and environmental research. EPRI brings together members, participants, the Institute's scientists and engineers, and other leading experts to work collaboratively on solutions to the challenges of electric power. These solutions span nearly every area of electricity generation, delivery, and use, including health, safety, and environment. EPRI's members represent over 90% of the electricity generated in the United States. International participation represents nearly 15% of EPRI's total research, development, and demonstration program.

Together...Shaping the Future of Electricity

Program:

Technology Innovation

1015110